THE IMPACTS OF CLIMATE VARIABILITY AND CHANGE ON THE PHYSICAL AND SOCIAL-ECOLOGICAL DYNAMICS OF THE KUROSHIO AND NORTH PACIFIC TRANSITION ZONE

A Dissertation
Presented to
The Academic Faculty

By

Gian Giacomo Navarra

In Partial Fulfillment of the
Requirements for the Degree
Doctor of Philosophy in the
School of Science
Department of Earth and Atmospheric Science

Georgia Institute of Technology

Dec 2022

THE IMPACTS OF CLIMATE VARIABILITY AND CHANGE ON THE PHYSICAL AND SOCIAL-ECOLOGICAL DYNAMICS OF THE KUROSHIO AND NORTH PACIFIC TRANSITION ZONE

Thesis committee:

Dr. Emanuele Di Lorenzo
School of Earth and Atmospheric Science
Georgia Institute of Technology

Dr. Yi Deng
School of Earth and Atmospheric Science
Georgia Institute of Technology

Dr. Takamitsu Ito
School of Earth and Atmospheric Science
Georgia Institute of Technology

Dr. Iris Tien
School of Civil and Environmental Engineering
Georgia Institute of Technology

Dr. Joseph Montoya
School of biology
Georgia Institute of Technology

Dr. Ryan Rickazewski
Pacific Islands Fisheries Science Center, Ecosystem Sciences Division, Honolulu, HI, United States
NOAA

Date approved: December, 2022

The person who live only for himself live just one time

Gian Giacomo Navarra

ACKNOWLEDGMENTS

My deepest gratitude goes to Prof.Emanuele Di Lorenzo, my advisor, he proved to be a very good advisor. I am glad to him not only for making me the scientist that I am now but also because he has supported me in every situation. In my second year, I had an important brain surgery operation so not to have epileptic seizures anymore. My advisor has been extremely nice during that difficult period. Thanks also to all my defense committee for their support. I want to thank Prof. Takamitsu Ito who always impress me for his knowledge and for being a great friend. Also, I want to thank Prof. Yi Deng, Prof. Iris Tien, Prof. Joseph Montoya and Dr. Ryan Rickazewski for helping me in my graduate studies. I am also very gratefull to Prof.Roozbahani, Dr.Maike Sonnewald and Antonietta Capotondi who helped to shed new light on many of my ideas. Also, I want to extend my gratitude to my lab group peers and the EAS department in general.Thank you to Annalisa Bracco and Kim Cobb. The former for helping in building all my ocean dynamics knowledge and the latter for her useful advice in my academic carrer. Special thanks are due to the friends and colleagues who made this work possible, Giovanni Liguori, Fabrizio Falasca, Yingying Zhao, Youngji Joh, Filippos Taglikis, Tongtong Xu, Annika Jarid, and all the Ocean Science and Engineering (OSE) members. I am also very grateful to my parents, Nadia and Antonio, for their support despite the struggles of having me thousands of miles away.

TABLE OF CONTENTS

Acknowledgments iv

List of Tables viii

List of Figures ix

Summary xiv

Chapter 1: Introduction and Background 1

1.1 Kuroshio-Oyashio region 1

1.2 North Pacific Modes of Variability 1

1.2.1 Pacific Decadal Oscillation 2

1.2.2 North Pacific Gyre Oscillation 3

1.2.3 Regime shift of ecosystem 3

1.3 Forecasting marine ecosystems 4

1.3.1 Dynamical Forecasting approach 4

1.3.2 Statistical Forecasting approach 5

1.4 Motivation 5

1.5 References 7

Chapter 2: Understanding past and projected changes in climate 11

2.1 Introduction 11

2.2 Methodology 14

2.2.1 Variance trend calculation 15

2.2.2 Model output 15

2.2.3 Test to evaluate the significance of trends in variance in an ensemble 16

2.3 Characterizing the North Pacific Transition Zone (NPTZ) 17

2.4 Climate Change Projections of NPTZ, CESM-LE vs. CMIP5-E 19

2.4.1 Changes in mean circulation of the North Pacific Ocean 19

2.4.2 Changes in the Variability of the NPTZ 21

2.5 Correlation SLP forcing index with SSH_{PC1} and SSH_{PC2} 23

2.6 Conclusions 24

2.7 References 27

Chapter 3: Predictability and Empirical Dynamics of Fisheries Time Series in the North Pacific 43

3.1 Introduction 43

3.2 Methodology 46

3.2.1 Reanalysis Data 46

3.2.2 Fishery Data 47

3.2.3 Detrending and Standardization 48

3.2.4 Principal Components and Empirical Orthogonal Functions 48

3.2.5 LIM model 49

3.2.6 Cross-validation 52

3.2.7 LIM tau test 53

3.2.8 Persistence and Forecast Skill 53

3.3 Results and Discussion 54

3.3.1 Fisheries biomass data and relation to physical quantities 54

3.3.2 LIM Forecasts of the low-frequency variability of the KOE 56

3.3.3 LIM forecast of Fisheries Time Series 57

3.3.4 LIM forecasting skills Sensitivity analysis 59

3.4 Conclusions 60

3.5 References 62

Chapter 4: Conclusion and Future Research 80

4.1 References 83

Appendices 86

Appendix A: Appendix Chapter 2 87

Appendix B: Appendix Chapter 3 96

LIST OF TABLES

2.1 CMIP5 models 16

B.1 RAM stocks 97

B.2 LME stocks 101

B.3 LME stocks 102

B.4 LME stocks 103

B.5 FAO stocks 104

B.6 FAO stocks 105

LIST OF FIGURES

1.1 Root Mean Square SSH 2

1.2 SEES system 6

2.1 Satellite Data of SSH and Chl-a. In (a) the mean chlorophyll concentration is shown with particular relevance to the NPTZ area. (b) represents the total correlation between SSH and chlorophyll. In c) and d) instead correlation maps between SSH anomalies with the first pc and second pc are explained. The former case, is displayed in c) while the correlation with the second pc is in d). Then the last two represent how the first pc correlates with PDO index (e) and how the second pc correlates with the NPGO index (f). 34

2.2 CESM-LE and CMIP5-E difference maps for SSH. In (a) the mean SSH in the period 1950-2000 is explained, the black lines represents the contour of the mean SSH in this period. In (b) the difference between 1950-2000 and 2050-2100 SSH is calculated. In (c) and d) the same is done but for the variance of the SSH. In (e)-(h) figures the same procedures has been followed but with CMIP5-E models. Units of SSH are in cm 35

2.3 CESM-LE and CMIP5-E difference maps for SLP. In (a) the mean SSH in the period 1950-2000 is explained and the black lines represent the contour of the mean SLP in this period. In (b) the difference between 1950-2000 and 2050-2100 SSH is calculated. In (c) and (d) the same is done but for the variance of the SSH. In (e)-(h) figures the same procedures have been followed but with CMIP5-E models. Units of SLP are in cm 36

2.4 EOF of SSH and SLP with trend. In (a) the first EOFs with trend is displayed. There is a clear pattern in the region of the Kuroshio. In (b) the first pc associated with this EOF is represented. This gives a clear increasing trend. Then the same EOF Is calculated for the SLP in (c).In this case, the first pc explains a stable scenario. In (e)-(h) the same figures have been done but with the CMIP5 models. Units of SSH are in cm, while SLP Units are in Pa. 37

2.5 EOF analysis CESM detrended anomalies. In a) and b) the first and second EOF for the SSH anomalies are represented. Here the trend has been removed, compared to Fig.2.4. The trend in the variance corresponding to the first EOF is displayed in (b). In this latter one the top figure displayed the principal component and the mean pc(in black). In the bottom figure instead the trend of the variance is represented. In (g) and (h) the pdf associated to the random samples (grey part in (e) and (f)) is calculated. In this case, the CESM output is taken into consideration . Units of SSH are in cm. 38

2.6 EOF analysis CMIP5 detrended anomalies. In (a) and (b) the first and second EOF for the SSH anomalies are represented. Here the trend has been removed, compared to Fig.2.4. The trend in the variance corresponding to the first EOF is displayed in (b). In this latter one, the top figure displayed the principal component and the mean pc(in black). In the bottom figure instead the trend of the variance is represented. In (g) and (h) the pdf associated to the random samples (grey part in (e) and (f)) is calculated. In this case the CMIP5 output is taken into consideration . Units of SSH are in cm. 39

2.7 In (a) the first correlation pattern for the SLP anomalies over the first pc of SSH is represented. The trend in the variance corresponding to the first pattern is displayed in (c). The principal components for each single runs are the grey part while the mean pc is in black. The trend of the variance is given by the green line. In (e) the percentage increase is calculated. The red line is the increase for just the summer season, while the blue line regards the winter season. In (b) the second correlation pattern associated to the SLP anomalies projected over the second pc of SSH is displayed. The trend in the variance corresponding to the first pattern is described in (d) while the associated percentage increase is in (f). The grey part in (e) and (f) describe the significance test performed. In this case CESM runs are taken into consideration. Units of SSH are in cm. 40

2.8 In (a) the first correlation pattern for the SLP anomalies over the first pc of SSH is represented. The trend in the variance corresponding to the first pattern is displayed in (c). The principal components for each single runs are the grey part while the mean pc is in black. The trend of the variance is given by the green line. In (e) the percentage increase is calculated. The red line is the increase for just the summer season, while the blue line regards the winter season. In (b) the second correlation pattern associated to the SLP anoamlies projected over the second pc of SSH is displayed. The trend in the variance corresponding to the first pattern is described in (d) while the associated percentage increase is in (f). The grey part in (e) and (f) describe the significance test performed. In this case CMIP5 models are taken into consideration. Units of SSH are in cm. 41

2.9 in this case we consider the response of the climate system to continous random forcing and its correlation with the first and second pc of SSH. In (a) and (b) the correlation between the SLP forcing index and the SSH ensemble mean first and second pc is displayed. In this case the CESM-LE output has been used. In (c) and (d) the same figures have been done with the CMIP-E models. We obtain a correlation a little higher in the CESM-LE case 42

3.1 Timeseries of detrended and normalized fish stocks for the RAM (a), LME (b), and FAO (c) datasets. The variance explained by the removed trend is represented in (d), (e),and (f). The mean variance excluded by the detrending has been inserted in the plots. The associated variability is described by the first and second principal component (g) and (h), while the corresponding EOFs are displayed in supplementary Figure S1. The percentage of variance explained by the PCs in each dataset is shown in (i). 73

3.2 Correlation map between SST anomalies and PC1 (a) and PC2 (c) of the fishery datasets (RAM, LME, FAO). The average correlation maps across the datasets for PC1 and PC2 are shown in (b) and (d). 74

3.3 Forecast correlation skill of the LIM with physics only (SSTa, SSHa) for lead-times of 6 months (a), 12 months (b), and 24 months (c). In (d), (e), and (f) the same correlation skill maps are shown but computed using the 6-year low-pass filter applied on the original and forecasted monthly data . 75

3.4 KOE SSTa index forecast correlation skill as a function of the initialization month of the year from the physics only LIM (a), the persistence (b), and their difference (c). The same correlation skill maps are shown but computed after applying a 6-year low-pass filter applied on the original and forecasted monthly data (d)(e), and (f). 76

3.5 The LIM forecasting correlation skill as a function of different lead-times is displayed from the RAM (a), LME (b), and FAO (c) stocks. The persistence correlation skill for each of these stock is also shown for comparison in (d), (e), and (f). A different between the skill of the LIM minus persistence is shown in (g), (h), and (i). 77

3.6 Selected single stock time series (blue lines) and the forecasted time series (red lines). The stock have been selected considering those that have the highest difference between forecasting LIM skill and the persistence. The 2- year lead forecast are shown for the RAM (a,b), for LME (e,f) and for the FAO(i,j). The same comparison are shown for the 5-year lead forecast in panels (c,d) for RAM, (g,h) for LME, and (k,l) for FAO. The name of the selected stock is displayed at the top of each panel 78

3.7 Same as Figure 5, except showing the forecast skill of the LIM where the physics and fish sticks are decoupled, (a) RAM, (b) LME, (c) FAO. The differences in skill between the decoupled and the full LIM case are shown in (d), (e), and (f). The forecasting correlation skill as a function of different lead-times is displayed also for a LIM where each stock is forecasted independently are shown for the RAM (g), LME (h), and FAO (i) datasets, along with the differences from full LIM case in panels (d), (e), and (f), respectively. 79

A.1 Figures 1-29 represents correlation map obtained by the projection of the SLP anomalies on the first pc of SSH calculated with CESM-LE output runs. In this case each single output has been considered. 88

A.2 Variance trend of the SLP using the CESM-LE output. In Figures a1-a29 the principal component and the mean pc(in black) are displayed. The trend is associated to the patterns obtained from the projection of PSL anomalies on the first pc of SSH. While in figures b1-b29 the trend in SLP variability for each singular model is considered. 89

A.3 In Fig.1-29 we consider the correlation map obtained by the projection of the SLP anomalies on the second pc of SSH calculated for each single CESM-LE output runs. 90

A.4 variance trend of the SLP. In Figures a1-a29 the principal component and the mean pc(in black) are displayed. The trend is associated to the patterns obtained from the projection of SLP anomalies on the second pc of SSH. While in figures b1-b29 the trend in SLP variability for each singular model is represented. The CESM has been used 91

A.5 In Fig.1-23 we represent correlation map obtained by the projection of the SLP anomalies on the first pc of SSH. In this case the CMIP5-E models have been used. 92

A.6 Variance trend of the PSL using the CMIP5-E models. In Figures a1-a29 the principal component and the mean pc(in black) are displayed. The trend is associated to the patterns obtained from the projection of PSL anomalies on the first pc of SSH. While in figures b1-b29 the trend in SLP variability for each singular model is considered. 93

A.7 In Fig.1-23 we represent correlation maps obtained by the projection of the SLP anomalies on the second pc of SSH. In this case the CMIP5-E have been used. 94

A.8 variance trend of the PSL using the CMIP5-E models. In Figures a1-a29 the principal component and the mean pc(in black) are displayed. The trend is associated to the patterns obtained from the projection of PSL anomalies on the second pc of SSH. While in figures b1-b29 the trend in SLP variability for each singular model is considered. 95

B.1 The first and second EOF weights for the RAM Biomass (a), the LME landings (b), and FAO catches (c). 96

B.2 Eigenvalue spectra of the LIM operator L (a) and the spectra of the matrix Q (b) for the LIM containing only SST and SSH. The same calculation has been done in (c) and(d) for the RAM LIM, in (e) and (f) for the LME LIM and in (g) and (h) the FAO LIM. 98

B.3 LIM tau test applied to the SST forecast LIM. In column (a)-(c) we compute the lag Covariance matrix with the LIM up to 2 years of leading time. The results are compared with the lag covariance matrix from the observational data (d)-(f). 99

B.4 LIM tau test for the RAM stocks. The test consists in calculating the covariance matrix with the state vector (d)(e)(f) and compare the results with the same matrix obtained from the LIM (a)(b)(c). The calculation is done at different lags up to 132 months. 100

B.5 LIM tau test for the FAO stocks. The test consists in calculating the covariance matrix with the state vector (d)(e)(f) and compare the results with the same matrix obtained from the LIM (a)(b)(c). The calculation is done at different lags up to 132 months. 106

B.6 LIM tau test for the LME stocks. The test consists in calculating the covariance matrix with the state vector (d)(e)(f) and compare the results with the same matrix obtained from the LIM (a)(b)(c). The calculation is done at different lags up to 132 months. 107

B.7 The LIM forecasting correlation skill as a function of different lead-times is displayed from the RAM (a), LME (b), and FAO (c) stocks. Prior to the computation of the skill, a 6-year high-pass filter applied. The difference in skill between the full LIM and the high-pass version is displayed in (d), (e), and (f) for the three datasets respectively 108

SUMMARY

There is growing recognition that climate change is impacting the ocean's western boundary current system. In the Pacific, the Kuroshio and its offshore Kuroshio-Oyashio Extension (KOE) play a central role in the North Pacific climate and impact the social-ecological dynamics of countries that rely on marine ecosystem services (e.g. fisheries). In the thesis, we have used a combination of observations and modeling approaches to understand how past and projected changes in the physical environment of KOE impact social-ecological dynamics linked to the fish industry of Japan and the North Pacific more widely. The thesis is articulated in 3 Chapters. In Chapter 1 we have introduced the problem and the main motivation that lead us to perform this study. In Chapter 2, we analyze the climate variability and change of the KOE over the historical and future projection period 1920-2100. We perform this task using Coupled Model Intercomparison Project 5 (CMIP5) models and a large ensemble from the Community Earth System Model (CESM-LE) output runs. The reason for considering also the CESM-LE runs is that they give the possibility to explore how the variance of the KOE in one model (e.g. a fixed set of dynamics) responds to anthropogenic forcing when compared to the range of natural variability of the CESM-LE model. In this way, we can perform a scenario which goes beyond the time of the observational data. In Chapter 3, we have used an Empirical Dynamical Model approach to characterize the joint statistics of the physical and social-ecological environmental system (SEES) that is relevant to climate and fisheries. To define the states of the SEES we use three international fish databases, (1) the Large Marine Ecosystem (LME, 9,000 fish stocks), (2) the NOAA fishery database referred to as Restricted Access Management (RAM, 300 fish stock) and the (3) the Food and Agriculture Organization (FAO, 1400 fish stocks). Among the approaches used to explore the relationship between KOE's climate and the SEES response, we have developed a Linear Inverse Model (LIM) approach that has been very successful to simulate and predict the KOE physical climate and its re-

lation to large-scale Pacific dynamics such as El Niño Southern Oscillation (ENSO), the Pacific Decadal Oscillation (PDO), and others.

CHAPTER 1
INTRODUCTION AND BACKGROUND

1.1 Kuroshio-Oyashio region

The Kuroshio-Oyashio region is formed by the Western Boundary Current(WBC) of the North Pacific subtropical and subpolar gyres. As represented in Fig. 1.1, the Kuroshio-Oyashio system has two recirculation gyres, an anticyclonic Southern Gyre and a cyclonic Northern Gyre. In the middle, around 35 N, quasi stationary meanders form the Kuroshio Oyashio Extension (KOE) jet. Atmosphere-ocean interactions are exceptionally strong [Kwon et al. 2010] over the WBC and their eastward extension. For example, the largest mean and variance at inter-annual and longer timescales of the net surface heat flux occurs in the WBC regions. In addition, eddy variability has also been found to play an important role in the surface ocean heat budget [Kelly 2010; Vivier et al.2002; Nonaka and Xie 2003]. The eddy kinetic energy level in the upstream region (32-38N and 141-153E) reveals that its variability correlates well regional KOE path variability [Qiu et al. 2005].

1.2 North Pacific Modes of Variability

The Kuroshio-Oyashio Extension jet is also known to be one of the major regions of decadal variability in the North Pacific. The origins of this low-frequency variability are linked to both internal and externally forced mechanisms. However, most studies[Ceballos et al. 2009] have identified external atmospheric forcing as a consequence of the adjustment of the PDO and NPGO SSH anomalies.

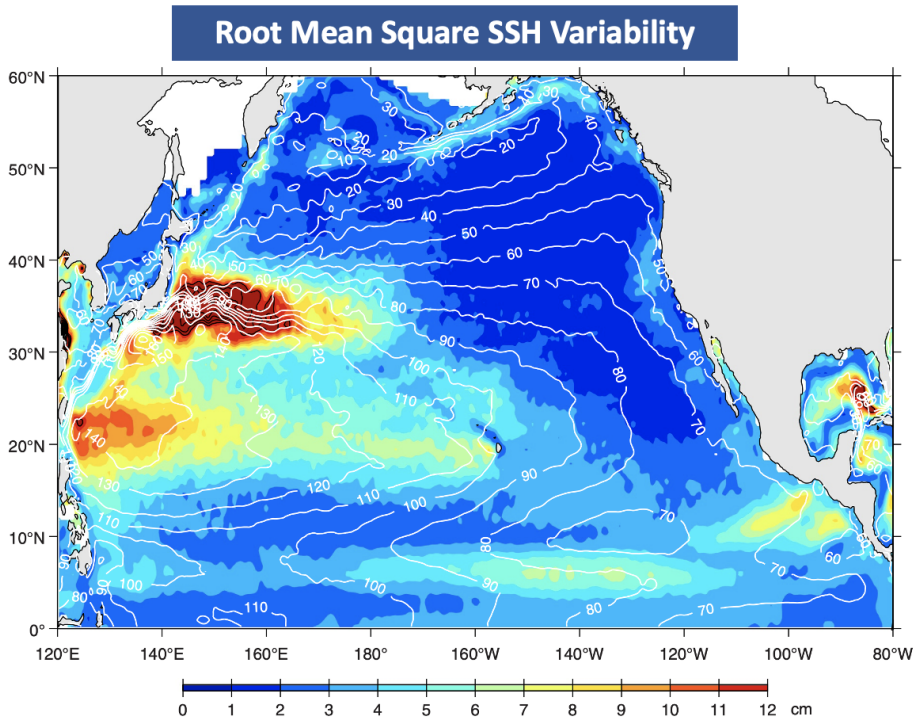

Figure 1.1: Qiu et al. 2013 ; Root mean Square SSH Variability in the North Pacific

1.2.1 Pacific Decadal Oscillation

The first mode considered is the Pacific Decadal Oscillation(PDO). The PDO was named by Steven Hare, who noticed it while studying salmon production patterns. It is the dominant low-frequency climate variability in the North Pacific and it is defined as the leading mode of detrended SST anomalies in the region [20, 60; -200, -110]. The PDO experiences phase shifts which occur every 30 years with pronounced effects on biology and fisheries. Specifically, when the PDO is in a positive phase, strong westerly winds and vertical mixing result in a cool SST and low spring primary production due to light limitation, with the reverse happening in a negative phase [(Mantua & Hare,2002; Miller et al., 2004]. The region of KOE responds to these oscillations with a time lag of 3-6 years because the anomalies have to propagate westward in the form of Rossby waves. Consequently, the KOE experiences a shift between two dynamical states, a stable and an unstable state. When in a stable phase the KOE eastward transport intensifies and the latitudinal position

shift more Northward [Qiu et al. 2014], while the opposite happens in an unstable phase.

1.2.2 North Pacific Gyre Oscillation

A second important mode is the North Pacific Gyre Oscillation or NPGO. As for the PDO, the NPGO is stochastically induced by the atmospheric mode of the North Pacific Oscillation (NPO) and it is defined as the second leading mode of the SST in the same region mentioned before. The ecological relevance of the NPGO has been recently emphasized by different studies [Di Lorenzo et al. 2008]. They find that NPGO variability is significantly correlated with fluctuations in salinity and Chl-a. On the East coast of the North Pacific, the NPGO reflects changes in wind stress, in particular winds that force coastal upwelling. This makes the NPGO a primary indicator for upwelling strength and nutrient fluxes (N03 and P04 and SiO2). In contrast to the phases of the PDO, the NPGO mode positive phase shows a pair of counter-rotating gyres that reflect the gyre scale mean circulation. In recent years the observed strengthening of the NPGO mode may represent a response to anthropogenic forcing and global warming[Bond et al., 2003;Douglass et al.,2006].

1.2.3 Regime shift of ecosystem

The impact of decadal fluctuations of the KOE on marine ecosystems is well documented. It has been found that the AL/PDO induces temporal variations in the KOE fisheries and secondary producers by dominating the seasonal mixed layer process [Chiba et al. 2009]. When the PDO is in the positive phase, that is a positive value of the associated index, the sea level dropped, the thermocline shoals and the mixed layer deepened leading to a weakening of the KOE. While the opposite happens in a negative phase. These climate regime shifts are well correlated with biological shifts [Yati Emi et al. 2020; Möllmann et al. 2012]. The weakening of the KOE leads to an increase in Western Pacific Sardines, while during a strengthening of the jet the anchovies are more abundant [Chavez et al. 2003]. Also, in recent years fisheries have been greatly impacted by climate change. One

important effect of the ocean heat uptake regards ocean deoxygenation which consists of the decline of Dissolved Oxygen with profound impacts on fisheries and marine ecosystems. This negative trend is driven by reduced ventilation and solubility [Ito et al. 2019; Keeling et al. 2010]. The lack of oxygen supply as the environment warms up may lead to altered distributions or extinctions of fish from cooler conditions. It is then very important to analyze and predict future scenarios for the marine ecosystem in the Kuroshio.

1.3 Forecasting marine ecosystems

However, even though our understanding of large-scale climate variability and its drivers has seen major advances, the mechanism by which climate variability impacts marine ecosystems and the services they provide remain not well understood. Furthermore, the ways in which human society interacts with these ecosystems can be very complex and determine the severity of the climate impacts [Bograd et al. 2019; Tam et al. 2019]. The influence of long-term anthropogenic climate change on the social-ecological and environmental dynamics of the North Pacific basin is increasingly evident. This impact is particularly strong in the Western Boundary Currents not only of the North Pacific but also of the Atlantic. To identify projected changes in fisheries due to climate change, social-ecological indicators have been used. Indicators acts as proxies to simplify complicated trends in biological, environmental and anthropogenic variables. [Shin and Shannon. 2010]. In the thesis, we have examined how past and projected changes in the physical environment of KOE impact social-ecological dynamics linked to the fish industry of Japan and the North Pacific more widely.

1.3.1 Dynamical Forecasting approach

Dynamical models have been extensively used for making the forecast of marine ecosystems [Yati et al. 2020]. Those models rely on the assumption that knowledge of the present climate yields useful predictions of future climate states[Tommasi et al.2017, Jacox et

al. 2020]. A great advantage of climate models is that they are able to simulate regions where no data are actually present (like the deep ocean). However, they are an imperfect representation of reality due to their finite resolution which force them to insert sub-grid parametrization for physical phenomena which happens below the resolution. One way to deal with this issue, in case observations are present, regards data assimilation. In this case, the observations or climate reanalysis produce an initialized climate state which differs from the one the model simulate by running freely.

1.3.2 Statistical Forecasting approach

On the other side, statistical approaches rely on extracting relations between the physical data on a large-scale circulation and the ecosystem data. These type of methods are much less memory intense compared to dynamical down-scaling and don't have a bias that are always present in climate models. There can be many types of statistical forecasting, however we can recognize two main types. the first one is uni-variate, so they relate the local variable to predict (the predictand) to just one large-scale climate variable (the predictor). The second main approach regards multivariate forecasting where the predictand is associated with many predictors. One issue related to the statistical approach is that they rely on long historical records for model training and development and are not well equipped to handle non-stationarity in physical-biological systems.

1.4 Motivation

Even though our understanding of large-scale climate variability and its drivers has seen major advances, the mechanism by which the climate variability impacts marine ecosystems and the services they provide remain not well understood. Furthermore, the ways human society interacts with these ecosystems can be very complex and determine the severity of the climate impacts [Bograd et al. 2019 ; Tam et al. 2019]. The influence of long-term anthropogenic climate change on the social-ecological and environmental dy-

namics of the North Pacific basin is increasingly evident. This impact is particularly strong in the Western Boundary Currents not only of the North Pacific but also of the Atlantic.

The importance of the problem can be described considering Fig. 1.2. The interactions of the ecosystem with human society are often nonlinear and occur over a range of spatial and temporal scales. Thus, the human society which relies heavily on the ocean is negatively impacted by these fluctuations. This makes it crucial to build a forecasting model which can predict future behaviour of particular quantities related to secondary producers called indicators. The indicator acts as proxy to simplify complicated trends in biological, environmental and anthropogenic variables, [Shin and Shannon. 2010]. However, when it comes to forecasting a marine ecosystem some challenges came up. We actually don't have dynamical equations to describe the interaction between climate and ecosystems. Also marine ecosystems present non-linearities and complex behavior which can make them more difficult to predict.

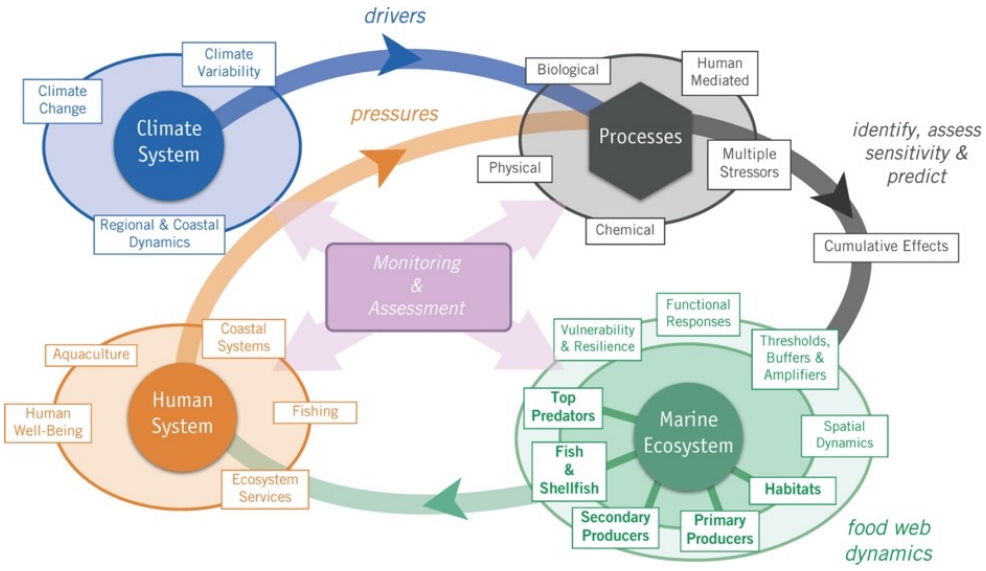

Figure 1.2: (Bograd et al. 2019) The North Pacific Social–Ecological–Environmental System (FUTURE schematic).

In the thesis, we want to further understand the application of Stochastic modeling tools which have been proven to be successful in forecasting the SST in the subtropics. To make these predictions we have used an Empirical Dynamical Model approach (LIM) which has

not yet been applied to include social-ecological state variables. We have applied the LIM to a set of fishery indicators that act as proxies to simplify complicated trends in biological, environmental, and anthropogenic variables. [Shin and Shannon 2010]. It is our goal as a next step to compare these results with the same forecast obtained from a Deep Learning Model.

1.5 References

BIBLIOGRAPHY

[1] E. Di Lorenzo, N. Schneider, K. M. Cobb, P. J.S. Franks, K. Chhak, et al.. North Pacific Gyre Oscillation links ocean climate and ecosystem change. Geophysical Research Letters, American Geophysical Union, 2008, 35, pp.L08607. ff10.1029/2007GL032838ff. ffhal-00634617f

[2] Shin, Y-J., Shannon, L. J., Bundy, A., Coll, M., Aydin, K., Bez, N., Blanchard, J. L., Borges, M. F., Diallo, I., Diaz, E., Heymans, J. J., Hill, L., Johannesen, E., Jouffre, D., Kifani, S., Labrosse, P., Link, J. S., Mackinson, S., Masski, H., Möllmann, C., Neira, S., Ojaveer, H., ould Mohammed Abdallahi, K., Perry, I., Thiao, D., Yemane, D., and Cury, P. M. 2010. Using indicators for evaluating, comparing, and communicating the ecological status of exploited marine ecosystems. 2. Setting the scene. – ICES Journal of Marine Science, 67: 692–716.

[3] Jacox MG, Alexander MA, Siedlecki S, Chen K, Kwon YO, Brodie S, Ortiz I, Tommasi D, Widlansky MJ, Barrie D, Capotondi A, Cheng W, Di Lorenzo E, Edwards C, Fiechter J, Fratantoni P, Hazen EL, Hermann AJ, Kumar A, Miller AJ, Pirhalla D, Pozo Buil M, Ray S, Sheridan SC, Subramanian A, Thompson P, Thorne L, Annamalai H, Aydin K, Bograd SJ, Griffis RB, Kearney K, Kim H, Mariotti A, Merrifield M, Rykaczewski R (2020) Seasonal-to-interannual prediction of North American coastal marine ecosystems: forecast methods, mechanisms of predictability, and priority developments. Progress Oceanogr 183. https://doi.org/10.1016/j.pocean.2020.102307

[4] Bograd SJ, Kang S, Di Lorenzo E, Horii T, Katugin ON, King JR, Lobanov VB, Makino M, Na G, Perry RI, Qiao F, Rykaczewski RR, Saito H, Therriault TW, Yoo S and Batchelder H (2019) Developing a Social–Ecological–Environmental System

Framework to Address Climate Change Impacts in the North Pacific. Front. Mar. Sci. 6:333. doi: 10.3389/fmars.2019.00333

[5] Chiba, S., H. Sugisaki, M. Nonaka, and T. Saino (2009), Geographical shift of zooplankton communities and decadal dynamics of the Kuroshio-Oyashio currents in the western North Pacific, Global Change Biol., 15,1846–1858

[6] Ito, T., Long, M. C., Deutsch, C. A., Minobe, S., & Sun, D. (2019). Mechanisms of low-frequency oxygen variability in the North Pacific, Global Biogeochemical Cycles, 33, 110– 124. https://doi.org/10.1029/2018GB005987

[7] Mantua NJ, Hare SR (2002) The pacific decadal oscillation. Journal of Oceanography, 58, 35–44.

[8] Miller AJ, Chai F, Chiba S, Moisan JR, Neilson DJ (2004) Decadal-scale climate and ecosystem interactions in the North Pacific Ocean. Journal of Oceanography, 60,163–188.

[9] Möllmann, C., and Diekmann, R. (2012). Marine ecosystem regime shifts induced by climate and overfishing. Adv. Ecol. Res. Glob. Change Multispecies Syst. 47, 303–347. doi: 10.1016/b978-0-12-398315-2.00004-1

[10] Tam, Jamie & Fay, Gavin & Link, Jason. (2019). Better Together: The Uses of Ecological and Socio-Economic Indicators With End-to-End Models in Marine Ecosystem Based Management. Frontiers in Marine Science. 6. 560. 10.3389/fmars.2019.00560.

[11] Tommasi, D., Stock, C. A., Hobday, A. J., Methot, R., Kaplan, I. C., Paige Eveson, J., ... Werner, F. E. (2017). Managing living marine resources in a dynamic environment: the role of seasonal to decadal climate forecasts. Progress in Oceanography, 152, 15-49. https://doi.org/10.1016/j.pocean.2016.12.011

[12] Yati E., Minobe S., Mantua N., Ito S.-I., Di Lorenzo E. (2020). Marine Ecosystem Variations Over the North Pacific and Their Linkage to Large-Scale Climate Variability and Change. Front. Mar. Sci. 7. doi: 10.3389/fmars.2020.578165

[13] Bond, N. A., J. E. Overland, M. Spillane, and P. Stabeno (2003), Recentshifts in the state of the North Pacific,Geophys. Res. Lett.,30(23), 2183,doi:10.1029/2003GL018597

[14] Douglass, E., D. Roemmich, and D. Stammer (2006), Interannual variabil-ity in northeast Pacific circulation,J. Geophys. Res.,111, C04001,doi:10.1029/2005JC003015

[15] Ceballos, L. I., E. Di Lorenzo, C. D. Hoyos, N. Schneider, and B. Taguchi (2009), North Pacific Gyre Oscillation Synchronizes Climate Fluctuations in the Eastern and Western Boundary Systems, Journal of Climate, 22(19), 5163-5174, doi:10.1175/2009jcli2848.1

KeelingKeeling, R. F., A. Körtzinger, and N. Gruber (2010), Ocean Deoxygenation in a WarmingWorld,Ann. Rev. of Mar. Sci.,2, 199–229, doi : $10.1146/annurev.marine.010908.163855$.

CHAPTER 2

UNDERSTANDING PAST AND PROJECTED CHANGES IN CLIMATE

This chapter is published as "Navarra, G.G., Di Lorenzo, E. Poleward shift and intensified variability of Kuroshio-Oyashio extension and North Pacific Transition Zone under climate change. Clim Dyn 56, 2469–2486 (2021). https://doi.org/10.1007/s00382-021-05677-0"

2.1 Introduction

The Kuroshio-Oyashio Extension (KOE) represents the western boundary current development of the subtropical gyre. When the Kuroshio and Oyashio currents separate from the Eastern part of Japan, at 35° N they form the KOE, which is characterized by quasi-stationary meanders formed in the Izu-Ogasawara Ridge [Qiu et al. 2002; Qiu et al. 2005]. In this region high interactions between the atmosphere and the ocean take place. The oceanic features of the KOE can be described through heat transfers that are mainly latent and sensible energy fluxes. In particular, the connection between winds and multi-scale ocean variability plays a key role in the climate system by maintaining the surface baroclinicity and energizing storms [Kwon, et al 2010; Sasaki et al. 2011]. The KOE is part of a larger region between the subpolar and subtropical gyre that is also referred to as the North Pacific Transition Zone (NPTZ) (Figure 2.1a, black box). This region is characterized by the presence of a strong chlorophyll-a (CHL-a) front and is defined as the contour where CHL-a equals 0.2 mg m-3 66 . [Ascani et al. 2016; Polovina et al. 2001; Polovina et al. 2015; Sasai et al. 2007]. The seasonal changes of the NPTZ, it is South of the KOE in boreal winter while in Summer it moves North of the jet, making it crucial for physical and biological reasons. Ocean turtles follow the meridional seasonal migrations of the NPTZ, specifically the sharp surface chlorophyll gradient. These migrations of the front are characterized by strong interannual to decadal variability linked to the KOE dynamics and are

evident as a region of high correlation between CHL-a and sea surface height anomalies (SSHa) (Figure 2.1b, black box). The KOE is also known to be one of the major regions of decadal variability in the North Pacific. The origins of these low-frequency fluctuations are linked to both internally generated and externally forced mechanisms. Although some studies suggest that instabilities and eddy mean flow interactions act as an important mechanism for generating internal decadal variability [Yang et al. 2018; Pierini et al. 2009; Taguchi et al. 2010], most studies have identified external atmospheric forcing through the excitation of large-scale ocean Rossby waves as the more dominant driver of KOE decadal variability [Qiu 2003, Qiu 2005, Ceballos et al. 2009, Yang et al. 2017]. Specifically, the low-frequency variability of the KOE and NPTZ is linked to large-scale atmospheric forcing associated with the variability of the Aleutian Low (AL) [Qiu et al. 2007] and the North Pacific Oscillation (NPO) [Ceballos et al. 2009]. The AL and NPO drive the oceanic variability of the PDO and of the North Pacific Gyre Oscillation (NPGO) [Yi et al. 2018], respectively. The adjustment of the PDO and NPGO SSHa is known to excite long Rossby waves in the central and eastern North Pacific that propagate westward towards the western boundary where they energize the decadal variability of the KOE [Minobe, 1999, Taguchi, B., et al. (2005)]. In recent years [Wu et al. 2019] argue that another candidate for the generation of westward propagating Rossby waves is the Atlantic-Multi-decadal Oscillation (AMO). The AMO wind-induced anomalies propagate westward at the speed of the first mode baroclinic Rossby wave. The impact of decadal fluctuations of the KOE on the NPTZ and marine ecosystem is well documented. It has been found that the seasonal migration of juvenile turtles is influenced by the decadal changes in the mean location of the NPTZ in connection with the KOE position and phases of the Pacific Decadal Oscillation (PDO) [Mantua et al. 2002;Ascani et al. 2016]. When the PDO is in the positive phase, that is a positive value of the associated index, the KOE weakens allowing the neonates to move north where they find more productive waters. On the opposite, during a negative phase of the PDO, the KOE strengthen and the loggerhead neonates move South in the less

productive waters of the Subtropical gyre. One explanation of this relation is linked to the way the PDO interacts with primary production. When the AL intensifies (positive phase of the PDO) it leads to an increase in wind stress and the vertical mixing of cold water in the upper ocean. The resulting deepening of the mixed layer leads to less availability of light in the euphotic layer and an overall reduction of zooplankton biomass, [Yatsu et al. 2013; Nakata K. et al.2001]. The loggerhead turtles will then move North to find more productive waters in the Oyashio region. Although the vertical mixing of nutrient is clearly an important driver of ecosystem variability in the KOE, horizontal transport dynamics play an equally important role [Di Lorenzo et al. 2013]. From previous studies, it has been confirmed the role of the AL/PDO in inducing temporal variations in the KOE zooplankton by dominating the seasonal mixed layer process [Chiba et al. 2009]. However, it has also been shown that changes in the NPO/NPGO modify the mean advective transport of the KOE and impact the zooplankton biogeography [Chiba et al. 2013]. Given the reliance of marine ecosystems and fisheries on the interannual and decadal variability of the NPTZ, the goal of this study is to explore how the NPTZ variance responds to a warmer climate predicted by global climate models. Specifically, we examine the Community Earth System Model Large Ensemble (CESM-LENS) projection and compare against an ensemble of climate models from the Coupled Model Intercomparing Project (CMIP5) under the Representative Concentration Pathways RCP8.5. Previous studies have already noted that western boundary currents, such as the KOE, are likely shifting poleward and intensifying as a result of climate warming [Yang et al. 2016;Lorenz et al. 2014], however, it remains unclear if these changes in the mean are also followed by a change in the variability – which may have even more important impacts on marine populations [Sydeman et al. 2013]. The article is organized into sections as follows. The covariance analysis between SSHa and CHL-a is described in Section 3 and it is used to identify the physical signatures of the NPTZ variability in the KOE modes. In Section 4 the future scenario of the SSH variance is described considering the CMIP5-E models and CESM-LE runs. In the last section, the

sea level pressure (SLP) pattern that guides the SSH in the Kuroshio has been considered. The main purpose is to analyze the future scenario of the SSH variance. We also connect this change to the atmospheric influence of SLP variations on KOE and how it will change over time. The importance of considering the variance of SSH is connected to its biological implications.

2.2 Methodology

The SSH altimeter data is produced by the Copernicus Marine Service and it derived by merging. multimission altimeter data from the following missions: Jason-3, Sentinel-3A, HY-2A, Saral/AltiKa, Cryosat-2, Jason-2, Jason-1,T/P, ENVISAT, GFO, ERS1/2. Further description and download of the data is found in https://resources.marine.copernicus.eu/?option=com_csw&task=results?option=com_csw&view=details&product_id=SEALEVEL_GLO_PHY_L4_REP_OBSERVATIONS_008_047

(A more recent version is also available in https://data.marine.copernicus.eu/product/GLOBAL_REANALYSIS_PHY_001_031/description)

For the chlorophyll, we use the data from the ocean Colour CCI project which focuses on the water-leaving radiance in the visible domain. Derived chlorophyll and inherent optical properties utilize data archives from ESA's globally merged MERIS, NASA's SeaWiFS and MODIS sensors archives. It is also looking at the feasibility of using OCM-2 and VIIRS data as a "gap filter" before the launch of Sentinel-3. Further information is found in https://esa-oceancolour-cci.org/ The SSH dataset used in this study has a 0.25° x 0.25° spatial resolution. It covers the period from 1993 to 2017 and consists of monthly mean values. The grid goes from 50°S to 61°N of latitude and from -260 to -50 of longitude. The chlorophyll data have been put on the same spatial grid.

2.2.1 Variance trend calculation

We can describe the method used to obtain the variance. After calculating the absolute value of the first principal component, a Taylor expansion $ytr = x_o + x_1 t + x_2 t_2$ has been considered. In this case t is the length of the ensemble mean first pc. We have then two vectors, one of the coefficients $x = [x_o\ x_1\ x_2 ...]$ and the other of the variable $E = [1\ t\ t^2 ...]$. If we define $y_{tr} = Ex$, the variance is obtained by minimizing the square $min|y - Ex|^2 = 0$

$$J = n^T n = (y - Ex)^T (y - Ex) \tag{2.1}$$

2.2.2 Model output

The data sets used in the model part are two kind of series, a CMIP5-E/historical and a CMIP5-E/RCP8.5. This kind of model is a coupled ocean-atmosphere model where the atmosphere is represented as a stochastic interference in the ocean. For the analyses 23 different types of CMIP5-E models are considered. The reasons why there is not only one model of coupled atmosphere-ocean depends on the fact that the stochastic interference can be treated in many different ways. The list of those models is present in table 1. y is the first principle component. The same procedure has been done for the second pc. This is a kind of linear regression, with a numerical error that depends on when the series is stopped.

CESM-LE model runs

We compare the results of the CMIP5-E with 29 runs of CESM-LE. Two different grids have been considered for SSH and PSL. In the first case, the runs extend from 60°S to 60°N, while for the PSL the models go from 10°N to 90°N, for both cases the resolution is 1 degree. The reason for considering also the CESM-LE runs is that they give the possibility to explore how the variance of the KOE/NPTZ in one model (e.g. a fixed set of dynamics) responds to anthropogenic forcing when compared to the range of natural variability of the CESM-LE model. In the CMIP5-E, we cannot examine the changes in KOE/NPTZ vari-

Table 2.1: CMIP5 models

Model Name	Institution
ACCESS1-0	Australian Community Climate and Earth System Simulator Coupled Model
ACCESS1-3	Australian Community Climate and Earth System Simulator Coupled Model
CESM1-BGC	National Science Foundation, Department of Energy, National Center for Atmospheric Research
CESM1-CAM5	National Science Foundation, Department of Energy, National Center for Atmospheric Research
CMCC-CMS	Centro Euro-Mediterraneo per I Cambiamenti Climatici
CMCC-CM	Centro Euro-Mediterraneo per I Cambiamenti Climatici
CanESM2	Canadian Centre for Climate Modelling and Analysis
EC-EARTH	The First Institute of Oceanography, SOA, China
FGOALS-g2	LASG, Institute of Atmospheric Physics, Chinese Academy of Sciences; and CESS, Tsinghua University
CSIRO-Mk3-6-0	Commonwealth Scientific and Industrial Research Organization in collaboration with the Queensland Climate Change Centre of Excellence
HadGEM2-CC	Met Office Hadley Centre
GISS-ES-R-CC	NASA Goddard Institute for Space Studies
GFDL-ESM2G	Geophysical Fluid Dynamics Laboratory
GFDL-ESM2M	Geophysical Fluid Dynamics Laboratory
GFDL-CM3	Geophysical Fluid Dynamics Laboratory
NorESM1-M	Institut Pierre-Simon Laplace
NorESM1-ME	Norwegian Climate Centre
Inmcm4	Institute for numerical mathematics
bcc-csm1-1-m	Beijing Climate Center, China Meteorological Administration
MPI-ESM-MR	Max Planck Institute for Meteorology (MPI-M)
MIROC-ESM	Japan Agency for Marine-Earth Science and Technology, Atmosphere and Ocean Research Institute (The University of Tokyo), and National Institute for Environmental Studies.
IPSL-CM5A-MR	Institute Pierre-Simon Laplace
IPSL-CM5B-LR	Institute Pierre-Simon Laplace

ance against the natural variability in isolation because an important fraction of variability arises from the "model biases" in their representation of the KOE dynamics and variability. Therefore, the CESM-LE and CMIP-E provide us with different but complementary insights into the climate change response of KOE/NPTZ variability. 380 nm to 750 nm.

2.2.3 Test to evaluate the significance of trends in variance in an ensemble

Here we develop a Monte Carlo approach to test if the changes in variance inferred from ensemble averaging multiple realizations of a time-series are significant. Specifically, we

use this test to estimate the significance of changes in variance found in the principal components of the climate model output. To calculate it we use 10000 random pcs to compare the simulation with the real pc. These random pcs have been used as input for the autoregressive model (AR1-model). The significance is then given by considering the difference in percentage between the real pc and the mean of the pcs calculated randomly.

2.3 Characterizing the North Pacific Transition Zone (NPTZ)

The impact of the physical climate variability of the KOE on the ecological dynamics of the NPTZ is evident from the large-scale co-variability between SSHa and CHL-a anomalies in the NPTZ. A pointwise correlation between satellite SSH and CHL-a anomalies (see methods for data sources) reveal a strong band of negative correlation (R -0.6) extending from Japan to California along the latitudinal boundaries of the NPTZ (Figure 1b, see orange box). The NPTZ region is compatible with the one represented in the paper by [Polovina et al. 2001], where the trajectories of loggerhead turtles are shown. The seasonal movements are to the North during summer, while they are to the South in Winter. The seasonal cycle is not the only influencing factor, the low-frequency variability of the climate modes has a great influence in establishing the migration direction of little turtles [Ascani et al., 2016]. These species change their trajectories if the PDO is in a positive or in a negative phase. Changes in ocean advection related to the NPGO are also found to be critical in determining the zooplankton species distribution in the NPTZ, especially in the KOE region [Chiba et al. 2013]. A physical interpretation of the anti-correlation between SSH and CHL-a anomalies along the NPTZ and California Current System may be given by taking into consideration that the SSH in these regions tracks closely the upper ocean heat content because temperature effects generally dominate over salinity effects. Positive SSH anomalies are associated with warmer sea surface temperatures and higher heat in the upper ocean [Kelly et al. 2010], which in turn are indicative of downwelling conditions and/or reduced flux of nutrients from the deep ocean. The reduced nutrient content in re-

gions of warmer SSTs/higher SSHa leads to less biologically productive waters and lower CHL-a content. Therefore, in the KOE the increase in SSH is associated with an increase of SST. The increase in stratification associated with the SST gradients leads to a decrease in nutrients and chlorophyll. A negative correlation in Fig. 2.1b between the SSH and the chl-a in the Kuroshio extension is then expected [Kouketsu, S., et al. 2016; Storch et al. 1999]. We also observe regions where the correlation between SSH and CHL-a anomalies is positive, especially along the Aleutian Islands and the Gulf of Alaska. In these regions, anti-cyclonic eddies are the primary mechanism supplying high nutrient waters from the coast into the open ocean through lateral advection and vertical mixing of nutrients is a minor control on the overall productivity [Di Lorenzo et al. 2013]. To further examine the relationship between physical and ecosystem variability we perform a more in-depth analysis of the covariance between SSH and CHL-a anomalies. A singular value decomposition (SVD) of the correlation matrix between SSH and CHL-a anomalies in the region on the NPTZ (black box in Figure 2.1b, [-220 -140, 25 50]) reveals that this co-variability tracks the two dominant modes of North Pacific climate variability, the PDO and NPGO (Figure 2.1c, 2.1d, 2.1e, 2.1f). We choose the SVD method as we are dealing with two different fields, the SSH and the CHL-a. The SVD extracts structures that share most covariance between the two fields in a similar way in which the EOF's describe structures that explain most of the variance of an individual variable. Consistent with previous findings [Taguchi et al. 2007] on the climate variability of the KOE, the spatial and temporal patterns of the first singular vector (SVD1) track the PDO (Figure 2.1c and 2.1e) with a strong center of action in the KOE associated with a shift in the position of the NPTZ, while SVD2 tracks the NPGO with a North/South dipole characteristic of a change in the strength of the NPTZ (Figure 2.1d and 2.1f).

The two modes are not only different for spatial structure but also for the quantity of variance explained, that is 25% in Fig.1c and 15% in Fig. 1d.

2.4 Climate Change Projections of NPTZ, CESM-LE vs. CMIP5-E

2.4.1 Changes in mean circulation of the North Pacific Ocean

We now examine the output of long-term climate simulations to explore changes in the mean and variance of the KOE circulation along the NPTZ under the climate warming scenario RCP8.5. Specifically, the CESM-LE large-ensemble (29 members) and an ensemble of CMIP5-E models (23 members) have been considered. The mean ensemble circulation for both the CESM-LE and the CMIP5-E (Figures 2.2a and 2.2e) shows a gyre circulation structure that is consistent with SSH satellite observations. To examine how and if the mean circulation changes under anthropogenic forcing, the difference of the mean SSH 2050-2100 minus 1950-2000 (Figure 2.2b for CESM-LE, Figure 2.2f for CMIP5-E) has been computed. Before calculating the means, a constant equal to the average SSH of the entire Pacific has been subtracted from the SSH. In both ensembles, we find a meridional dipole structure with amplitudes changes 13% of the mean, which projects onto an intensification and northward shift of the mean KOE gradient region.

To better understand the relationship between changes in the mean circulation of the ocean and the atmospheric forcing we examine the Sea Level Pressure (SLP) fields in both the CESM-LE and the CMIP5-E ensemble. Figures 2.3a and 2.3e show the mean SLP for the period 1950-2000 for CESM-LE and CMIP5-E, while Figures 2.3b and 2.3f shows the difference in SLP between the time period 2050-2100 and 1950-2000. In the SLP difference maps, we find a weakening and Northward shift of the Aleutian Low with the center of action at 40°N. In the CMIP5-E and the CESM-LE outputs, we also find a reduction of SLPa over the polar latitudes (> 50°N). These results are consistent with previous studies [Yang et al.2016; Gillett et al. 2013] documenting a climate change signature in SLP similar to the positive phase of the Northern Annular Mode with a poleward shift of the Westerlies linked to negative SLP over high latitudes and positive SLP at mid-latitudes. The difference in mean SLP between present and future climate is not necessarily signif-

icant in terms of absolute value given that the amplitude of the changes is less than the standard deviation (e.g. compare panel f and g in Figure 2.3). However, the changes in the large-scale gradients of SLPa are significant. For example, in the CESM-LE, the gradient between the sub-tropical gyre region (e.g. 50°N) and the pole (e.g. 75°N) changes by 10 Pa (Figure 2.3b), which corresponds to a significant fraction (35%) of the mean gradient of 35 Pa (Figure 2.3a). These changes in the gradient impact the surface winds and ocean circulation. Specifically, the enhanced positive gradient from the subtropical gyre region to the poles leads to stronger downwelling in the subtropical pacific which leads to higher SSH in the subtropics and lower SSH in the subpolar gyre. Consistent with these changes in downwelling/upwelling conditions, the ocean circulation difference maps inferred in the SSH show a poleward shift and intensification in the NPTZ during the period 2050-2100. This climate change signature is also evident by performing an EOF analysis of the ensemble mean SSH of the CESM-LE and CMIP5-E (Figure 2.4). The first EOFs reveals again the same dipolar pattern (Figure 2.4a, 2.4c), and the first principal components are characterized by a strong trend developing at the end of the 21st century (Figure 2.4b, 2.4d). This finding is consistent with previous studies with CMIP5-E models suggesting that the KOE is warming and shifting poleward as a response to anthropogenic forcing [Yang et al. 2016]. Some studies attribute these changes to either an increase in baroclinicity or to an expansion of the Hadley Cell with a poleward shift in the Westerlies [Vallis et al. 2014; Deser et al. 1999]. An alternative explanation has been done by [Chen et al. 2008] for which the increase in temperature leads to a change in the critical latitude of the eddies. As a consequence, there is a poleward shift of eddy momentum flux and also of the Westerlies. The climate spatial trends in the mean SLP changes emerge also in the first EOF of SLPa where the trends have not been removed (Figure 2.4c for CESM-LE and Figure 2.4g for CMIP5-E). However, the ensemble means first principal component in CESM-LE and CMIP5-E (Figure 2.4b, 2.4f) do not show strong trends because the changes in mean SLP are weak compared to the standard deviation of the field.

2.4.2 Changes in the Variability of the NPTZ

Both the CESM and CMIP5 ensemble captures the structure of the mean spatial variance of SSHa over the North Pacific with strong values in the KOE region (Figure 2.2c and 2.2g). To quantify how the variability of the NPTZ changes under anthropogenic forcing, we compute the difference in the mean spatial variance for the period 2050-2100 minus 1950-2000 for both the CESM-LE (Figure 2.2d) and CMIP5-E (Figure 2.2h) ensemble. Both the CMIP5-E and the CESM-LE runs gives a significant increase in the mean SSH that is associated with a lower increase of variance in the Kuroshio extension region. The increased SSH gradient (Figure 2.2 b and Figure 2.2f) works to intensify the midlatitude westerlies resulting in an increasing wind stress curl field. As the subtropical gyre increases the SSH mean, as we can see from the southern recirculation gyre, the corresponding intensification of poleward heat transport reverse this effect. To further understand the dynamics underlying the changes in variance, and how it impacts the NPTZ, we decompose the variance using EOF analyses. Specifically, we consider the spatial domain [215W-140W;30N-50N] that was used to extract the two dominant modes of SSHa-CHL-a co-variability (Figure 2.1c and 2.1d) associated with a shift in positions and changes in the intensity of the NPTZ circulation. Before the computation of the EOFs, we remove the anthropogenic signals in the CESM-LE and CMIP5-E (see methods) to focus on changes in the variability that are not influenced by the anthropogenic trends. For each model realizations, we compute the first two modes and align the signs of each mode so that the spatial expressions are consistent in sign with that of the observations in Figure 2.1. We then take the ensemble mean of the spatial patterns for the CESM-LE and CMIP5-E simulations. We find the spatial structure of the first two modes of SSHa, in both CESM-LE (Figure 2.5) and CMIP5-E (Figure 2.6), track closely the modes derived from observations (Figure 1c and 1d), suggesting that the climate models capture realistically the dominant structures of SSHa variance over the NPTZ region. The first SSHa mode reveals a strong pole over the NPTZ region that is consistent with a shift in the axis of the KOE (Figure 2.1c) and tracks the PDO mode of

the models (e.g. In supplemental materials the PDO index has been computed by using the SSH anomalies and compared with the same index with the SST anomalies). The second mode reveals a meridional dipole associated with a change in the strength of NPTZ gradient and tracks the NPGO indices in each model. We now explore the changes in variance in the two dominant modes of NPTZ variability and test if there are any significant changes over the period 1920-2100. For the CESM-LE, we begin by taking the absolute value to the individual PC1 realizations (Figure 2.5c, gray line), we then average the PC1s together (Figure 2.5c, the ensemble mean is the black bold line) and fit a quadratic trend model (Figure 2.5c, green line,$y(t) = at + bt^2$) to estimate the long-term changes in variance. The percentage change in variance with respect to 1920 values is found by scaling the trend by the value on January 1920 and multiplying by 100 (Figure 5e, green line). The same procedure is repeated using only winter (Figure 2.5e, blue line) and summer (Figure 2.5e, red line) values to understand if there are seasonal dependences in the trend of the variance. In the case of CESM-LE PC1, we find a significant increase in the total variance of about 20% by 2100, with about 25% in the summer and 10% in the winter (see below for the significance test). The second mode of the CESM-LE also shows a very significant increase in variance (Figures 5c and 5f) with a predicted amplification of about 30% by 2100. Test of significance for the ensemble trend in variance: To assess if the trends of variance in the ensemble average are significant (e.g. green line, Figure 2.5c), we develop a Monte Carlo approach that simulates the trend estimation process used to derive the ensemble trend in variance shown in Figure 2.5 (green line). Specifically, we generate 10,000 random realizations of the ensemble trend (gray spread, Figure 2.5e and Figure 2.6e). Each random trend line is generated by applying the quadratic trend fit on 30 random PC1s red noise time series that have the same autocorrelation as in the original 30 PC1s of the CESM ensemble. This test is also repeated for estimating the significance of the PC2 trends in variance (gray spread, Figure 2.5f, and Figure 2.6f). To understand if the predicted changes in variance from the CESM ensemble are robust, we perform the same trend analyses for the CMIP5-

E. We obtained that the trend in variance for PC1 is confirmed in the CMIP5-E with a total variance increase 10% (Figure 2.6e). However, for PC2, the CMIP5 ensemble does not predict a significant change in variance (Figure 2.6f). The lack of a significant trend in the PC2 running variance reveals an important discrepancy between the CMIP5-E and the CESM-LE scenario, which may indicate a high level of uncertainty emerging from the model's inability to reproduce a consistent NPGO dynamics e.g. [Furtado et al. 2011]

2.5 Correlation SLP forcing index with SSH_{PC1} and SSH_{PC2}

To further understand and verify the relation between the SLPa forcing timeseries and the SSHa PCs, a simple statistical model has been developed to relate changes in SSHa to SLPa forcing,

$$\frac{\partial SSH_{PC1}(t)}{\partial t} = SLPa_{forcing}(t) - \gamma SSH_{PC1}(t) \tag{2.2}$$

Following the approach of [Frankignoul and Hasselman 1977], Eq. 2.2 represents a simple model of a climate system where the rate of change of the SSHa is forced by the atmospheric SLPa and decays back to zero with a damping time scale defined by $1/\gamma$. Negative feedback leads to an asymptotic balance between the random forcing and the feedback damping yielding to a statistically stationary response. If we consider $SLPa = [SLPa] + SLPa_{forcing}(t)$, in an equilibrium condition the mean value of SLPa can be considered negligible. In this way, the response of the climate system to the continuous random forcing is represented as a first-order autoregressive model (AR-1 model). At the same time the meaning of the coefficient γ is explained by looking at the autocorrelation of the red noise, $r(t) = exp(\frac{t}{\tau})$, τ is the time lag while γ represents the damping rate given by the inverse of the autocorrelation decay time T. We analyze the influence of the forcing factor represented by the $SLPa_{forcing}$ on the SSH_{PC1} by calculating the correlation between the two indices. In Fig. 2.9a and 2.9c the ensemble mean correlation has been done for the SSH_{PC1} and the forcing index obtained from integration of SLP_{PC1}. A correlation

of 0.64 for CESM and 0.49 for CMIP5 has been obtained. To estimate the significance of the correlations the PDF of cross-correlation coefficients is represented in the same figures. To build the PDF we examine the correlation of 1000 random pairs that have the same autocorrelation of the two-time series considered. In Fig.2.9b and 2.9d the SLP forcing index from model (equation 2.2) is calculated with SLP_{PC2}. In this case, the ensemble mean correlation of the index with SSH_{PC2} gives a correlation of 0.57 for CESM-LE and 0.45 for CMIP5-E. To further understand the relationship between the atmospheric forcing and the KOE, we adopt a lag correlation analysis proposed by [Frankignoul et al. (1998)]. The essence of this approach is to examine the correlation between an atmospheric variable, the SLPa field, and the SSH_{PC1} (Supplemental Materials) with a lag that is longer than the intrinsic atmospheric timescale (2 month, [Deser et al. 2007]). The resulting correlation maps show significant correlation patterns similar to Fig.2.7a and Fig.2.8a when the SLPa patterns lead the SSHa PCs by 12 months. This confirms that the SLP acts as a forcing of the KOE SSH and NPTZ. To explain this leading time, we can consider that when the Aleutian Low intensifies (positive phase of the PDO) it cools the Central North Pacific and generates SSH anomalies through Ekman divergence. [Kwon et al. 2010]. It also has been found by other studies [Ceballos et al.2009] that the Rossby waves generated by NPO-induced SLP anomalies can have an impact on the KOE. The time of wave propagation gives rise to the time lag of 6-12 month.

2.6 Conclusions

The presence of strong chlorophyll gradients makes the NPTZ a region of great importance for ecosystem dynamics. Changes in the location and amplitude of the chlorophyll gradient are strongly connected to changes in the KOE dynamic circulation. This is evident from the dominant modes of covariability between SSHa and chlorophyll-a in the KOE region in satellite observations (Fig. 2.1). The first mode represents a meridional shift in location of the KOE/NPTZ and tracks the PDO, whereas the second mode has a dipole structure

and describes an intensification of the KOE mean circulation and the NPTZ. To understand the impact of anthropogenic forcing on the NPTZ, we examine the projected changes in the characteristics of the KOE physical modes using the Community Earth System Model Large Ensemble (CESM-LE) and 23 CMIP5-E models. We consider the change in SSH mean and variance between two time periods, 1950-2000 and 2050-2100 (Fig. 2.2 and 2.3). The SSH mean difference map gives a meridional dipole structure that projects onto an intensification and Northward shift of the KOE and NPTZ. The poleward shift is also associated with a Northward movement of the Aleutian Low as revealed by the SLP mean difference maps. A shift in the North Pacific atmospheric circulation has been previously examined. [Vallis et al. (2015)] found a correlation between the expansion of the Hadley cell and the poleward shift of the Westerlies and the corresponding ocean circulation imprint. An alternative explanation is given by [Chen et al. (2008)], which argue that as a consequence of global warming the phase speed of mid latitude atmospheric eddies increases. This leads to a poleward shift of the eddy-momentum flux and, as a consequence, of the Westerlies.

Several studies have recognized that changes in climate variance, rather than changes in the mean, are a better predictor of phase and regime shifts in a variety of oceanic systems [Sydeman et al. 2013]. We have explored the changes in the NPTZ variance by examining the two dominant modes of detrended KOE SSHa (Fig 5 and Fig. 6) in the CESM-LE and CMIP5 ensemble. A Monte Carlo test has been done to test the significance of the trend. The CESM-LE suggests a 20% increase in the SSHa of SSH PC1 while for the CMIP5-E models the increase is almost 15%. We found that the increase in SSH variance is associated with trends in the variability of the corresponding SLP forcing patterns (e.g. SLP PC1) (Fig. 2.7 and 2.8). For SSH PC2, the CESM-LE predicts a very significant trend in variance with changes up to $30-40\%$. However, in the CMIP5-E this trend is not as significant, and the corresponding forcing patterns in SLP do not exhibit clear trends (e.g. SLP PC2). This may indicate that changes in the variance of the CESM-LE second mode, and

to some degree of CMIP5-E, are driven by internal ocean processes linked to the changes in the mean circulation. To further examine the relation of the SSHa modes (SSH PC1 and SSH PC2) to atmospheric forcing in the KOE we apply a simple auto-regressive model of order 1 forced by indices of the SLPa forcing patterns (SLP PC1 and SLP PC2) (eq. 2.4). The reconstructions of SSH PC1 in the CESM-LE gives a correlation of 0.71 while for the CMIP5 the values are lower, 0.45. Lower correlation values are found in the reconstruction of SSH PC2 with a correlation of 0.57 for the CESM-LE and 0.39 for CMIP5-E. The weaker correlation in the reconstruction of the second SSHa mode further confirms the role of internal ocean dynamics in controlling its variability. The changes in KOE circulation and NPTZ identified in this study have several biological implications. In addition to the co-variability between the SSHa and CHL-a, which can be considered a proxy for primary productivity, the variability of the NPTZ is linked to higher-trophic ecosystem dynamics. For example, changes in the intensity of the KOE circulation, captured by the second SSHa mode, have been linked to the alternation of zooplankton species found in the NPTZ [Chiba et al. 2009]. Similarly, meridional shift in the axis of the NPTZ associated with changes in the AL intensity, captured by the first SSHa mode, are linked to changes in the overall biomass of zooplankton [lower biomass during stronger AL, [Nakata et al. 2001] and changes in migration patterns marine turtles [Ascani et al. 2016]. While these links between the NPTZ variability and marine ecosystem dynamics clearly indicate that marine populations respond to the SSHa modes of variability, it remains unclear how a trend in the variance of these modes will impact ecosystem function. Rising trends in climate variance are accompanied by rising levels of synchrony (e.g. covariability) [Black et al. 2018]. Such a rise in synchrony may destabilize the ecosystems and expose populations to higher risks of extinction by reducing the so-called "portfolio effect". Specifically, when marine populations respond more synchronously to the same perturbations, they become less resilient and more susceptible to sudden collapses with disruptions of the ecosystem services they provide e.g. [Moran 1953].

2.7 References

Ascani, F., K. S. Van Houtan, E. Di Lorenzo, J. J. Polovina, and T. T. Jones (2016), Juvenile recruitment in loggerhead sea turtles linked to decadal changes in ocean circulation, Glob. Change Biol., 22(11),3529-3538, doi:10.1111/gcb.13331.

B. Black, P. van der Sleen, E. Di Lorenzo, et al. Rising synchrony controls western North American ecosystems Glob Change Biol. 2018; 24:2305–2314. https://doi.org/10.1111/gcb.14128

Ceballos, L. I., E. Di Lorenzo, C. D. Hoyos, N. Schneider, and B. Taguchi (2009), North Pacific Gyre Oscillation Synchronizes Climate Fluctuations in the Eastern and Western Boundary Systems, Journal of Climate, 22(19), 5163-5174, doi:10.1175/2009jcli2848.1.

Chen, G., J. Lu, and D.M. Frierson, 2008: Phase Speed Spectra and the Latitude of Surface Westerlies: 504 Interannual Variability and Global Warming Trend J. Climate, 21, 5942–5959, 505 https://doi.org/10.1175/2008JCLI2306.1

Chiba, S., E. Lorenzo, A. Davis, J. E. Keister, B. Taguchi, Y. Sasai and H. Sugisaki, 2013: Large-scale climate control of zooplankton transport and biogeography in the Kuroshio-Oyashio Extension region. Geophysical Research Letters, 40(19) 5182-5187, doi:10.1002/grl.50999.

Chiba, S., H. Sugisaki, M. Nonaka, and T. Saino (2009), Geographical shiftof zooplankton communities and decadal dynamics of the Kuroshio-Oyashio currents in the western North Pacific, Global Change Biol., 15,1846–1858

Di Lorenzo, E., V. Combes, J.E. Keister, P.T. Strub, A.C. Thomas, P.J.S. Franks, M.D.

Ohman, J.C. Furtado, A. Bracco, S.J. Bograd, W.T. Peterson, F.B. Schwing, S. Chiba, B. Taguchi, S. Hormazabal, and C. Parada. 2013. Synthesis of Pacific Ocean climate and ecosystem dynamics. Oceanography 26(4):68– 81, https://doi.org/10.5670/oceanog.2013.76.

Di Lorenzo, E., D. Mountain, H.P. Batchelder, N. Bond, and E.E. Hofmann. 2013. Advances in marine ecosystem dynamics from US GLOBEC: The horizontal-advection bottom-up forcing paradigm. Oceanography 26(4):22–33, https://doi.org/10.5670/oceanog.2013.73.

Deser, C., R.A. Tomas, and S. Peng, 2007: The Transient Atmospheric Circulation Response to North Atlantic SST and Sea Ice Anomalies. J. Climate, 20, 4751–4767, https://doi.org/10.1175/JC

Deser, C., M.A. Alexander, and M.S. Timlin, 1999: Evidence for a Wind-Driven Intensification of the Kuroshio Current Extension from the 1970s to the 1980s. J. Climate, 12, 1697–1706, https://doi.org/10.1175/1520-0442(1999)012¡1697:EFAWDI¿2.0.CO;2

Frankignoul, C., A. Czaja, and B. L'Heveder, 1998: Air-Sea Feedback in the North Atlantic and Surface Boundary Conditions for Oceans Models. J. Climate, 11, 2310–2324, https://doi.org/10.1175/1520- 0442(1998)011¡2310:ASFITN¿2.0.CO;2

Furtado, J. C., E. Di Lorenzo, N. Schneider and N. A. Bond, 2011: North Pacific Decadal Variability and Climate Change in the IPCC AR4 Models. Journal of Climate, 24(12) 3049-3067, doi:10.1175/2010jcli3584.1.

Frankignoul & Klaus Hasselmann (1977) Stochastic climate models, Part II Application to sea-surface temperature anomalies and thermocline variability, Tellus, 29:4, 289-305, DOI: 10.3402/tellusa.v29i4.11362

Gillett, N. Fyfe, J. (2013). Annular mode changes in the CMIP5 simulations. Geophysical Research Letters. 40. 1189-1193. 10.1002/grl.50249.

Joh, Y., & Di Lorenzo, E. (2017). Increasing coupling between NPGO and PDO leads to prolonged marine heat waves in the Northeast Pacific. Geophysical Research Letters,44,11,663–11,671. https://doi.org/10.1002/2017GL075930

Kay, J.E., C. Deser, A. Phillips, A. Mai, C. Hannay, G. Strand, J.M. Arblaster, S.C. Bates, G. Danabasoglu, J. Edwards, M. Holland, P. Kushner, J. Lamarque, D. Lawrence, K. Lindsay, A. Middleton, E. Munoz, R. Neale, K. Oleson, L. Polvani, and M. Vertenstein, 2015: The Community Earth System Model (CESM) Large Ensemble Project: A Community Resource for Studying Climate Change in the Presence of Internal Climate Variability. Bull. Amer. Meteor. Soc., 96, 1333–1349, https://doi.org/10.1175/BAMS-D-13-00255.1

Kelly, K. A., et al. (2010). "Western Boundary Currents and Frontal Air–Sea Interaction: Gulf Stream and Kuroshio Extension." Journal of Climate 23(21): 5644-5667

Kouketsu, S., et al. (2016). "Mesoscale eddy effects on temporal variability of surface chlorophyll a in the Kuroshio Extension." Journal of Oceanography 72(3): 439-451.

Kwon, Y., M.A. Alexander, N.A. Bond, C. Frankignoul, H. Nakamura, B. Qiu, and L.A. Thompson, 2010:Role of the Gulf Stream and Kuroshio-Oyashio Systems in Large-Scale Atmosphere-Ocean Interaction: A Review. J. Climate, 23, 3249–3281, https://doi.org/10.1175/2010JCLI3

Lorenz, D.J., 2014: Understanding Midlatitude Jet Variability and Change Using Rossby

Wave Chromatography: Poleward-Shifted Jets in Response to External Forcing. J. Atmos. Sci., 71, 2370– 2389, https://doi.org/10.1175/JAS-D-13-0200.1

Mantua, Nathan Hare, Steven. (2002). The Pacific Decadal Oscillation. Journal of Oceanography. 58. 35- 44. 10.1023/A:1015820616384.

Minobe S., Resonance in bidecadal and pentadecadal climate oscillations over the North Pacific: role in climate regime shif, Geophysical Research Letters, 1999, vol.26(pg.855-858)

Nakata K., Koyama S., Matsukawa Y. Interannual variation in spring biomass and gut content composition of copepods in the Kuroshio current, 1971–89, Fisheries Oceanography, 2001, vol. 10 (pg. 329-341)

Polovina, Jeffrey & Howell, Evan & Kobayashi, Donald & Seki, Michael. (2015). The Transition Zone Chlorophyll Front Updated: Advances from a decade of research. Progress in Oceanography. 10.1016/j.pocean.2015.01.006.

Polovina, Evan Howell, Donald R Kobayashi, Michael P Seki, The transition zone chlorophyll front, a dynamic global feature defining migration and forage habitat for marine resources, Progress in Oceanography,Volume 49, Issues 1–4,2001, Pages 469-483, ISSN 0079-6611, https://doi.org/10.1016/S0079-6611(01)00036-2.

Pierini, S. and Dijkstra, H. A.: Low-frequency variability of the Kuroshio Extension, Nonlin. Processes Geophys., 16, 665–675, https://doi.org/10.5194/npg-16-665-2009, 2009.

Qiu, B. The Kuroshio Extension System: Its Large-Scale Variability and Role in the Midlatitude Ocean- Atmosphere Interaction. Journal of Oceanography 58, 57–75 (2002). https://doi.org/10.1023/

Qiu, B. and S. Chen, 2005: Variability of the Kuroshio Extension Jet, Recirculation Gyre, and Mesoscale Eddies on Decadal Time Scales. J. Phys. Oceanogr., 35, 2090–2103, https://doi.org/10.1175/JPO2807.1

Qiu, B., (2003): Kuroshio Extension Variability and Forcing of the Pacific Decadal Oscillations: Responses and Potential Feedback. J. Phys. Oceanogr., 33, 2465–2482, https://doi.org/10.1175/2459

Qiu, B., et al. (2007). "Coupled decadal variability in the North Pacific: An observationally constrained idealized model." Journal of Climate 20(14): 3602-3620

Sasaki, Y.N. and Schneider, N. (2011) Decadal shifts of the Kuroshio extension jet: application of thin-jet theory. Journal of Physical Oceanography, 41(5), 979– 993. https://doi.org/10.1175/2011JP

Sydeman, W. J., J. A. Santora, S. A. Thompson, B. Marinovic, and E. Di Lorenzo (2013), Increasing variance in North Pacific climate relates to unprecedented ecosystem variability off California, Glob. Change Biol., 19(6), 1662-1675, doi:10.1111/gcb.12

Sasai, Yoshikazu & Sasaoka, Kosei Sasaki, Hideharu & Ishida, Akio. (2007). Seasonal and intraseasonal variability of chlorophyll-a in the North Pacific: model and satellite data. Journal of the Earth Simulator. 8. 3-11.

S. Chiba, H. Sugisaki, M. Nonaka, T. Saino Geographical shift of zooplankton communities and decadal dynamics of the Kuroshio–Oyashio currents in the western North Pacific,

Global Change Biology, 15 (2009), pp. 1846-1858

Sonnewald, M., C. Wunsch, and P. Heimbach, 2018: Linear Predictability: A Sea Surface Height Case Study. J. Climate, 31, 2599–2611, https://doi.org/10.1175/JCLI-D-17-0142.1

Storch, H., & Zwiers, F. (1999). Statistical Analysis in Climate Research. Cambridge: Cambridge University Press. doi:10.1017/CBO9780511612336

Taguchi, Bunmei & Qiu, Bo & Nonaka, Masami & Sasaki, Hideharu & Xie, Shang-Ping & Schneider, Niklas. (2010). Decadal variability of the Kuroshio Extension: Mesoscale eddies and recirculation. Ocean Dynamics. 60. 673-691. 10.1007/s10236-010-0295-1.

Taguchi, B., S. Xie, N. Schneider, M. Nonaka, H. Sasaki, and Y. Sasai, 2007: Decadal Variability of the Kuroshio Extension: Observations and an Eddy-Resolving Model Hindcast. J. Climate, 20, 2357– 2377, https://doi.org/10.1175/JCLI4142.1

Taguchi, Bunmei & Xie, Shang-Ping & Mitsudera, Humio & Kubokawa, Atsushi. (2005). Response of the Kuroshio Extension to Rossby Waves Associated with the 1970s Climate Regime Shift in a High- Resolution Ocean Model*. Journal of Climate - J CLIMATE. 18. 10.1175/JCLI3449.1.

TOPEX/Poseidonand ERS-1 and -2.J. Geophys. Res.,105,19 477–19 498,doi:10.1029/2000JC900063

Yang, Y., X. San Liang, B. Qiu, and S. Chen, 2017: On the Decadal Variability of the Eddy Kinetic Energy in the Kuroshio Extension. J. Phys. Oceanogr., 47, 1169–1187,

https://doi.org/10.1175/JPO-D-16- 0201.1

Yang, H., G. Lohmann, W. Wei, M. Dima, M. Ionita, and J. Liu (2016), Intensification and poleward shift of subtropical western boundary currents in a warming climate, J. Geophys. Res.Oceans,121, 4928–4945, doi:10.1002/2015JC011513

Yatsu, A., Chiba, S., Yamanaka, Y., Ito, S-I., Shimizu, Y., Kaeriyama, M., and Watanabe, Y. 2013. Climate forcing and the Kuroshio/Oyashio ecosystem. – ICES Journal of Marine Science, 70: 922–933

Yi, D.L., B. Gan, L. Wu, and A.J. Miller, 2018: The North Pacific Gyre Oscillation and Mechanisms of its Decadal Variability in CMIP5 Models. J. Climate, 31, 2487–2509, https://doi.org/10.1175/JCLI-D- 17-0344.1

Vallis, G. K., P. Zurita-Gotor, C. Cairns, and J. Kidston, 2015: Response of the large-scale structure of the atmosphere to global warming. Quart. J. Roy. Meteor. Soc.,141, 1479–1501, https://doi.org/10.1002/qj.2456

Wu, B., Lin, X. & Qiu, B. On the seasonal variability of the Oyashio extension fronts. Clim Dyn 53, 7011–7025 (2019). https://doi.org/10.1007/s00382-019-04972-1

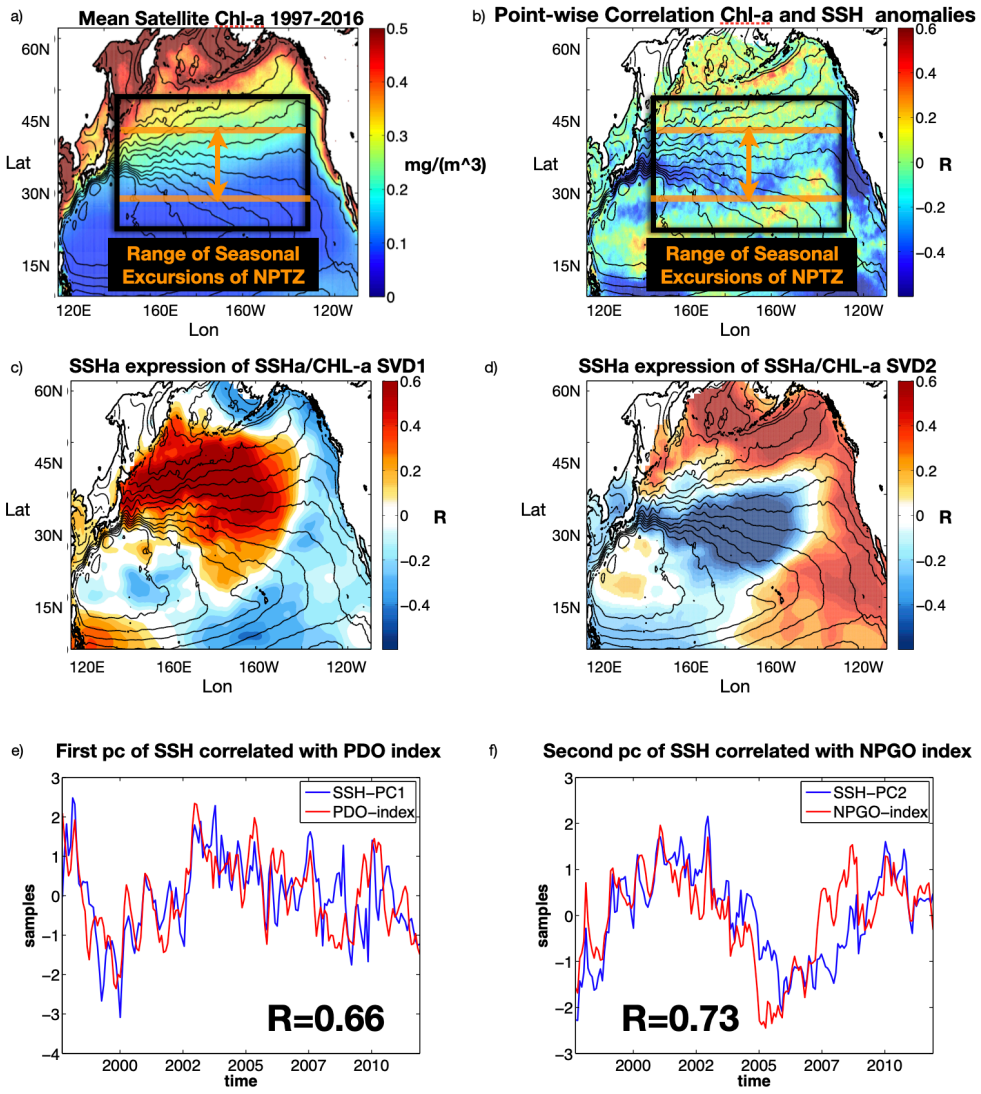

Figure 2.1: in part a) the mean chlorophyll concentration is shown with particular relevance to the NPTZ area. (b) represents the total correlation between SSH and the chlorophyll. In (c) and (d) instead correlation maps between SSH anomalies with the first pc and second pc are explained. The former case, is displayed in c) while the correlation with the second pc is in (d). Then the last two represents how the first pc correlates with the PDO index (e) and how the second pc correlates with the NPGO index (f)

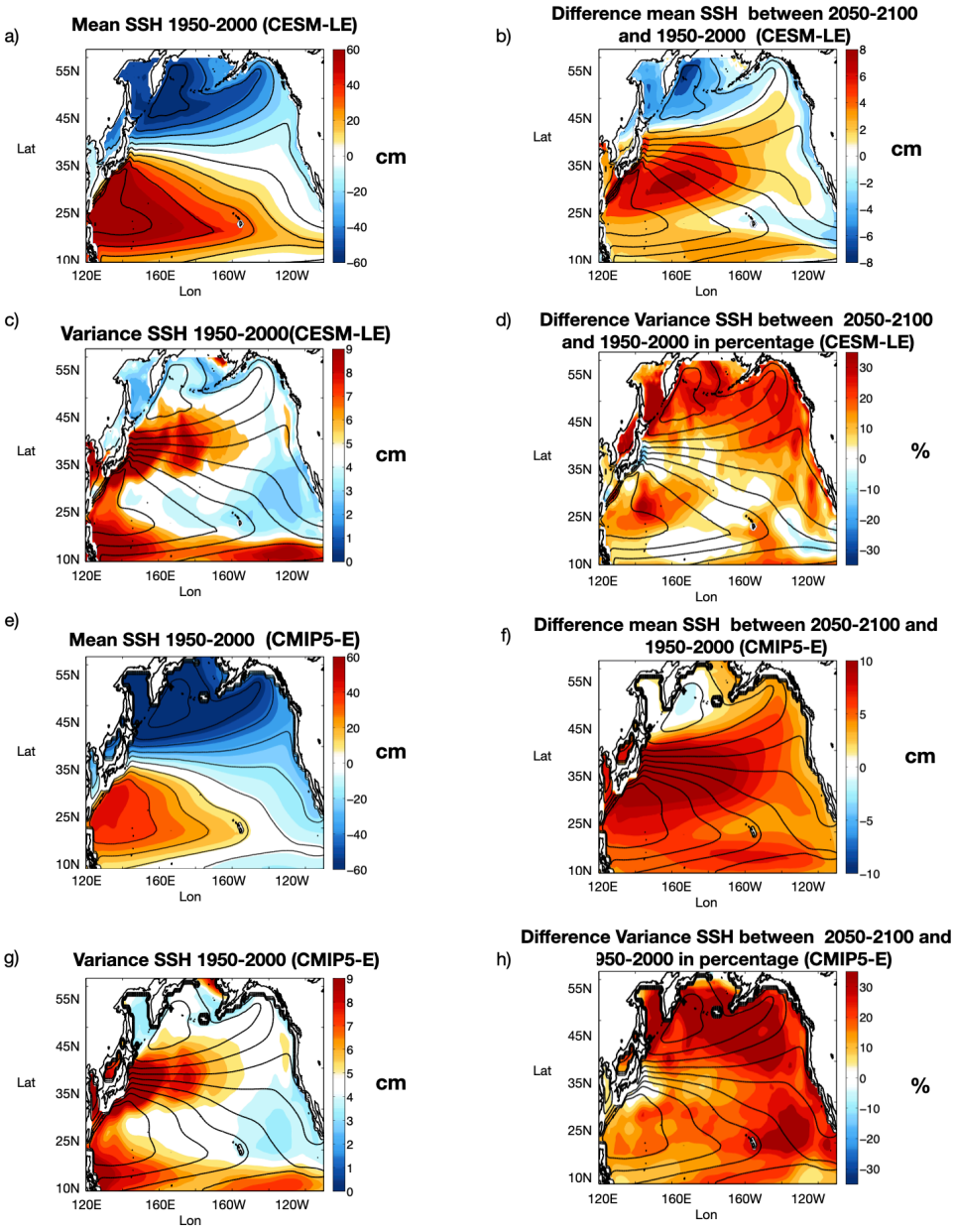

Figure 2.2: CESM-LE and CMIP5-E difference maps for SSH. In part (a) the mean SSH in the period 1950-2000 is explained, the black lines represents the contour of the mean SSH in this period. In b) the difference between 1950-2000 and 2050-2100 SSH is calculated. In (c) and (d) the same is done but for the variance of the SSH. In (e)-(h) figures the same procedures has been followed but with CMIP5-E models. Units of SSH are in cm

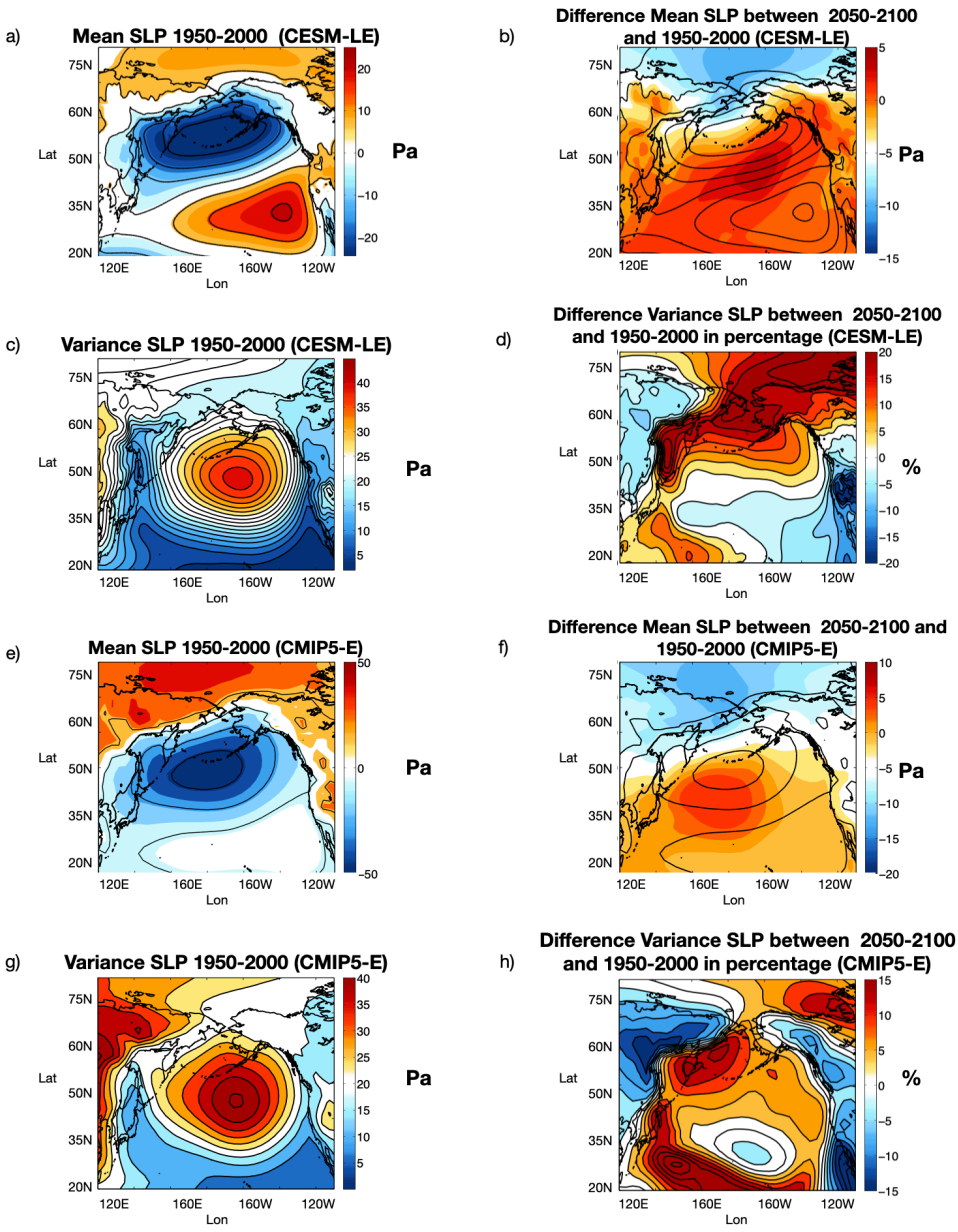

Figure 2.3: CESM-LE and CMIP5-E difference maps for SLP. In (a) the mean SSH in the period 1950-2000 is explained, the black lines represents the contour of the mean SSH in this period. In b) the difference between 1950-2000 and 2050-2100 SSH is calculated. In c) and d) the same is done but for the variance of the SSH. In (e)-(h) figures the same procedures has been followed but with CMIP5-E models. Units of SSH are in cm

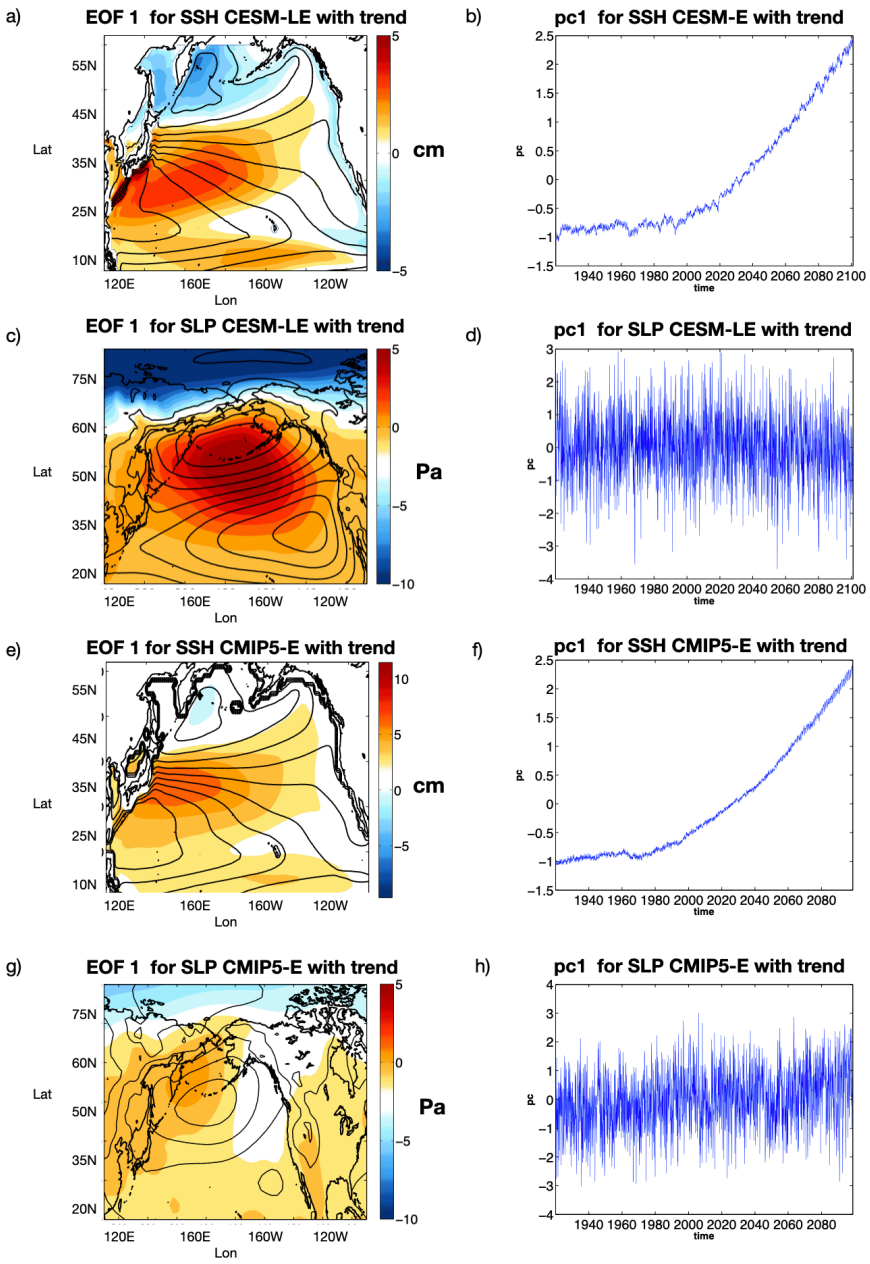

Figure 2.4: In (a) the first EOFs with trend is displayed. There is a clear pattern in the region of the Kuroshio. In b) the first pc associated to this EOF is represented. This gives a clear increasing trend. Then the same EOF is calculated for the SLP in (c).In this case the first pc explain an stable scenario. In (e)-(h) the same figure have been done but with the CMIP5 models. Units of SSH are in cm, while for the SLP Units are in Pa.

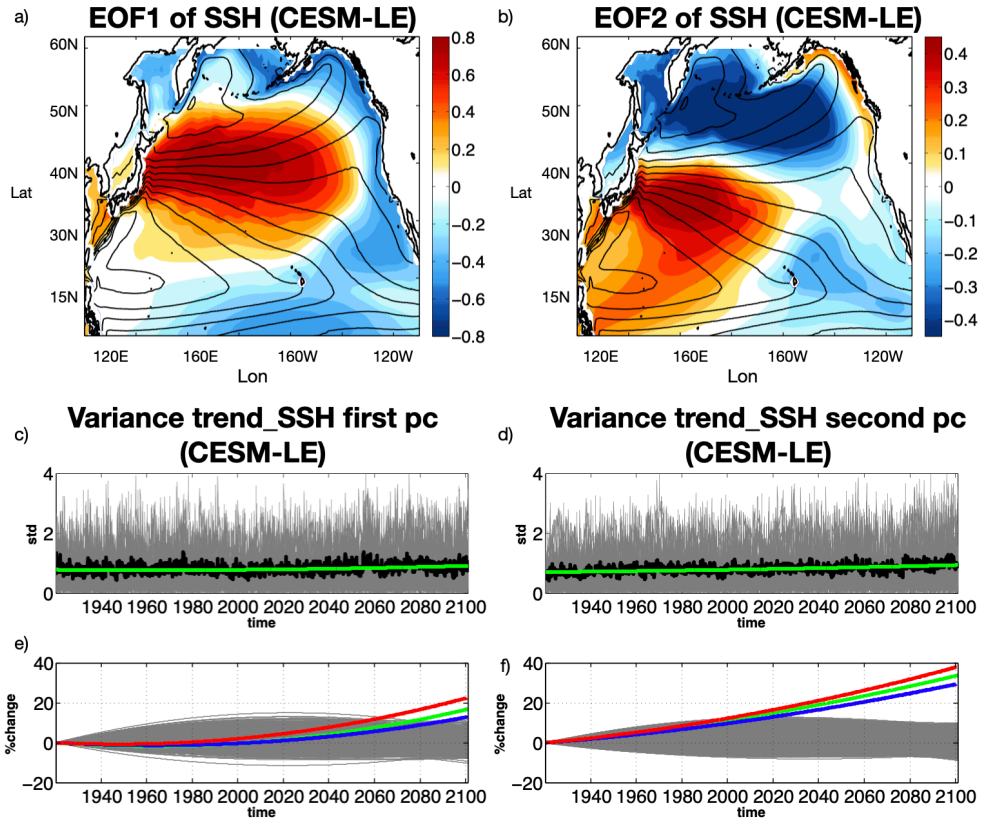

Figure 2.5: In (a) and (b) the first and second EOF for the SSH anomalies are represented. Here the trend has been removed, compared to Fig.2.4. The trend in the variance corresponding to the first EOF is displayed in (b). In this latter one the top figure displayed the principal component and the mean pc(in black). In the bottom figure instead, the trend of the variance is represented. In (g) and (h) the pdf associated with the random samples (grey part in (e) and (f)) is calculated. In this case the CESM output is taken into consideration. Units of SSH are in cm.

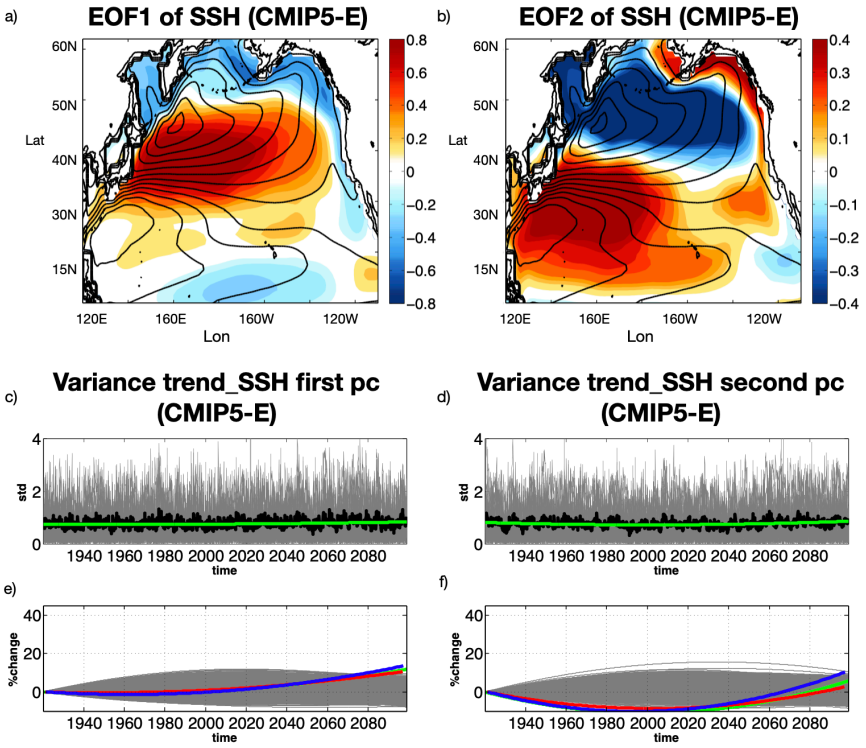

Figure 2.6: In (a) and b) the first and second EOF for the SSH anomalies are represented. Here the trend has been removed, compared to Fig.2.4. The trend in the variance corresponding to the first EOF is displayed in (b). In this latter one, the top figure displayed the principal component and the mean pc(in black). In the bottom figure instead, the trend of the variance is represented. In (g) and (h) the pdf associated to the random samples (grey part in (e) and (f)) is calculated. In this case, the CMIP5 output is taken into consideration . Units of SSH are in cm.

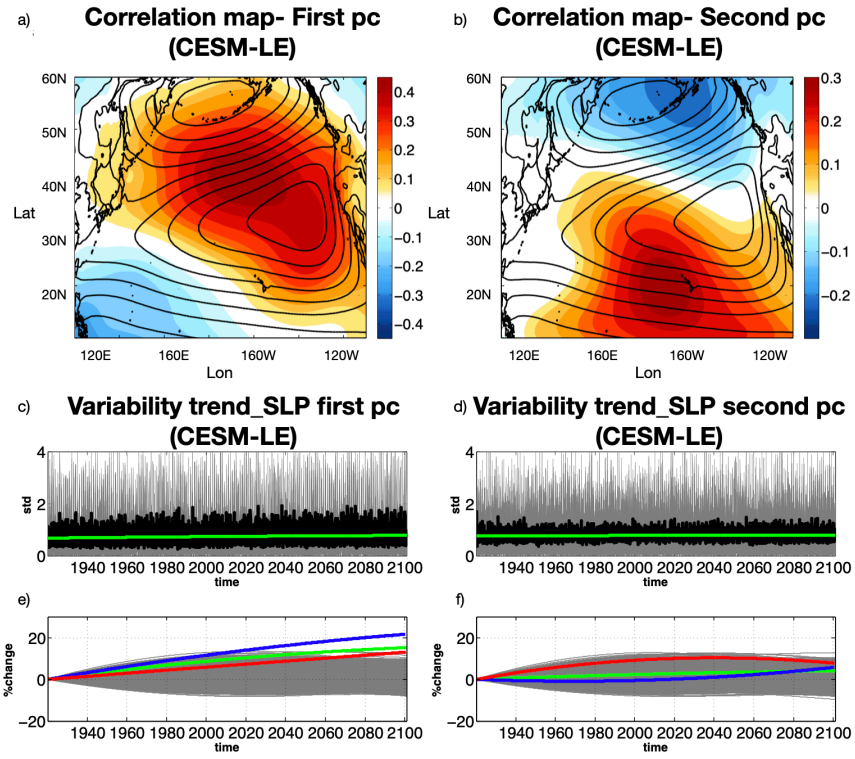

Figure 2.7: In (a) the first correlation pattern for the SLP anomalies over the first pc of SSH is represented. The trend in the variance corresponding to the first pattern is displayed in (c). The principal components for each single runs are the grey part while the mean pc is in black. The trend of the variance is given by the green line. In (e) the percentage increase is calculated. The red line is the increase for just the summer season, while the blue line regards the winter season. In (b) the second correlation pattern associated to the SLP anoamlies projected over the second pc of SSH is displayed. The trend in the variance corresponding to the first pattern is described in (d) while the associated percentage increase is in (f). The grey part in (e) and (f) describe the significance test performed. In this case CESM runs are taken into consideration. Units of SSH are in cm.

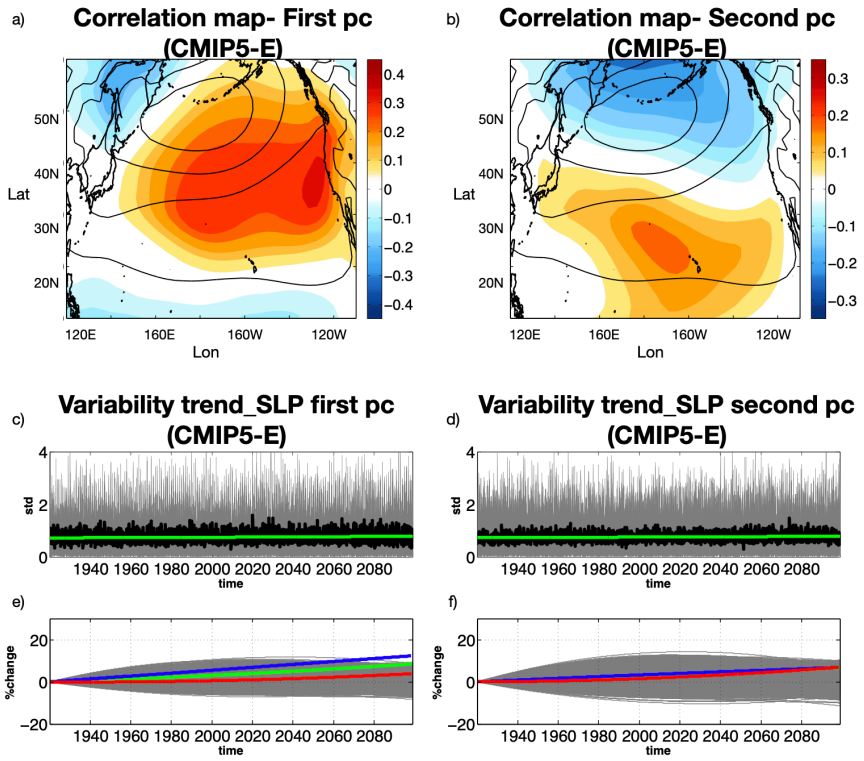

Figure 2.8: In (a) the first correlation pattern for the SLP anomalies over the first pc of SSH is represented. The trend in the variance corresponding to the first pattern is displayed in (c). The principal components for each single runs are the grey part while the mean pc is in black. The trend of the variance is given by the green line. In (e) the percentage increase is calculated. The red line is the increase for just the summer season, while the blue line regards the winter season. In (b) the second correlation pattern associated to the SLP anomalies projected over the second pc of SSH is displayed. The trend in the variance corresponding to the first pattern is described in (d) while the associated percentage increase is in (f). The grey part in (e) and (f) describe the significance test performed. In this case CMIP5 models are taken into consideration. Units of SSH are in cm.

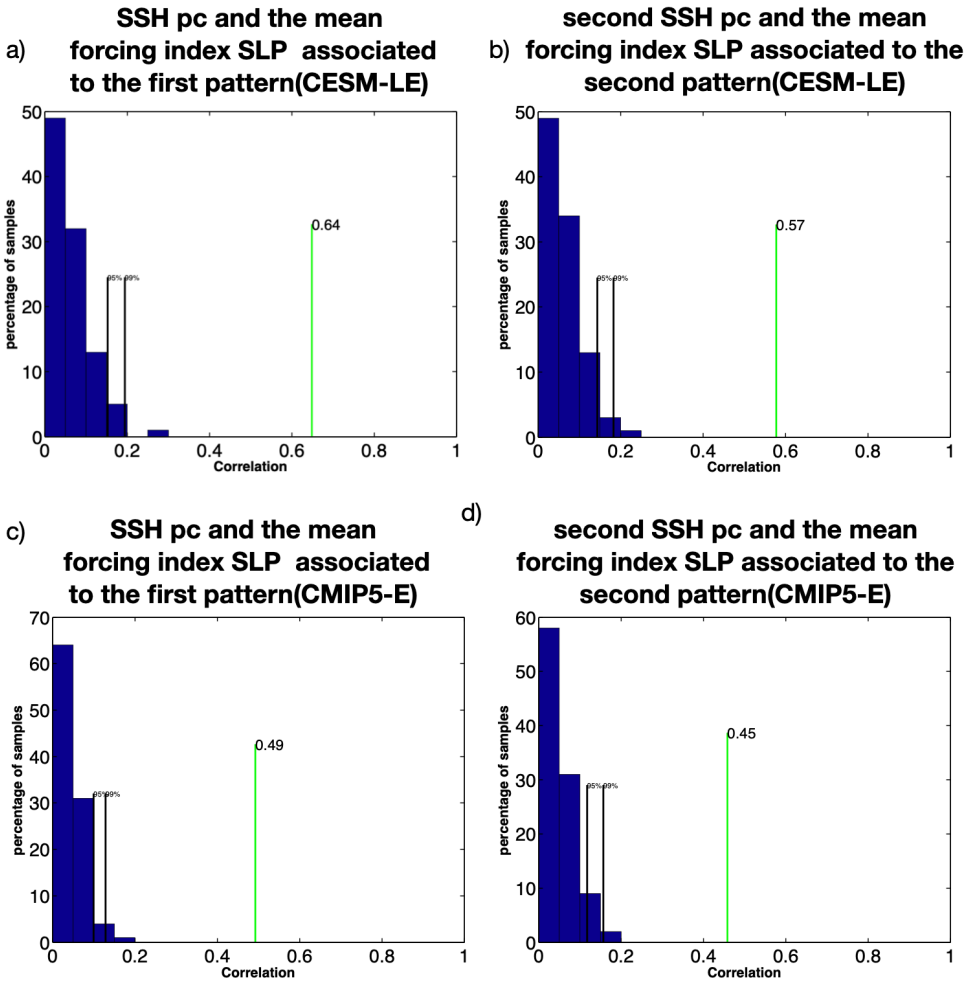

Figure 2.9: in this case we consider the response of the climate system to continous random forcing and its correlation with the first and second pc of SSH. In (a) and (b) the correlation between the SLP forcing index and the SSH ensemble mean first and second pc is displayed. In this case the CESM-LE output has been used. In (c) and (d) the same figures have been done with the CMIP-E models. We obtain a correlation a little higher in the CESM-LE case

CHAPTER 3

PREDICTABILITY AND EMPIRICAL DYNAMICS OF FISHERIES TIME SERIES IN THE NORTH PACIFIC

This chapter is published as "Navarra GG, Di Lorenzo E,Rykaczewski RR and Capotondi A (2022) Predictability and empirical dynamics of fisheries time series in the North Pacific. Front. Mar. Sci. 9:969319. doi: 10.3389/fmars.2022.969319"

3.1 Introduction

The Kuroshio-Oyashio system is composed of the western boundary currents (WBC) of the North Pacific's subtropical and subpolar gyres. In the transition region between the two gyres, quasi-stationary meanders form the Kuroshio-Oyashio Extension jet (KOE). The KOE is flanked to the south by an anticyclonic recirculation gyre which has been observed to increase the eastward transport of the jet [Mizuno et al., 1983; Qiu and Chen, 2005; Qiu et al., 2017]. Atmosphere-ocean interactions are particularly intensified in the WBC. Almost 70% of the latent and sensible heat transferred to the atmosphere from the ocean in the northern hemisphere is transferred in the region between 25°N and 45°N latitude [Kwon et al., 2010]. This heat transfer is crucial in controlling surface baroclinicity and increasing storm activity. As a result, the KOE jet is one of the regions with the greatest eddy kinetic energy in all the North Pacific. [Kelly et al., 2010]

The internal dynamics of the KOE play a critical role in explaining the decadal fluctuations of the Kuroshio-Oyashio system [Mitsudera et al., 2001; Qiu, 2003]. However, it is now well established that the interactions with external modes of variability are important in triggering the quasi-stationary meanders in the KOE jet. Recent study confirms that the surface Chl-a concentration, nutrient concentration, and catches of fish stocks are associated with two dominant modes of variability of the North Pacific [Yati Emi et al.,

2020] which are the Pacific Decadal Oscillation (PDO) [Mantua et al., 1997] and the North Pacific Gyre Oscillation (NPGO) [Di Lorenzo et al., 2008; Yatsu et al., 2013; Lin et al., 2014]. One way in which the PDO-related dynamics influences the marine ecosystems is through the control of seasonal mixed layer processes. For the northwestern Pacific, a positive phase of the PDO is associated with a negative anomaly in the SST with an associated increase in the mixed layer depth, leading to a weakening of the KOE [Yatsu et al., 2013]. The opposite happens in a negative phase. These climate regime shifts are well correlated with fluctuations in biological characteristics [Yati et al., 2020; Möllmann and Diekmann, 2012]. The weakening of the KOE is hypothesized to increase the catches of Japanese sardine in the northwestern Pacific, while during a strengthening of the jet, catches of Japanese anchovies are relatively high [Chavez et al., 2003].

While the patterns of climate variability are well established [Liu and Di Lorenzo, 2018], the mechanism by which the marine ecosystems are influenced by climate fluctuations remains unclear [see review in Bograd et al., 2019]. As climate processes induce fluctuations in marine ecosystems, human societies are often negatively impacted, as food security and coastal economies are dependent on the stability of marine resources [Yunne-Jai et al., 2010; Shin et al., 2010]. This means that improved predictions of future changes in the fisheries of the Kuroshio-Oyashio system can have important socioeconomic impacts.

Forecasting marine ecosystems presents a series of challenges because the interactions of the ecosystem with human society often have been nonlinear and occur over a range of spatial and temporal scales. Also, the lack of long and accurate time series challenges our ability to study climate and fisheries interactions and develop forecasts that are accurate at long lead times. To address these challenges, past studies have focused on identifying the observational needs for ecosystem forecasting [Capotondi et al., 2019] and on exploring the use of dynamical model approaches to account for non-linearities present in marine ecosystems dynamics [Jacox et al., 2019; Tommasi et al., 2017]. Yet, numerical dynamical models still have biases, including erroneous representations of the WBCs and their sepa-

ration latitude, limiting their usefulness for capturing many complex, fine-scale processes. Given that we still do not have adequate dynamical models that capture the dynamics of climate, fish, and human interactions, previous studies [Koul et al., 2021] have investigated the use of simple statistical models (linear regression and multiple linear regression) for fishery forecasting. These studies have offered successful predictions of cod stocks in the Barents Sea on decadal time scales.

In this article we have considered an alternative approach to predict of time series of fisheries indices by using an empirical dynamical model (EDM) method or Linear Inverse Model (LIM). These approaches have proved very useful for understanding the variability of North Pacific physical ecosystems drivers, including extremes [Capotondi et al., 2022], and have exhibited promising results when applied to North and tropical Pacific SST forecasts [Newman, 2007]. Here, we apply the LIM approach to explore the predictability of a set of fisheries time series describing the temporal changes of specific stocks. These time series can be viewed as proxies that simplify complicated biological and socioeconomic conditions over time [Blanchard et al., 2010; Tam et al., 2019]. The three fisheries databases considered in this study are (1) stock biomass anomalies from scientific stock assessments performed for a limited number of stocks in different regions (RAM database, [Ricard et al., 2012]), (2) landings of stocks as reported by the country targeting the species (LME database, [Pauly et al., 2020]), and (3) the catches of species that are estimated from data reported to the United Nations (FAO database [Pauly et al., 1998]).

These data sources are useful in the context of EDMs because they provide a large number of time series that capture physical, ecological and human factors inherent to commercial fisheries statistics. Also, EDMs like the LIM have the added advantage of being able to capture some of the human-forced dynamics that are implicitly reflected in the fish indicators and yet are not explicitly known.

The purpose of the paper is to analyze the ability of the EDM to forecast fisheries time series. While the use of complex dynamical models could be another possible ap-

proach [Park et al., 2019], the inclusion of fisheries information in dynamical models is not straightforward. In addition, dynamical models often suffer from biases in the representation of physical climate features, such as the Western Boundary Currents, and are much more computationally intensive. The EDM approach explored here, if skillful, may provide a useful alternative for forecasting fisheries indices. Here, we consider the forecasting skill related to the fisheries metrics and partition the fisheries predictability between the component associated with climatic variables, i.e., sea surface temperature (SST) and sea surface height (SSH) and that related to stock-stock interactions or socioeconomic factors.

3.2 Methodology

3.2.1 Reanalysis Data

The physical data that we included in the LIM was extracted from the ECMWF Ocean Reanalysis System 4 (ORAS4) on a 1 by 1 latitude–longitude spatial resolution between 1958-2016, for a spatial region of 15°S-62°N, 100°E-290°E, which includes the tropical and North Pacific. It is important to include in the LIM all North and tropical pacific basins for the physical state. This allows us to capture the dynamics of the large-scale climate modes such as PDO and NPGO and their tropical forcing linked to the different flavors of the El Niño Southern Oscillation [Di Lorenzo et al. 2013].

As is often done with the LIM [Newman et al., 2007; Zhao et al. 2021], the SSH and SST data were first coarsened by averaging them into a box of 2 degrees of latitude and 5 degrees of longitude. As a next step, the data were smoothed to remove sub-seasonal variations with a 3 month running mean. The SSH and SST anomalies were computed by removing the mean monthly climatology. Further description and access to the data can be found at https://icdc.cen.uni-hamburg.de/daten/reanalysis-ocean/easy-init-ocean/ecmwf-ocean-reanalysis-system-4-oras4.html

3.2.2 Fishery Data

The first database considered for the fisheries was the RAM Legacy Stock Assessment Database (RAM), www.ramlegacy.org, [Ricard et al. 2012]. Globally, this database contains 331 stock assessments divided into 295 marine fish stocks and 36 invertebrate stocks. The species considered from the RAM database are displayed in Supplemental Table 1 and included 20 species from the northwest Pacific region of interest (Figure 3.1a). For some species, the associated time series have a time duration of 63 years from (1950-2012). However, most of the fish indicators are only available after 1979. For this reason, we selected data after 1979 with less than 5 years of data gaps for developing the LIM. The second database considered was the commercial catches from a database aggregated by Large Marine Ecosystem (LME), https://www.lmehub.net/, [Pauly et al. 2020] (Figure 3.1b). An LME is defined as an area of 200,000 km2 or greater whose extent is determined by similarities in relevant variables such as bathymetry, productivity, or trophic relationships [Sherman et a. 2014]. The database contains 10,438 stocks in all regions of the world with 55 years of data, from 1950 to 2004. Three LMEs were considered in this study (the Kuroshio, the Oyashio Current and the Sea of Japan LMEs), and those included catches for 225 stocks that have data gaps for less than 5 years. The catches were defined as the weight of fish caught in the open sea independently of the way they have been taken (i.e., gear type or as target or non-target catch). We have considered catches data from 1959 to the most recent data. Here, catches in FAO region 61 (Fig. 3.1j) were analyzed (a region of the Northwest Pacific from about 20◦N to 65◦N and from the coast of Vietnam east to the Bering Strait). The discarded fish have not been filtered out in the two databases; the stocks of the LME database are referred as "catches" as the database contains more catches in weight than the FAO database. The last database considered included the landings obtained from the Food and Aquaculture Organization (FAO) of the United Nations (www.fao.org/fishery/en/statistics) [Pauly et al. 1998] (Figure 3.1c). Landings for each region offer insight into variability in commercial fishing operations and the fish populations

that support them. WE have used 171 landings data with data gaps less than 5 years. As for the LME database we have started the data from 1959. The stocks considered for

3.2.3 Detrending and Standardization

Before proceeding in developing the LIM, we detrended the fisheries and physical time series so to increase their stationarity (i.e., no linear trends are present in any record). Specifically, the time series extracted from the fisheries databases were standardized by dividing by the standard deviation for each individual stock ID and detrended by removing the best linear trend fit. Consequently, the time series are represented in STD units, and the total number of fish species is described by the StockID (Figure 3.1a, b, and c). The fish informations relative to the fish stocks are provided in Table 1, 2, and 3 of the supplemental materials. To examine the percentage of variance excluded by the detrending, we calculated the difference in variance between the total original data and the detrended time series. The mean variance explained by the trend is 29.5% for the RAM biomass (Figure 3.1d). In particular, the Red seabream Inland sea of Japan (stockID 18) displays the highest variance associated with the trend. For the LME catches and the FAO landings, the variance excluded by removing the trend is 13.5% and 17.5% respectively, as displayed in Figure 1e and f. The associated sign of the removed trend displays a mixture of positive and negative trends in the stock time series of all three databases (see supplemental Figure S1).

3.2.4 Principal Components and Empirical Orthogonal Functions

To reduce the dimensionality of the detrended and standardized fish indicators, we used a classic principal components (PCs) analysis. To extract the PCs we first compute the covariance matrix of each fish dataset $F_i(s,t)$, where s denotes the stock id, t its time values, and i the dataset label:

$$C(s,s) = F(s,s)F(s,s)^T \tag{3.1}$$

By performing an eigenvalue decomposition of C(s,s),

$$E_i(s,k)\Lambda(k,k)E_i(k,s)^T = C_i(s,s) \tag{3.2}$$

we derive the eigenvector $E_i(s,k)$ for the eigenmodes $k = 1 \ldots K$, where K=7 for RAM, and K=8 for LME and FAO that are associated with the K largest eigenvalues $\lambda(k)$ from the diagonal of the eigenvalue matrix $\Lambda(k,k)$. The choice of K modes retained in each dataset is explained in section 2.5. Physically, these eigenvectors, referred to as the Empirical Orthogonal Functions (EOFs), are the dominant patterns of variance across the stocks and provide an orthogonal basis onto which we can decompose the original fish datasets as:

$$P_i(k,t) = E_i(k,s)^T F_i(s,t) \tag{3.3}$$

where $P_i(k,t)$ are the PCs for each dataset i. Using this approach we reduce the dimensionality of the fish dataset from s (order 100)$\rightarrow$k (order 10). Prior to the computation of the covariance, years with missing data in any given stock were set to zero to void any contribution to the covariance. Given that for any given year there were only few missing data across all the stocks, the impact of setting to zero the missing values has negligible impact the estimation of the EOFs. The first two dominant PCs for each of the fish dataset are reported in Figure 1g and h and are discussed further in the results section 3.1. The EOFs structures for the first two modes are reported in supplemental material Figure S1. By normalizing the eigenvalue $\lambda(k)$ from the EOFs decomposition, we measure the fraction of variance explained by each pair of PC/EOF mode k as $\lambda(k)/\sum\lambda(k)$. The spectrum of explained variance is reported in Figure 3.1i.

3.2.5 LIM model

Inverse modeling can be defined as the extraction of dynamical properties of a physical-biological system from its observed statistics. The LIM model suggests that on inter annual

time scales, a system may be viewed as a linear system driven by Gaussian white noise. The idea is that the climate timescales underpinning the dynamics of our system are longer than the noise. An example of noise are the fast air sea interactions. In this framework the N component state vector of anomalies X evolves accordingly to the linear equation (3.4). In this equation L represents a matrix that describes the feedback among different components of X, while ξ is the stochastic forcing term.

$$\frac{dX}{dt} = LX + \epsilon \tag{3.4}$$

In this equation L represents a matrix that describes the feedback among different components of X, while ϵ is the stochastic forcing term. For the purpose of this study, the components of the state vector X and of the operator L in equation (3.4) are:

$$\frac{dX}{dt} = \frac{d}{dt}\begin{bmatrix} X_{fishery} \\ X_{SST} \\ X_{SSH} \end{bmatrix} = \begin{bmatrix} L_{fishery-fishery} & L_{SST-SSH} & L_{SST-fishery} \\ L_{SSH-SST} & L_{SST-SST} & L_{SSH-fishery} \\ L_{fishery-SST} & L_{fishery-SSH} & L_{SSH-SSH} \end{bmatrix} \begin{bmatrix} X_{fishery} \\ X_{SST} \\ X_{SSH} \end{bmatrix} + \begin{bmatrix} \xi_{fishery} \\ \xi_{SST} \\ \xi_{SSH} \end{bmatrix} \tag{3.5}$$

In this framework, the state vector X is made of three substate vectors representing the fishery, SST, and SSH dataset. Each of these substate vectors is constructed using the PCs to reduce the dimensionality of the problem. For example,

$$X(t)_{SST} = [SST_P C_1(t), SST_P C_2(t), \ldots., SST_P C_K(t)] \tag{3.6}$$

As discussed by Penland et al. [1989], the statistics of a system modeled by the LIM must be Gaussian [Penland et al. 1995]. The operator L can therefore be determined from the state vector X by discretizing the equation (3.4).

$$L = \frac{1}{\tau} ln(< X(t+\tau)X(t) >< X(t)X(t) >) \tag{3.7}$$

After obtaining L , we can forecast of the state vector for a specific lead time τ using:

$$X(t+\tau) = exp(L\tau)X(t) \tag{3.8}$$

An important assumption in the use of the LIM, and the forecast equation (3.8), is that the statistics of the system are stationary over the period considered. For this reason, the operator L must be dissipative, which means its eigenvalues must have negative real parts [Newman et al. 2013]. Similarly, we expect that the statistics of stochastic forcing $Q =< \xi\xi^T >$ [Penland et al. 1995], which are determined from the fluctuations-dissipation relationship,

$$Q = -LC(0) - C(0)L^T \tag{3.9}$$

has positive eigenvalues. In supplemental Figure S2 we have displayed the eigenvalue spectrum for the operator L and the matrix Q. We obtain negative eigenvalues for L and positive for Q indicating that our statistics are stationary.

-LIM forecast configuration

Number of PCs used in the state vector. To implement the LIM forecast model, the number of PCs retained in the physical and biological state vectors were chosen differently. For the physical components of the analysis, we retain 20 PCs for the SST and 17 for the SSH which capture 77% and 76% of the variance, respectively. These numbers were selected following the configuration of a previous Pacific LIM that uses the same data sources and domain area [see Zhao et al. 2021]. Equation 3.5 is used independently for each of the fish datasets. To establish how many PCs to retain for each datasets (e.g. RAM, LME, and FAO), we performed a series of cross-validated forecasts (explained in the next section 2.6) using equation (4) to identity the number of biological PCs to retain in the LIM that would lead to the highest forecast skill for the reconstructed fish indicators. Based on this cross-validation, we retained 8 PCs for the RAM biomass, corresponding to 94% of the variance of that quantity, 7 PCs for the LME landings, which describes 74% of the landings total

variance, and 7 PCs for the FAO catches, which still correspond to 70% of the variance. Also, for the fishery state vectors, we interpolate the data to the same monthly scale of SST and SSH to allow inclusion of physical information at seasonal time scales. Temporal span of forecast. The dataset used in this study have different spatial coverage. The physical data is only available starting 1959. Thus, we begin our training of the LIM and examination of the forecast skill over the following period: 1959-2016 for SSTa, 1979-2012 for RAM, 1959-2004 for LME, and 1959-2014 for FAO.

3.2.6 Cross-validation

To ensure that the LIM is tested on independent data, the estimates of L and of forecasting skills were cross validated by subsampling the data record. We have removed in total 10% of the data, for both the fishery and the physical part, and computed the operator L for the remaining data. The independent years removed are then forecasted using the computed L. This procedure is repeated for the entire period. The associated forecasting skills are computed by the correlation $r(\tau)$ between the observational data and the forecast for the different lead times τ. For example, to evaluate $r(\tau)$ for the each of the fish datasets, the PCs of the forecasted sub-state vector $\hat{X}(\tau)$ obtained from (eq. 4) [Newman et al. 2003] are projected into the truncated EOF space,

$$\hat{F}(s,\tau) = E_i(s,k)^T \hat{P}(k,\tau) \tag{3.10}$$

to obtain the forecasted fishery time series that are then correlated with the original data $F_i(s,\tau)$. We apply this procedure to the LIM that (1) contains only the physical state variables SST and SSH, and (2) contains the physical variables plus the fishery's principal components.

3.2.7 LIM tau test

To test the validity of linear approximation of the LIM, we perform the so called a τ test, which is designed to test the ability of the LIM to reproduce the lag covariance statistics using a lag which goes far beyond the training $\tau = 3$ months. Practically, the test consists of comparing the covariance matrix obtained from the original state vector to the covariance matrix calculated using the LIM for different lags $\tau = 3..12..36$ months. The LIM is re-computed each time using the different training τ. Given that the LIM must be independent of the chosen lag, these two covariance matrices should give a compatible result for the LIM to perform well [Newman et al. 2011; 2017]. A comparison of the diagonal elements of the observed lag covariances with the one obtained from the LIM is show in the supplemental material for the SST (Figure S3), and each of the fishery datasets (Figures S4, S5, and S6). Overall, LIM is able to capture the main structures of the lag autocovariance pattern for both the SST (Fig.1 of supplemental materials) and the fishery indicator (Fig 2-4 of supplemental material) for lags up to =72 months in the fish dataset.Results from this test indicate that the LIM approximation is valid for long-lead forecasts of this set of physical and fishery indicators.

3.2.8 Persistence and Forecast Skill

When evaluating the skill of a forecast it is customary to ask the question of whether the forecast model adds skill beyond the so-called persistence forecast. This is equivalent to forecasting that each future conditions is the same as the condition today. From a mathematical point of view the persistence correlation forecast skill at different lead time for a timeseries y(t) is given by the auto-correlation function

$$ACF(\tau) = \frac{< y(0)y(\tau) >}{< y(0)y(0) >} \tag{3.11}$$

Where $<y(0)y(0)>$ is the covariance at zero lag and $<y(0)y(\tau)>$ is the covariance at

lag τ. In climate science, for a forecast model to have higher skill that persistence is a fundamental measure to indicate that the model is able to extend the predictability through its dynamics beyond the natural temporal auto-correlation that exists in the data. A recent discussion of the concept of persistence can also be found in Jacox et al. [2020]. In the article, we compare the LIM forecast skill to persistence as a way to estimate the LIM's ability to capture the dynamics of the system and to use those dynamics to extend the predictability of the fish indicators. Specifically, we use the following definitions for the correlation skill,

$$r_{persistence}(\tau) = ACF(\tau) \tag{3.12}$$

$$r_{forecast}(\tau) = correlation(\hat{y}(\tau), y(\tau)) \tag{3.13}$$

where $\hat{y}(\tau)$ is the LIM forecasted state at lead and $y(\tau)$ is the observed state. As reported in section 2.6, all the forecasted states use a LIM that is trained with a datasets that does not include the observed state, which we also refer to this as the cross-validated forecast skill. To estimate the statistical significance of the correlation skill we have used a Montecarlo approach. Specifically, we first develop an auto-regressive model of order 1 (AR1) as a null-hypothesis simulation model (i.e., red noise) for a given pair of timeseries that are being compared in the correlation. Next, for each of the timeseries we estimate the lag-1 auto-correlation coefficient and use that to generate 2000 pairs of red noise timeseries using the AR1 model. We compute the probability distribution function (PDF) of correlation coefficients between the red noise timeseries pairs. This PDF is then used to estimate the 95% and 99% confident levels of the correlation between the two original timeseries.

3.3 Results and Discussion

3.3.1 Fisheries biomass data and relation to physical quantities

Given that the data has been decomposed in EOFs and PCs we first perform an inspection of their statistics. The temporal evolution of the first two dominant modes for the fish datasets

are captured by the PC1 and PC2 (Figures 1G, H). Both the PCs1 and PCs2 displays very strong low-frequency variability in each dataset with a significant level of coherency across the datasets. As further discussed in the next sections, these low-frequency variations may be associated not only with decadal climate variability, but also with human influences. For example, these stocks have been heavily exploited in the last 60 years [Pons et al., 2017]. In particular, the increase in fishing pressure coupled with the demography of the fish stocks has led to a collapse and recovery of populations with common trends among stocks as discussed by previous authors [Myers and Worm, 2003; Nye et al., 2009; Wang et al., 2020]. The amount of variance explained by the first two PCs for each fisheries databases (see Methods section 2.4) is very large (Figure 1I). For example, PC1 for the RAM biomass represents 47% of the total variance, while the PC1 of the LME catches and the FAO landings describe respectively 25% and 35% of the variance. This indicates that despite the large number of fish stock indicators, the overall degrees of freedom in the datasets are low and represented by a relatively low number of modes (e.g. pairs of PCs/EOFs). To quantify the extent to which the low-frequency fluctuations of the fish indicators are tracking climate variability, we perform a correlation analysis between the PCs of the fisheries data and large scale SSTa. Correlations between SST anomalies and the PCs1 for the three fish datasets are reported in Figure 2a. While the patterns show some differences it is evident, especially for the LME and FAO, that stronger correlation existing the region of the KOE. This is more evident by computing a map of the mean correlations across the datasets (Figure 2b), which shows a strong negative correlation from the East China Sea and coastal Japan extending in the central North Pacific. A similar correlation analysis for the PCs2 (Figure 2c) reveals the emergence of the more familiar basin-scale pattern of Pacific decadal variability such as the PDO across all the datasets. Again, this PDO-like pattern becomes clearer in the map of the mean correlations for PCs 2 (Figure 2d) exhibiting strong correlations in the canonical center of actions of the PDO over the central and eastern North Pacific. The correlation patterns of the PCs with the SSTa (Figure 3.2)

give us confidence that the link between the climate variability and the fish can be exploited for forecasting, especially in the KOE region, where previous studies have shown longer-lead multi-year predictability (see next section 3.2).

3.3.2 LIM Forecasts of the low-frequency variability of the KOE

It is well known that the KOE variability is strongly linked to wind induced Rossby waves formed in the Central North Pacific [Deser et al., 1999; Schneider and Miller, 2001; Seager et al., 2001]. The effect of the wave propagation can be separated into two dynamical modes of variability. The first mode is related to a latitudinal shift of the KOE jet, while the second is associated with a strengthening or weakening of the KOE quasi-stationary meanders [Taguchi et al., 2007; Taguchi et al., 2014; Ceballos et al., 2009]. These dynamical changes in the KOE jet can impact the local marine populations with changes in the wintertime mixing and springtime stratification that control seasonal nutrients and light supply for primary producers [Chiba et al., 2013; Nakata et al., 2003]. Given that it takes approximately 2-3 years for the Rossby waves to propagate in the KOE region, these large-scale dynamics carry an inherent multi-year predictability that can be exploited for longer lead low-frequency forecasts on physics and marine ecosystems. Thus, before exploring the predictability of the fisheries time series, it is informative to quantify the low-frequency predictability of the KOE physical environment, specifically the SST, which is a state variable with strong links to the dynamics of fish populations. For this purpose, we build a LIM using only SSTa and SSHa data (see Methods section 2.5) and use equation (3.8) to perform a series of cross-validated forecasts for lead times of 6, 12, and 24 months (Figure 3.3a, b, and c). We find that areas of higher skill are concentrated along the Northeast Pacific coast and the KOE extension and are co-located with centers of actions of the PDO and the KOE low-frequency variability patterns [Matsumura et al. 2016]. We also examine the forecast skill in the KOE region (the average SSTa in the black box of Figure 3.3a) as a function of the month used to initialize the forecast (Figure 3.4a). We find that significant forecast

skill (correlation ¿0.6) extends only up to 1.5 years. If we compare this skill level with that obtained from persistence (Figure 3.4b), we find that the LIM extends this skill beyond persistence up to 10 months (Figure 3.4c). Given that the fisheries are predominantly characterized by low-frequency variability, we now quantify the low-frequency predictability of the SSTa in the KOE by applying a 6-year filter to the forecasted state vector. As expected when applying a lowpass filter, we find an overall increase in skill spatially at 6, 12, and 24 months (Figure 3.3d, e, and c). If we examine the skill as a function of initialization month (Figure 3.4d), we find that high skill levels (R¿0.6) extend up to lead times of 4-5 years. However, the filtering also leads to longer persistence skills due to the increase in autocorrelation, up to 1.5 years (Figure 3.4e). Nevertheless, if we look at the difference in skill between the LIM forecast and persistence (Figure 3.4f), we find that the filtering does extend dynamically the low-frequency predictability by 4-5 years. As emphasized by previous articles [Thompson et al. 2010], the increased skill shows the importance of the low frequency variability of SST anomalies in the KOE jet. These results confirm previous findings that in the KOE, the large-scale climate associated with the propagation of Rossby waves and the modes of decadal variability lead to extended multi-year predictability.

3.3.3 LIM forecast of Fisheries Time Series

We now analyze if the long-lead, low-frequency predictability of the KOE physical state is important in extending the forecast of fisheries metrics. We construct three independent forecast LIMs for each of the fish datasets (i.e., RAM, LME, FAO) using the definition of the state vector in equation (2) (see Methods section 2.5). The results from the cross-validated forecast are shown in Figures 3.5a, b, and c for leads up to 160 months. Results show high correlation skill values R 0.7 extending almost to the end of the forecast window. Given that stocks are characterized by time series with exceptional low-frequency variability, it is critically important to assess If the correlation skill of the LIM is significant. Using the Montecarlo approach discussed in Method section 2.8, we identify the

95% and 99% significance levels for each of the datasets. These are marked in the colorbar of Figure 3.5 and show that any correlation above R=0.55 (RAM), R=0.41 ((LME), and R=0.44 (FAO) is significant at 95%. Correlations above R=0.66 (RAM), R=0.51 (LME), and R=0.54 (FAO) are significant at the 99% with the RAM being higher than the other datasets because of its shortened temporal span, which reduced the degrees of freedom. We further examine the impact of autocorrelation in the data on the forecast still by computing the persistent forecasts (Figure 5d, e, and f). We find significant persistence skill R 0.7 up to 4 years for some of the RAM biomass anomalies (Figure 3.5d) and up to 3 years for the LME (Figure 5e) catches and FAO landings (Figure 3.5f). Despite the long-lead forecast skill from persistence, the difference maps between the LIM forecast and persistence skill (Figure 3.5g, h, and i) show that the LIM has higher and extended significant forecast skill beyond the range of persistence by 3-5 year limit. Despite the statistical measures of skill significance discussed above, it is important to recognize that ultimately the real usefulness of these forecasts will depend on how, and what aspects of, this information enables better-informed decisions by fishery managers. For this purpose, it is informative to show the time series of the LIM forecasts for a few selected species. In each database we picked two species that show extended predictability and displayed their 2- and 5-years composite forecast time series (Figure 3.6, red lines are the cross-validated forecasts, blue line the original data). Focusing on the RAM, Figure 6a and b displays the stock Striped Marlin North Pacific and Yellow sea bream Sea of Japan from the RAM database. Despite the overall higher frequency variability of the LIM forecast, overall the 2-year LIM well captures the low-frequency evolution of the time series including some of the interannual extrema on timescale between 2-5 years. In contrast, for longer lead forecasts such as the 5-year (Figure 6c and d), the LIM is only able to capture the low-frequency variations (6 year and above) and loses information about the interannual fluctuations (e.g. compare Figure 6b vs. d). A similar behavior is somewhat evident also in the LME catches stocks Sardinops sagax and Reinhardtius evermanni (Figure 6e-h) and the FAO landings stocks

Sciaenidae and Colorabis saira (Figure 3.6i-l). We examine this behavior more systematically across the stocks – that is the LIM loses its ability to forecast interannual fluctuations for longer forecast leads, by applying a 6-year highpass filter on the composite forecasted time series for leads times between 0-160 months and re-examining the correlation skill with the original data. We find that the LIM interannual forecast skill is significantly less for longer lead times (Supplemental Figure S7a, b, c) as evidenced by taking the difference with the non-filtered forecast (Figure S7d, e, and f).

3.3.4 LIM forecasting skills Sensitivity analysis

To better understand how marine ecosystem components and physical components (and their interaction) contribute to the forecast skill, we perform a sensitivity analysis to investigate key physical and biological factors that influence the predictability of the fisheries. More precisely, the purpose of the sensitivity analysis is to quantify how the forecasting skill of individual fisheries time series depends on knowledge of the climate state and to the knowledge of the other fish stocks. We begin by exploring the role of the physical state variables in the predictability of the fisheries time series by including the constraint that the interaction terms of the fisheries with SSTa and SSHa in the operator L are zero. This condition implies that we are excluding the interaction of the SSTa and SSHa PCs with the fishery PCs. The forecast skill of the LIM that does not include the coupling with the physics is shown in Figure 3.7a, b, and c for the different fish datasets. It is immediately apparent that the skill is greatly reduced compared to the full LIM (Figure 3.7d, e, and f, show the difference map) suggesting that the information of the physical climate variability plays a primary role in extending the LIM forecast skill of the fishery indicators. Specifically, we find that a LIM forecast that depends only on the knowledge of the stock vs. stock interactions (e.g. without the physical information) has limited extended predictability to up to 50 months across the RAM, LME, and FAO timeseries. This reduction in skill can be attributed to several factors, which are not fully investigated in this study. One possible

reason regards the role of the Rossby wave propagation in the multiannual prediction of ecological systems [Jacox et al., 2020]. These waves are predominantly initiated in the eastern side of the North Pacific Ocean through modulation of Ekman pumping connected with wind stress curl anomalies induced by the PDO mode [Capotondi and Alexander, 2001; Qiu et al., 2017]. Propagating Rossby waves (RWs) have an important impact on nutrients availability on interannual timescales, which are linked to changes in primary [Sakamoto et al., 2004] and secondary producers as well. In particular, it has been found that RWs modulate the depth of the nutricline by a few tens of meters [Killworth et al., 2004] with corresponding impact on surface nutrient availability. In addition, RW impact surface chlorophyll concentration by a vertical displacement of the chlorophyll maximum, [Dandonneau et al., 2003]. Consequently, it is possible that the exclusion of the physical interactions that are associated with skillful physical predictions from the LIM lead to a much lower forecasting skill for most of the stocks. Next, we want to examine how the forecast skill depends on the interactions among species. To this end, the full case LIM forecast is repeated by replacing the principal components of the North Pacific stocks with the data time series for every single stock rather than all stocks together (Figure 3.7g, h, and i). For each of the three databases, the RAM biomass, the FAO landings, and the LME catches, we find again a substantial reduction in forecast skill when data from other stocks are excluded from the LIM (Figure 3.7k, l, and m, show the difference map). This suggests that interactions between stocks contain information that is useful for the predictability. Through these sensitivity analyses, we conclude that the climate forcing has a considerable impact on the fisheries forecast, but it does not represent the only contribution to the skill. To a lesser extent, skill is contributed from the fisheries data from other stocks in the region.

3.4 Conclusions

Previous studies [Yati et al. 2002, Brander et al. 2007] have documented how climate variability and change have a significant impact on marine populations and fish species in

the North Pacific. However, the mechanisms linking climate fluctuations to the dynamics of marine ecosystems are not fully understood and are currently not well captured by numerical models. Long-term time series of data for both climate and fisheries such as population biomass (RAM), catches (LME), and landings (FAO) provide an opportunity to explore the coupled climate-fish predictability using empirical dynamical models and machine learning approaches. These approaches are very promising because the time series of fish indicators also reflect non-climate forcing that are related to the internal stock dynamics, human exploitation by commercial fishing, economic conditions, and technological advancements. These combined interactions are hard to resolve in traditional dynamical models. Each of these non-climate processes and their interactions can have a substantial influence on metrics of fisheries biomass, landings, and catches. However, the relative importance of these factors on the variability of fish species and their predictability has not been fully explored. In this paper, we used observationally derived lag covariance statistics to empirically capture the linear and (fast) nonlinear interactions among fish stocks, and of fish stocks with human and climate drivers (e.g. the LIM forecast model). Our results showed that the empirical dynamical forecast of the climate-fish-human multi-variate LIM has long-lead predictability that extends beyond the persistence timescale for up to 5 years with significant skill. This finding is consistent with recent studies showing how both short-lived and long-lived species display a response to climate variability and to the increased fishing pressure [Pinsky ML et al. 2015; Rouyer et al. 2014; Wang et al. 2020]. To further confirm and separate the impacts that climate and non-climate drivers are having on the fisheries, we have implemented a series of sensitivity analyses that selectively included or excluded the interaction terms between climate and fisheries time series in the LIM dynamical operator. Results of the analysis revealed a significant decrease in fish forecast skills when the interaction with the SSH and SST is excluded. While the LIM methodology does not allow us to explicitly diagnose which mechanisms of physical-biological coupling are important for extending the predictability in the KOE region, it does confirm and quantify

the critical role of ocean climate dynamics, which previous studies had discussed but not explored with rigorous quantitative measures [see also review from Jacox et al. 2020]. In fact, this study is to our knowledge one of the first attempts to explore empirical model forecasting in the KOE region. Further analyses also revealed that the forecast skill arising from empirical relationships among the stocks is also important, although less important than the inclusion of physical characteristics. This indicates that the information shared among stocks, which could be reflective of changes in industrial fishing practices, market forces, or species interactions, substantially improves forecasting skills. In particular, we notice a distinction in the RAM data between short-lived species and long-lived species as we compare the results with the first sensitivity analysis. Short-living species are highly dependent on climate factors and much less on stock-stock interactions. While long-living species have a dependency on climate factors of the North Pacific, but the stock-stock interactions give a high contribution as well to the forecasting skill much more than short-living species. Although more studies are required to understand the joint predictability dynamics between climate and fisheries In the Pacific Ocean, the analyses presented here with a multivariate linear inverse model provide a promising approach for utilizing climate information to predict socio-ecological indicators such as fish catch, biomass, and landings. Our results also suggest that this approach may be successful in accounting for the dynamics of external human forcing (e.g., in this case, fishing) that are implicitly incorporated in the stock-stock interaction terms. Lastly, these findings support the idea that predicting the marine ecosystem as a hole (e.g., including multi-variate ecological indicators) is more skillful than focusing on individual stock time series.

3.5 References

Blanchard J. L., Coll M., Trenkel V. M., Vergnon Rémi, Yemane D., Jouffre D., et al. (2010). Trend analysis of indicators: a comparison of recent changes in the status of marine ecosystems around the world. ICES J. Mar. Sci. 67, Issue 4, 732–744. doi:

10.1093/icesjms/fsp282

Bograd SJ, Kang S, Di Lorenzo E, Horii T, Katugin ON, King JR, Lobanov VB, Makino M, Na G, Perry RI, Qiao F, Rykaczewski RR, Saito H, Therriault TW, Yoo S and Batchelder H (2019) Developing a Social–Ecological–Environmental System Framework to Address Climate Change Impacts in the North Pacific. Front. Mar. Sci. 6:333. $doi : 10.3389/fmars.2019.00333$

Brander, K M. Global fish production and climate change. United States: N. p., 2007. Web. $doi : 10.1073/pnas.0702059104$.

A. Capotondi, et al. Observational needs supporting marine ecosystem modeling and forecasting: Insights from U.S. Coastal Applications Front. Mar. Sci. (2019), 10.3389/fmars.2019.00623

Capotondi, A., Alexander, M. A. (2001). Rossby Waves in the Tropical North Pacific and Their Role in Decadal Thermocline Variability, Journal of Physical Oceanography, 31(12), 3496-3515. Retrieved Jun 4, 2022, from https://journals.ametsoc.org/view/journals/phoc/31/12/1520-0485_2002_031_3496_rwittn_2.0.co_2.xml

Capotondi, A., Newman, M., Xu, T., Di Lorenzo, E. (2022). An optimal precursor of Northeast Pacific marine heatwaves and Central Pacific El Niño events. Geophysical Research Letters, 49, e2021GL097350. https://doi.org/10.1029/2021GL097350

Cornillon P (2007). Fronts in the World Ocean's Large Marine Ecosystems. 21

Chavez, F.P. and Ryan, John & Lluch-Cota, Salvador and Niquen, M.. (2003). From anchovies to sardines and back: Multidecadal change in the Pacific Ocean. Science. 299.

217-221.

Chiba, S., Di Lorenzo, E., Davis, A., Keister, J. E., Taguchi, B., Sasai, Y., and Sugisaki, H. (2013), Large-scale climate control of zooplankton transport and biogeography in the Kuroshio-Oyashio Extension region, Geophys. Res. Lett., 40, 5182– 5187, doi : $10.1002/grl.50999$.

Ceballos, L. I., Di Lorenzo, E., Hoyos, C. D., Schneider, N., & Taguchi, B. (2009). North Pacific Gyre Oscillation Synchronizes Climate Fluctuations in the Eastern and Western Boundary Systems, Journal of Climate, 22(19), 5163-5174. Retrieved Jan 11, 2022, from https://journals.ametsoc.org/view/journals/clim/22/19/2009jcli2848.1.xml

Dandonneau Y, Vega A, Loisel H, du Penhoat Y, Menkes C. Oceanic Rossby waves acting as a "hay rake" for ecosystem floating by-products. Science. 2003 Nov 28;302(5650):1548-51. doi : $10.1126/science.1090729$. PMID: 14645844.

Deser, Clara & Alexander, Michael & Timlin, Michael. (1999). Evidence for a Wind-Driven Intensification of the Kuroshio Current Extension from the 1970s to the 1980s. Journal of Climate - J CLIMATE. 12. 1697-1706. 10.1175/1520-0442(1999)012¡1697:EFAWDI¿2.0.CO;2.

Di Lorenzo, E., et al. (2008), North Pacific Gyre Oscillation links ocean climate and ecosystem change, Geophys. Res. Lett., 35, L08607, doi : $10.1029/2007GL032838$.

Di Lorenzo, Emanuele & Ohman, Mark. (2013). A double-integration hypothesis to explain ocean ecosystem response to climate forcing. Proceedings of the National Academy of Sciences of the United States of America. 110. 10.1073/pnas.1218022110

Jacox, Michael & Alexander, Michael & Siedlecki, S. & Chen, Ke & Kwon, Young-Oh & Brodie, Stephanie & Ortiz, Ivonne & Tommasi, Desiree & Widlansky, Matthew & Barrie, Daniel & Capotondi, Antonietta & Cheng, Wei & Di Lorenzo, Emanuele & Edwards, Chris & Fiechter, Jerome & Fratantoni, Paula & Hazen, Elliott & Hermann, Albert & Kumar, Arun & Rykaczewski, Ryan. (2020). Seasonal-to-interannual prediction of U.S. coastal marine ecosystems: Forecast methods, mechanisms of predictability, and priority developments. Progress in Oceanography. 183. 102307. 10.1016/j.pocean.2020.102307.

Kelly, K. A., Small, R. J., Samelson, R. M., Qiu, B., Joyce, T. M., Kwon, Y., Cronin, M. F. (2010). Western Boundary Currents and Frontal Air–Sea Interaction: Gulf Stream and Kuroshio Extension, Journal of Climate, 23(21), 5644-5667. Retrieved May 15, 2021, from https://journals.ametsoc.org/view/journals/clim/23/21/2010jcli3346.1.xml

Killworth, P. D., Cipollini, P., Uz, B. M., and Blundell, J. R. (2004), Physical and biological mechanisms for planetary waves observed in satellite-derived chlorophyll, J. Geophys. Res., 109, C07002, $doi : 10.1029/2003JC001768$.

Koul, V., Sguotti, C., Årthun, M. et al. Skilful prediction of cod stocks in the North and Barents Sea a decade in advance. Commun Earth Environ 2, 140 (2021). https://doi.org/10.1038/s43247-021-00207-6

Kwon, Y. O., et al. (2010). "Role of the Gulf Stream and Kuroshio-Oyashio Systems in Large-Scale Atmosphere-Ocean Interaction: A Review." Journal of Climate 23(12): 3249-3281.

P., Lin, Chai, F., Xue, H., and Xiu, P. (2014), Modulation of decadal oscillation on surface chlorophyll in the Kuroshio Extension, J. Geophys. Res. Oceans, 119, 187– 199, $doi : 10.1002/2013JC009359$

Liu, Z., Di Lorenzo, E. Mechanisms and Predictability of Pacific Decadal Variability. Curr Clim Change Rep 4, 128–144 (2018). https://doi.org/10.1007/s40641-018-0090-5

Mantua, N. J., Hare, S. R., Zhang, Y., Wallace, J. M., and Francis, R. C. (1997). A Pacific interdecadal climate oscillation with impacts on salmon production. Bull. Am. Meteorol. Soc. 78, 1069–1079. $doi : 10.1175/1520 - 0477(1997)078 < 1069 : apicow > 2.0.co; 2$

Matsumura, S., Horinouchi, T. Pacific Ocean decadal forcing of long-term changes in the western Pacific subtropical high. Sci Rep 6, 37765 (2016). https://doi.org/10.1038/srep37765

Mitsudera, H., Waseda, T., Yoshikawa, Y. & Taguchi, B. Anticyclonic eddies and Kuroshio meander formation. Geophys. Res. Lett. 28, 2025–2028 (2001).

Mizuno, K., & White, W. B. (1983). Annual and Interannual Variability in the Kuroshio Current System, Journal of Physical Oceanography, 13(10), 1847-1867. Retrieved Jun 8, 2022, from https://journals.ametsoc.org/view/journals/phoc/13/10/1520-0485_1983_013_1847_aaivit_2_0_co_2.xml

Möllmann, C., and Diekmann, R. (2012). Marine ecosystem regime shifts induced by climate and overfishing. Adv. Ecol. Res. Glob. Change Multispecies Syst. 47, 303–347. $doi : 10.1016/b978 - 0 - 12 - 398315 - 2.00004 - 1$

Myers, R., Worm, B. Rapid worldwide depletion of predatory fish communities. Nature 423, 280–283 (2003). https://doi.org/10.1038/nature01610

Nakata, K. and Hidaka, K. (2003), Decadal-scale variability in the Kuroshio marine ecosystem in winter. Fisheries Oceanography, 12: 234-244. https://doi.org/10.1046/j.1365-2419.2003.00249.x .

Newman, M. (2013). An Empirical Benchmark for Decadal Forecasts of Global Surface Temperature Anomalies, Journal of Climate, 26(14), 5260-5269. Retrieved May 11, 2021, from https://journals.ametsoc.org/view/journals/clim/26/14/jcli-d-12-00590.1.xml

Newman, M., and P. D. Sardeshmukh (2017), Are we near the predictability limit of tropical Indo-Pacific sea surface temperatures?, Geophys. Res. Lett., 44, 8520–8529, doi:10.1002/2017GL074088.

Newman, Matthew & Alexander, Michael & Scott, James. (2011). An empirical model of tropical ocean dynamics. Climate Dynamics. 37. 1823-1841. 10.1007/s00382-011-1034-0.

Newman, M. (2007). Interannual to Decadal Predictability of Tropical and North Pacific Sea Surface Temperatures, Journal of Climate, 20(11), 2333-2356. Retrieved Feb 20, 2022, from https://journals.ametsoc.org/view/journals/clim/20/11/jcli4165.1.xml

Newman, M., Sardeshmukh, P. D., Winkler, C. R., & Whitaker, J. S. (2003). A Study of Subseasonal Predictability, Monthly Weather Review, 131(8), 1715-1732. Retrieved May

26, 2021, from https://journals.ametsoc.org/view/journals/mwre/131/8/_2558.1.xml

Nye JA, Link JS, Hare JA, Overholtz WJ (2009) Changing spatial distribution of fish stocks in relation to climate and population size on the Northeast United States continental shelf. Mar Ecol Prog Ser 393:111-129. https://doi.org/10.3354/meps08220

Pauly, D., Christensen, V., Dalsgaard, J., Froese, R., and Torres, F. Jr. (1998). Fishing down marine food webs. Science 279, 860–863. doi: 10.1126/science.279.5352.860

Pauly D, Zeller D, and Palomares M.L.D. (Editors) (2020) Sea Around Us Concepts, Design and Data (www.seaaroundus.org)

Park JY, Stock CA, Dunne JP, Yang X, Rosati A. Seasonal to multiannual marine ecosystem prediction with a global Earth system model. Science. 2019 Jul 19;365(6450):284-288. doi: 10.1126/science.aav6634. PMID: 31320541.

Penland, C., Sardeshmukh, P. D. (1995). The Optimal Growth of Tropical Sea Surface Temperature Anomalies, Journal of Climate, 8(8), 1999-2024. Retrieved Jun 4, 2022, from https://journals.ametsoc.org/view/journals/clim/8/8/1520-0442_1995_008_1999_togots_2_0_co_2.xml

Penland, C. (1989). Random Forcing and Forecasting Using Principal Oscillation Pattern Analysis, Monthly Weather Review, 117(10), 2165-2185. Retrieved Jun 4, 2022, from https://journals.ametsoc.org/view/journals/mwre/117/10/1520-0493_1989_117_2165_rfafup_2_0_co_2.xml

Pinsky ML, Byler D. Fishing, fast growth and climate variability increase the risk of collapse. Proc B. 2015;282:20151053. doi: 10.1098/rspb.2015.1053

Pons, M., Branch, T.A., Melnychuk, M.C., Jensen, O.P., Brodziak, J., Fromentin, J.M., Harley, S.J., Haynie, A.C., Kell, L.T., Maunder, M.N., Parma, A.M., Restrepo, V.R., Sharma, R., Ahrens, R. and Hilborn, R. (2017), Effects of biological, economic and management factors on tuna and billfish stock status. Fish Fish, 18: 1-21. https://doi.org/10.1111/faf.12163

Qiu, B., Chen, S., & Schneider, N. (2017). Dynamical links between the decadal variability of the Oyashio and Kuroshio extensions. Journal of Climate, 30(23), 9591–9605. https://doi.org/10.1175/JCLI-D-17-0397.1

Qiu, B., & Chen, S. (2005). Variability of the Kuroshio Extension Jet, Recirculation Gyre, and Mesoscale Eddies on Decadal Time Scales, Journal of Physical Oceanography, 35(11), 2090-2103. Retrieved Apr 30, 2021, from https://journals.ametsoc.org/view/journals/phoc/35/11/jpo2807.1.xml

Qiu, B. (2003). Kuroshio Extension Variability and Forcing of the Pacific Decadal Oscillations: Responses and Potential Feedback, Journal of Physical Oceanography, 33(12), 2465-2482. Retrieved Nov 6, 2021, from https://journals.ametsoc.org/view/journals/phoc/33/12/2459.1.xml

Ricard, D., Minto, C., Jensen, O.P. and Baum, J.K. (2012), Examining the knowledge base and status of commercially exploited marine species with the RAM Legacy Stock Assessment Database. Fish Fish, 13: 380-398. https://doi.org/10.1111/j.1467-2979.2011.00435.x

Rouyer T., Fromentin J.-M., Hidalgo M., Stenseth N. C. (2014). Combined effects of exploitation and temperature on fish stocks in the northeast Atlantic. ICES J. Mar. Sci. 71, 1554–1562. doi: 10.1093/icesjms/fsu042

Sakamoto, C. M., Karl, D. M., Jannasch, H. W., Bidigare, R. R., Letelier, R. M., Walz, P. M., Ryan, J. P., Polito, P. S., and Johnson, K. S. (2004), Influence of Rossby waves on nutrient dynamics and the plankton community structure in the North Pacific subtropical gyre, J. Geophys. Res., 109, C05032, doi:10.1029/2003JC001976.

Schneider, N., & Miller, A. J. (2001). Predicting Western North Pacific Ocean Climate, Journal of Climate, 14(20), 3997-4002. Retrieved Jun 4, 2022, from https://journals.ametsoc.org/view/journals/clim/14/20/1520-0442_2001_014_3997_pwnpoc_2.0.co_2.xml

Seager, R., Y. Kushnir, N. H. Naik, , M. A. Cane, , and J. Miller, 2001: Wind-driven shifts in the latitude of the Kuroshio–Oyashio Extension and generation of SST anomalies on decadal timescales. J. Climate, 14, 4249–4265.

Sherman, K. (2014). Adaptive management institutions at the regional level: the case of large marine ecosystems. Ocean Coast. Manag. 90, 38–49. doi: 10.1016/j.ocecoaman.2013.06.008

Shin, Y-J., Shannon, L. J., Bundy, A., Coll, M., Aydin, K., Bez, N., Blanchard, J. L., Borges, M. F., Diallo, I., Diaz, E., Heymans, J. J., Hill, L., Johannesen, E., Jouffre, D., Kifani, S., Labrosse, P., Link, J. S., Mackinson, S., Masski, H., Möllmann, C., Neira, S., Ojaveer, H., ould Mohammed Abdallahi, K., Perry, I., Thiao, D., Yemane, D., and Cury, P. M. 2010. Using indicators for evaluating, comparing, and communicating the ecological

status of exploited marine ecosystems. 2. Setting the scene. – ICES Journal of Marine Science, 67: 692–716.

Taguchi, B., & Schneider, N. (2014). Origin of Decadal-Scale, Eastward-Propagating Heat Content Anomalies in the North Pacific, Journal of Climate, 27(20), 7568-7586. Retrieved Nov 8, 2021, from https://journals.ametsoc.org/view/journals/clim/27/20/jcli-d-13-00102.1.xml

Taguchi, B., Xie, S., Mitsudera, H., & Kubokawa, A. (2005). Response of the Kuroshio Extension to Rossby Waves Associated with the 1970s Climate Regime Shift in a High-Resolution Ocean Model, Journal of Climate, 18(15), 2979-2995. Retrieved Mar 21, 2022, from https://journals.ametsoc.org/view/journals/clim/18/15/jcli3449.1.xml

Taguchi, B., S.-P. Xie, N. Schneider, M. Nonaka, H. Sasaki, and Y. Sasai, 2007: Decadal variability of the Kuroshio Extension: Observations and an eddy-resolving model hindcast. J. Climate, 20, 2357–2377, doi:10.1175/JCLI4142.1.

Tam, Jamie & Fay, Gavin & Link, Jason. (2019). Better Together: The Uses of Ecological and Socio-Economic Indicators With End-to-End Models in Marine Ecosystem Based Management. Frontiers in Marine Science. 6. 560. 10.3389/fmars.2019.00560.

Thompson, L. A., & Kwon, Y. (2010). An Enhancement of Low-Frequency Variability in the Kuroshio–Oyashio Extension in CCSM3 owing to Ocean Model Biases, Journal of Climate, 23(23), 6221-6233. Retrieved Jan 14, 2022, from https://journals.ametsoc.org/view/journals/clim/23/23/2010jcli3402.1.xml

Tommasi Desiree, Stock Charles A., Alexander Michael A., Yang Xiaosong, Rosati Anthony, Vecchi Gabriel A. (2017). Multi-Annual Climate Predictions for Fisheries: An Assessment of Skill of Sea Surface Temperature Forecasts for Large Marine Ecosystems, Frontiers in Marine Science, Volume=4, 2296-7745, https://www.frontiersin.org/article/10.3389/fmars.2017.00201

Wang, JY., Kuo, TC. & Hsieh, Ch. Causal effects of population dynamics and environmental changes on spatial variability of marine fishes. Nat Commun 11, 2635 (2020). https://doi.org/10.1038/s41467-020-16456-6

Yati E, Minobe S, Mantua N, Ito S and Di Lorenzo E (2020) Marine Ecosystem Variations Over the North Pacific and Their Linkage to Large-Scale Climate Variability and Change. Front. Mar. Sci. 7:578165. doi: 10.3389/fmars.2020.578165

Yatsu, A. Review of population dynamics and management of small pelagic fishes around the Japanese Archipelago. Fish Sci 85, 611–639 (2019). https://doi.org/10.1007/s12562-019-01305-3

Yunne-Jai Shin, Lynne J. Shannon, Using indicators for evaluating, comparing, and communicating the ecological status of exploited marine ecosystems. 1. The IndiSeas project, ICES Journal of Marine Science, Volume 67, Issue 4, May 2010, Pages 686–691, https://doi.org/10.1093/icesjms/fsp273

Zhao, Y. Y., M. Newman, A. Capotondi, E. Di Lorenzo and D. X. Sun, 2021: Removing the Effects of Tropical Dynamics from North Pacific Climate Variability. Journal of Climate, 34(23) 9249-9265, doi:10.1175/jcli-d-21-0344.1.

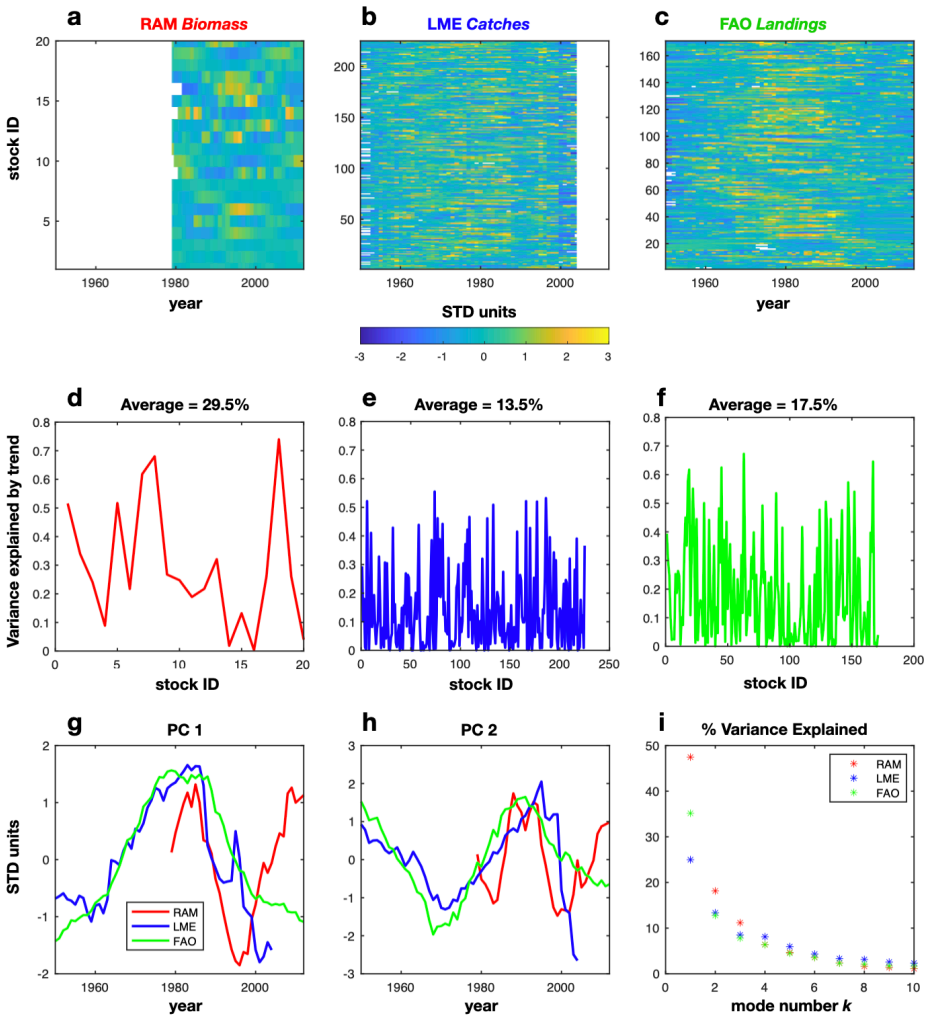

Figure 3.1: Timeseries of detrended and normalized fish stocks for the RAM (a), LME (b), and FAO (c) datasets. The variance explained by the removed trend is represented in (d), (e),and (f). The mean variance excluded by the detrending has been inserted in the plots. The associated variability is described by the first and second principal component (g) and (h), while the corresponding EOFs are displayed in supplementary Figure S1. The percentage of variance explained by the PCs in each dataset is shown in (i).

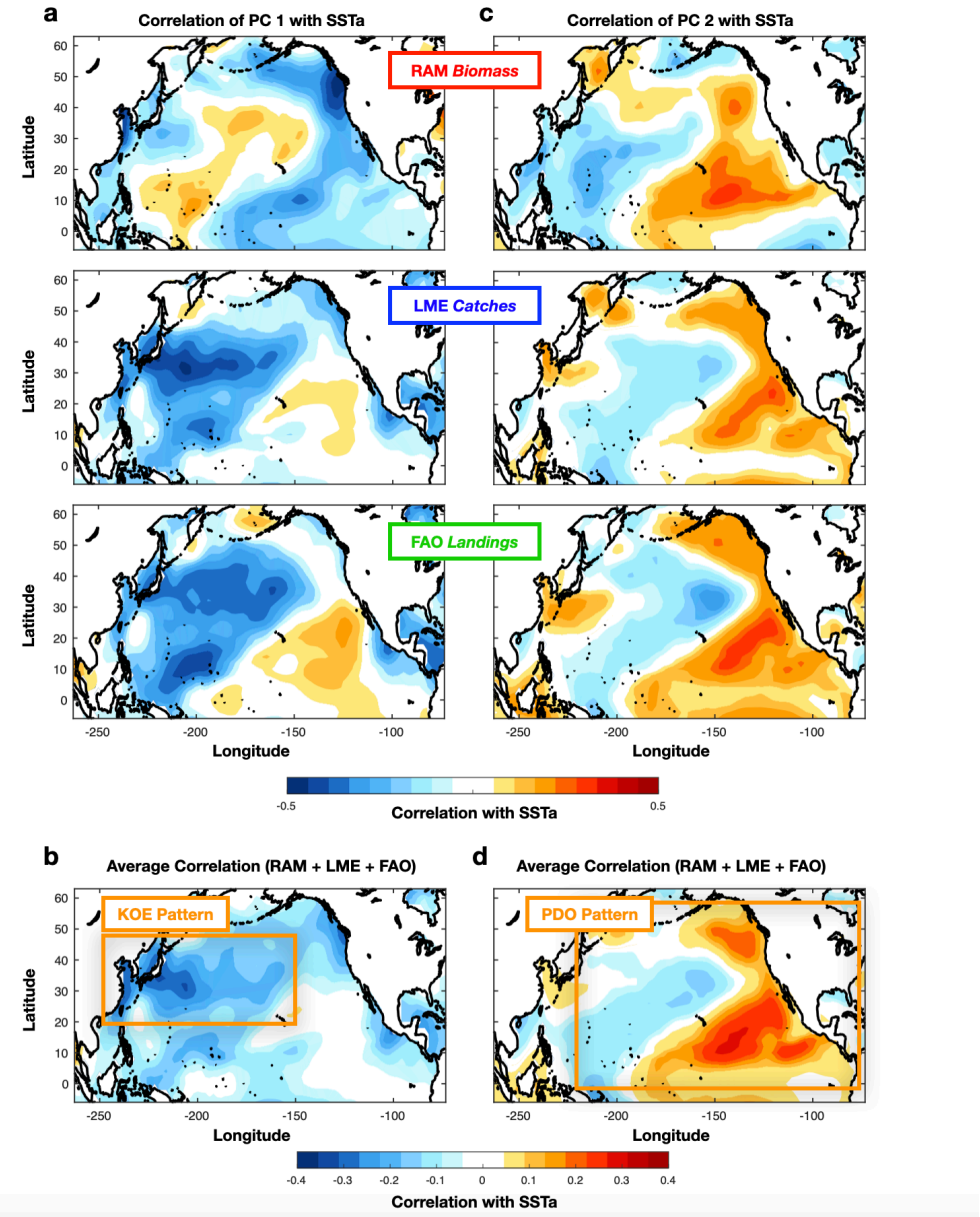

Figure 3.2: Correlation map between SST anomalies and PC1 (a) and PC2 (c) of the fishery datasets (RAM, LME, FAO). The average correlation maps across the datasets for PC1 and PC2 are shown in (b) and (d).

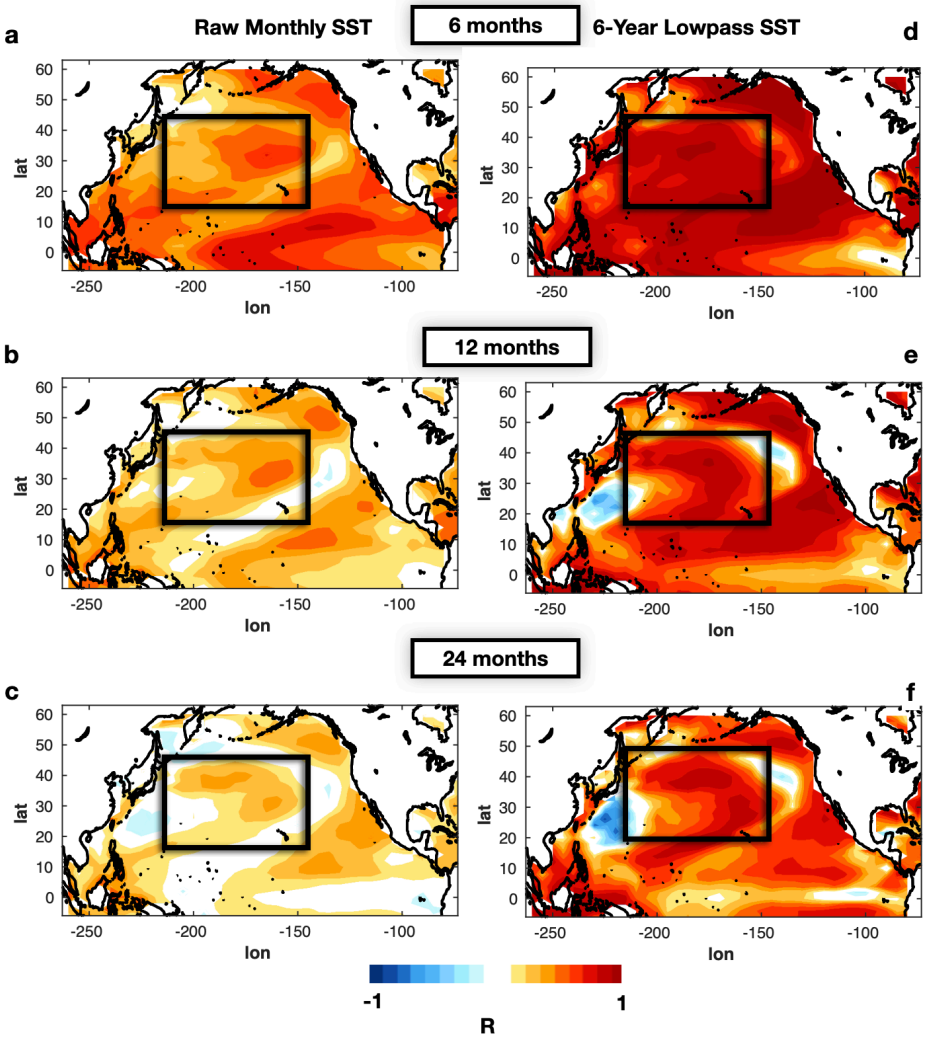

Figure 3.3: Forecast correlation skill of the LIM with physics only (SSTa, SSHa) for lead-times of 6 months (a), 12 months (b), and 24 months (c). In (d), (e), and (f) the same correlation skill maps are shown but computed using the 6-year low-pass filter applied on the original and forecasted monthly data

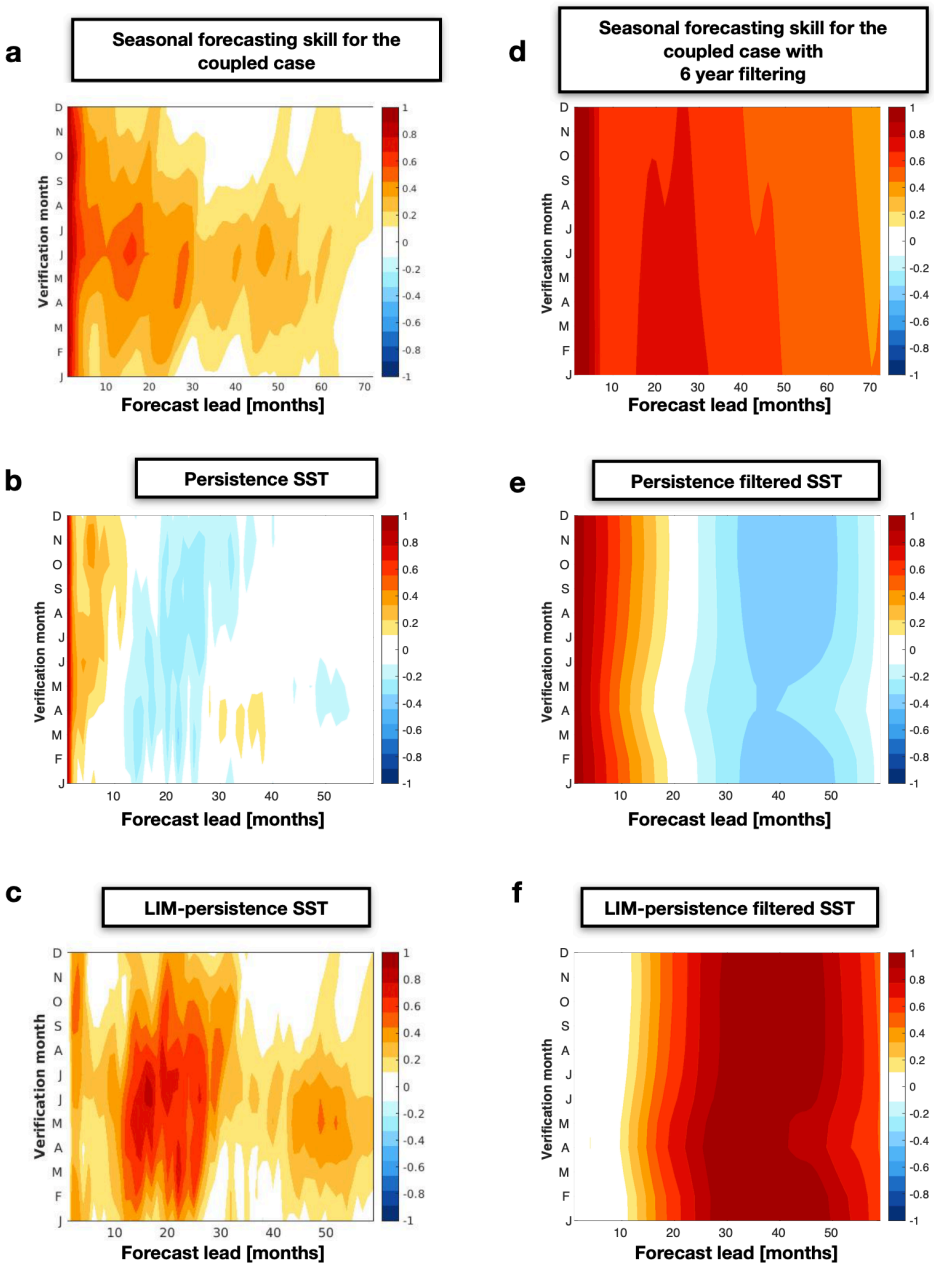

Figure 3.4: KOE SSTa index forecast correlation skill as a function of the initialization month of the year from the physics only LIM (a), the persistence (b), and their difference (c). The same correlation skill maps are shown but computed after applying a 6-year low-pass filter applied on the original and forecasted monthly data (d)(e), and (f).

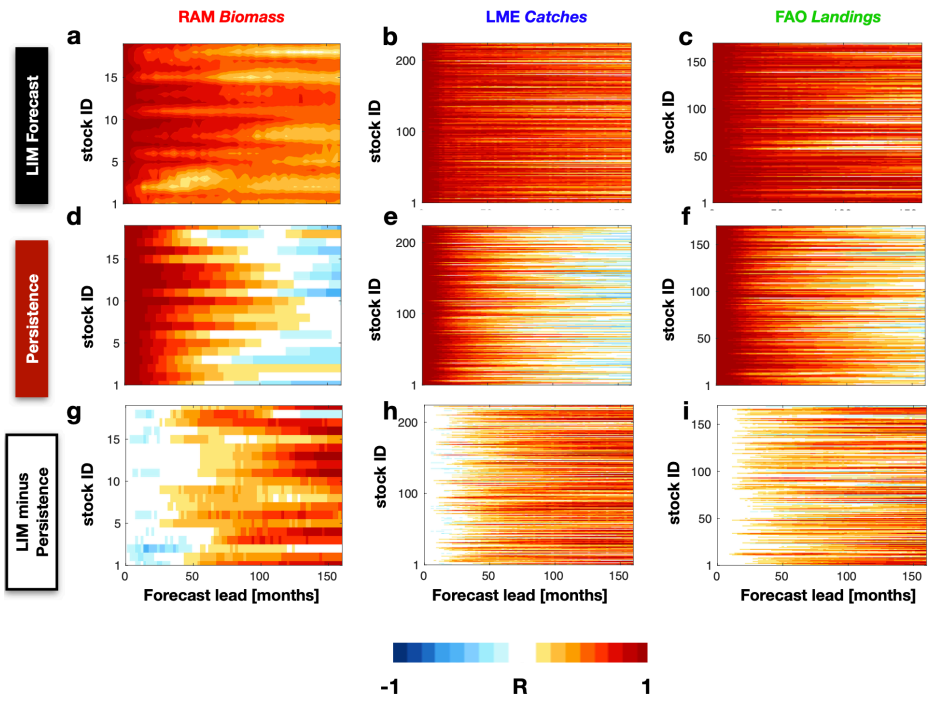

Figure 3.5: The LIM forecasting correlation skill as a function of different lead-times is displayed from the RAM (a), LME (b), and FAO (c) stocks. The persistence correlation skill for each of these stock is also shown for comparison in (d), (e), and (f). A different between the skill of the LIM minus persistence is shown in (g), (h), and (i).

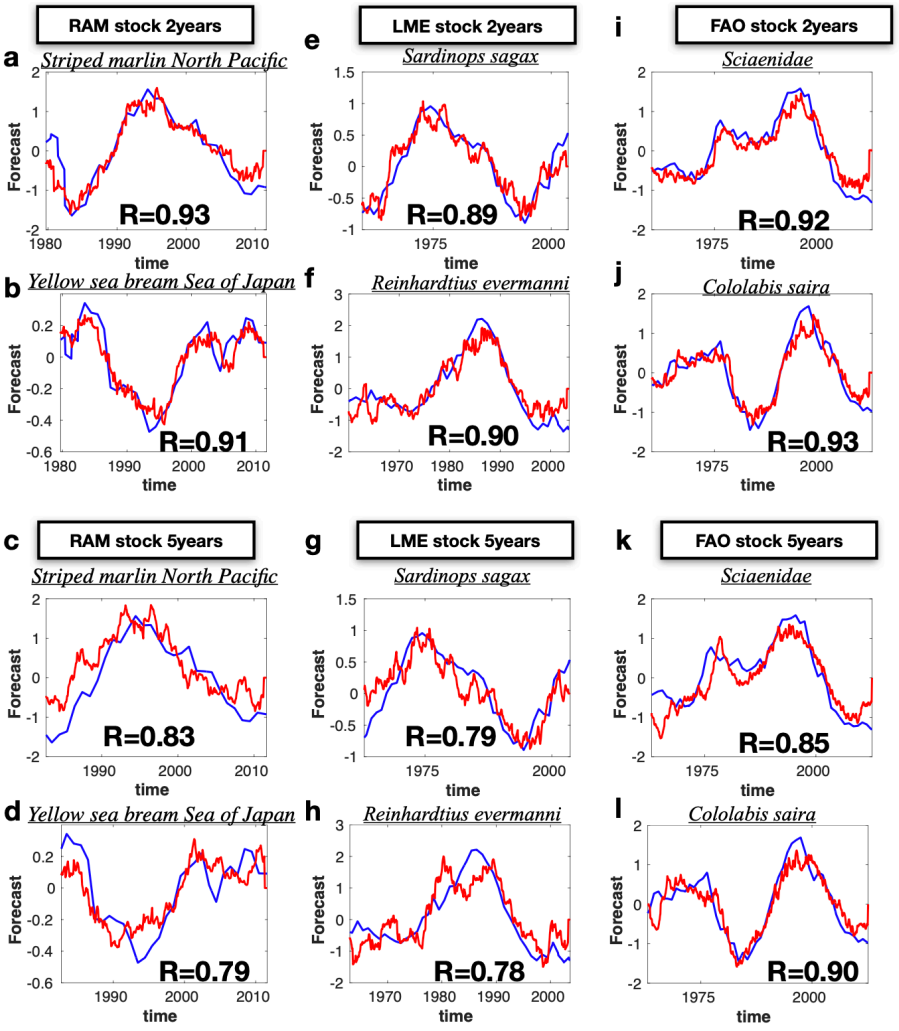

Figure 3.6: Selected single stock time series (blue lines) and the forecasted time series (red lines). The stock have been selected considering those that have the highest difference between forecasting LIM skill and the persistence. The 2- year lead forecast are shown for the RAM (a,b), for LME (e,f) and for the FAO(i,j). The same comparison are shown for the 5-year lead forecast in panels (c,d) for RAM, (g,h) for LME, and (k,l) for FAO. The name of the selected stock is displayed at the top of each panel

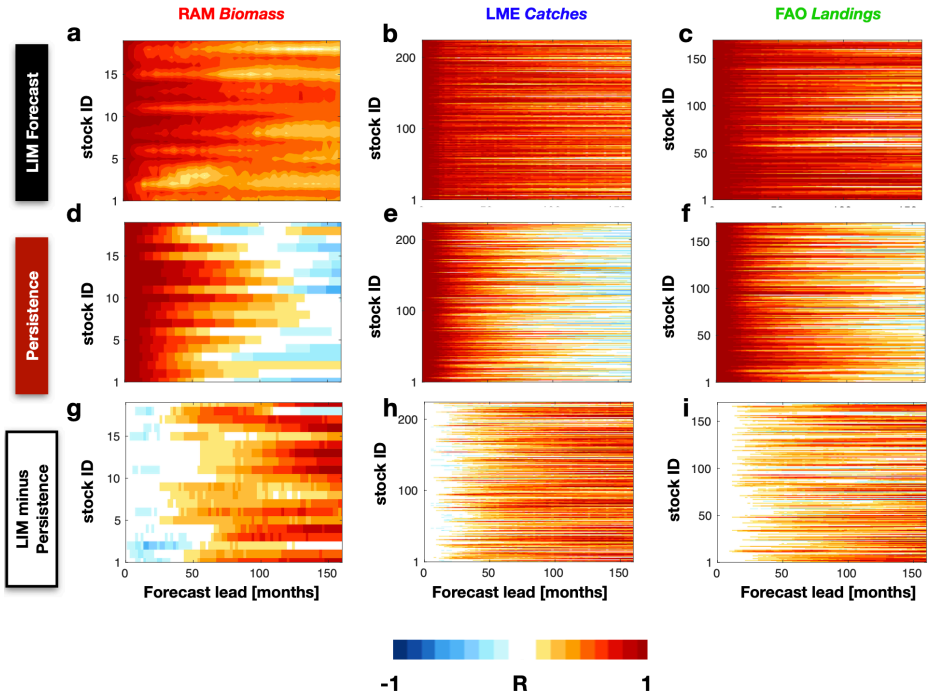

Figure 3.7: Same as Figure 5, except showing the forecast skill of the LIM where the physics and fish sticks are decoupled, (a) RAM, (b) LME, (c) FAO. The differences in skill between the decoupled and the full LIM case are shown in (d), (e), and (f). The forecasting correlation skill as a function of different lead-times is displayed also for a LIM where each stock is forecasted independently are shown for the RAM (g), LME (h), and FAO (i) datasets, along with the differences from full LIM case in panels (d), (e), and (f), respectively.

CHAPTER 4

CONCLUSION AND FUTURE RESEARCH

A large part of this dissertation is based on the idea that external physical drivers of the North Pacific region are a key source of predictability for marine ecosystems. Specifically, we have considered the impacts of large-scale climate modes of variability such as the Pacific Decadal Oscillation (PDO) and the North Pacific Gyre Oscillation (NPGO). These modes have an important influence on the ecological dynamics of the Kuroshio-Oyashio region (Chapter I).

Previous studies have linked the PDO ecological impacts to changes in nutrient availability that are caused by seasonal changes in mixed layer processes driven by the wind-stress curl pattern of the PDO. Similarly, the NPGO has been shown to control the changes in mean advection of the KOE and distribution of zooplankton [Chiba et al. 2013]. The relationships between these physical climate processes and the ecological dynamics of the North Pacific are also evident in the significant covariability between the SSH and the Chl-a, which is an indirect measure of phytoplankton abundance. To better emphasize how this covariability tracks the main dominant North Pacific modes we have performed an SVD analysis. From the analysis, we identify two main modes of covariability, which are associated with a poleward shift of the KOE (e.g. PDO, the first single pattern mode) and to an intensification of the current (e.g. NPGO, the second mode). As our observational data does not allow us to identify a climate change signature in the short 30-years data record, we considered 29 simulations of the Coupled Earth System Model (CESM) over the period 1900-2100, and 23 models from the 5th Coupled Model Intercomparison Project (CMIP5). These simulations use transient external forcings over the observed historical record (e.g. increases in greenhouse gases) and the Representative Concentration Pathway scenario of climate change version 8.5 (RCP8.5) from 2000-2100. From difference maps

of mean SSH between 1950-2000 and 2050-2100, we find a meridional dipole structure that projects onto an intensification and poleward shift of the Kuroshio-Oyashio Extension (KOE) leading also to an increase in downwelling over the subtropics. We link these changes to an increased SLP gradient between the polar and the subpolar regions with a 10 Pascal increase in the gradient, which corresponds to 35% of the total gradient. The change in SLP gradient between the poles and the tropics leads to intensified Westerlies and a shift of the winds to Northern Latitudes, which consequently induces a poleward shift also on the KOE mean circulation axis. The change in the variability associated with the first and the second modes has been analyzed by looking at the trend in the variance of the first and second principal components (PCs) of SSH. The importance of looking at the SSH variance is because of it's biological implications regarding an increase in synchrony of how marine populations respond to a climate perturbation. Specifically, it has been suggested that marine ecosystems may behave more synchronously when the variance of the climate signals is stronger, which in turn make them more vulnerable to collapse and extinction due to the portfolio effect. Therefore the positive trend found in the SSH variability can have important consequences on the ecological dynamics of the North Pacific. To further analyze the significance of the trend we have performed a Monte Carlo test using 10000 random PCs. The first PC of the SSH displays a positive increase in the trend which is statistically significant in both the CESM and the CMIP5. For the second we find significant changes in variance only in the CESM ensemble but not the CMIP5. These results may be linked to the models' inability to capture the NPGO dynamics (Chapter II).

Given the importance of SSH and SST for the North Pacific marine ecosystem, we proceed to build a forecasting model where the Reanalysis data of SST and SSH have been used as predictors. The methodology relies on a Linear Inverse Model, which previous studies have successfully used to forecast the SST in different oceanic basins [Newman et al. 2007]. We have applied the LIM on a set of fish stock indicators, which we are considered proxies to simplify complicated trends always present in ecosystems. Specifically,

we have analyzed the biomass anomalies from the Restricted Access Management (RAM) database, the catches from the Large Marine Ecosystem database (LME), and the landings from the Food and Aquaculture Organization (FAO) database. We found that the LIM was able to forecast the fishery time series beyond the persistence time scale. To further analyze the importance of the ecosystem as a whole we conducted a series of sensitivity analyses, which revealed the important role played by the SST/SSH of the North Pacific as predictors of the fish indicators. While the LIM did not allows us to directly explore the mechanisms that lead to the increase in forecasting skill and to the links between climate and fisheries, we speculate based on previous studies [Jacox et al. 2020] that ocean advection processes linked to the arrival of Westward propagating Rossby waves from the Central North Pacific are important. These waves are formed following wind stress curl anomalies induced by the PDO and the NPGO and propagate westward to the KOE with a time lag of 2-3 years. The arrival of the Rossby wave is responsible for changes in the eastward transport of the jet and consequently impacts the local marine ecosystem processes. Also, it has been found that the Rossby waves change the depth of the nutricline and therefore impact the nutrient availability and the trophic food chain including fish. To explore the importance of interactions within fish species we have conducted a second sensitivity analysis where the LIM has been run for each stock individually. We find that for most species the skill is reduced, although this is highly dependent on the type of stock. We conclude that some stocks have internal population interaction dynamics that play an important role in the skill (Chapter III).

As a future direction for this work, the Linear Inverse Model analysis will be expanded to a different set of data and compared with the forecast skill derived from deep learning methods. The Gated Recurrent Unit neural network and the Encoder-Decoder model are examples of methods that have the potential to better capture the nonlinearity of fish indicators. These data mining tools have shown promise in several fields of science ranging from computer vision to natural language processing [LeCun et al.2015] and they are becoming

commonly used also in climate science. The Encoder-Decoder model falls under the class of recurrent neural network (RNN), which are sequence models more advance than traditional neural network introduced by [Kyunghyun Cho et al. 2014]. They have been widely used for time series forecasting tasks, from SST prediction [Nadiga et al. 2021] to Chl-a forecasting [Chen et al. 2015]. Despite their successful applications, however, traditional RNNs have two disadvantage with regard to the lower number of parameters, which can result in a more difficult optimization, and the vanishing gradient problem, where the gradient used by the neural network to update the parameters become zero. In recent years, a more recent type of neural network, the Long Short Term Memory (LSTM) has been developed [Hochreiter et al., 1997] to overcome these issues. In our future work, we plan to use a more advanced version of LSTM based on an Encoder-Decoder approach, where the model has a first LSTM network (the encoder) that reads the historical sequence to a fixed length vector, while the second LSTM (the decoder) predict the future workload value. To the extent that nonlinearity and nonlinear relationship between climate and marine ecosystems are important, we anticipate that the application of the improved Encoder-Decoder methods will lead to an improvement in forecast skill with respect to the LIM approach presented in Chapter III.

4.1 References

Chen, Qiuwen & Guan, Tiesheng & Yun, Liu & Li, Ruonan & Recknagel, Friedrich. (2015). Online forecasting chlorophyll a concentrations by an auto-regressive integrated moving average model: Feasibilities and potentials. Harmful Algae. 43. 10.1016/j.hal.2015.01.002.

Nadiga, B. T. (2021). Reservoir computing as a tool for climate predictability studies. Journal of Advances in Modeling Earth Systems, 13, e2020MS002290. https://doi. org/10.1029/2020MS00229

Chiba, S., Di Lorenzo, E., Davis, A., Keister, J. E., Taguchi, B., Sasai, Y., and Sugisaki, H. (2013), Large-scale climate control of zooplankton transport and biogeography in the Kuroshio-Oyashio Extension region, Geophys. Res. Lett., 40, 5182– 5187, doi : $10.1002/grl.50999$.

Hochreiter, S., and Schmidhuber, J. (1997). Long Short-Term Memory. Neural Comput. 9, 1735–1780. doi:10.1162/neco.1997.9.8.1735

Kyunghyun Cho, Bart van Merriënboer, Caglar Gulcehre, Dzmitry Bahdanau, Fethi Bougares, Holger Schwenk, and Yoshua Bengio. 2014. Learning Phrase Representations using RNN Encoder–Decoder for Statistical Machine Translation. In Proceedings of the 2014 Conference on Empirical Methods in Natural Language Processing (EMNLP), pages 1724–1734, Doha, Qatar. Association for Computational Linguistics

LeCun, Y., Bengio, Y. & Hinton, G. Deep learning. Nature 521, 436–444 (2015). https://doi.org/10.1038/nature14539

Newman, M. (2007). Interannual to Decadal Predictability of Tropical and North Pacific Sea Surface Temperatures, Journal of Climate, 20(11), 2333-2356. Retrieved Dec 6, 2022, from https://journals.ametsoc.org/view/journals/clim/20/11/jcli4165.1.xml

Jacox, Michael & Alexander, Michael & Siedlecki, S. & Chen, Ke & Kwon, Young-Oh & Brodie, Stephanie & Ortiz, Ivonne & Tommasi, Desiree & Widlansky, Matthew & Barrie, Daniel & Capotondi, Antonietta Cheng, Wei & Di Lorenzo, Emanuele & Edwards, Chris & Fiechter, Jerome & Fratantoni, Paula Hazen, Elliott & Hermann, Albert & Kumar, Arun & Rykaczewski, Ryan. (2020). Seasonal-to-interannual prediction of U.S. coastal marine

ecosystems: Forecast methods, mechanisms of predictability, and priority developments. Progress in Oceanography. 183. 102307. 10.1016/j.pocean.2020.102307.

Appendices

APPENDIX A

APPENDIX CHAPTER 2

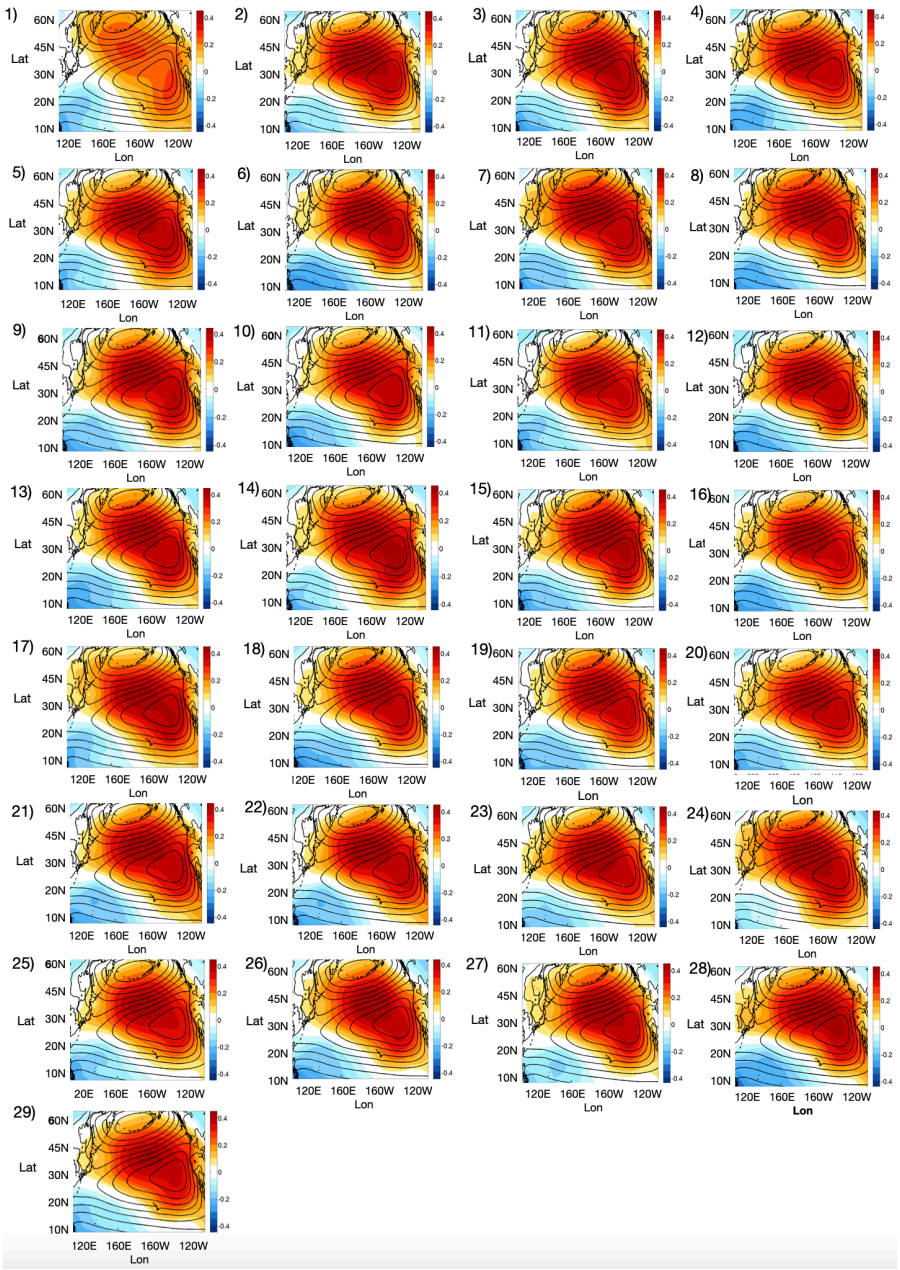

Figure A.1: Figures 1-29 represents correlation map obtained by the projection of the SLP anomalies on the first pc of SSH calculated with CESM-LE output runs. In this case each single output has been considered.

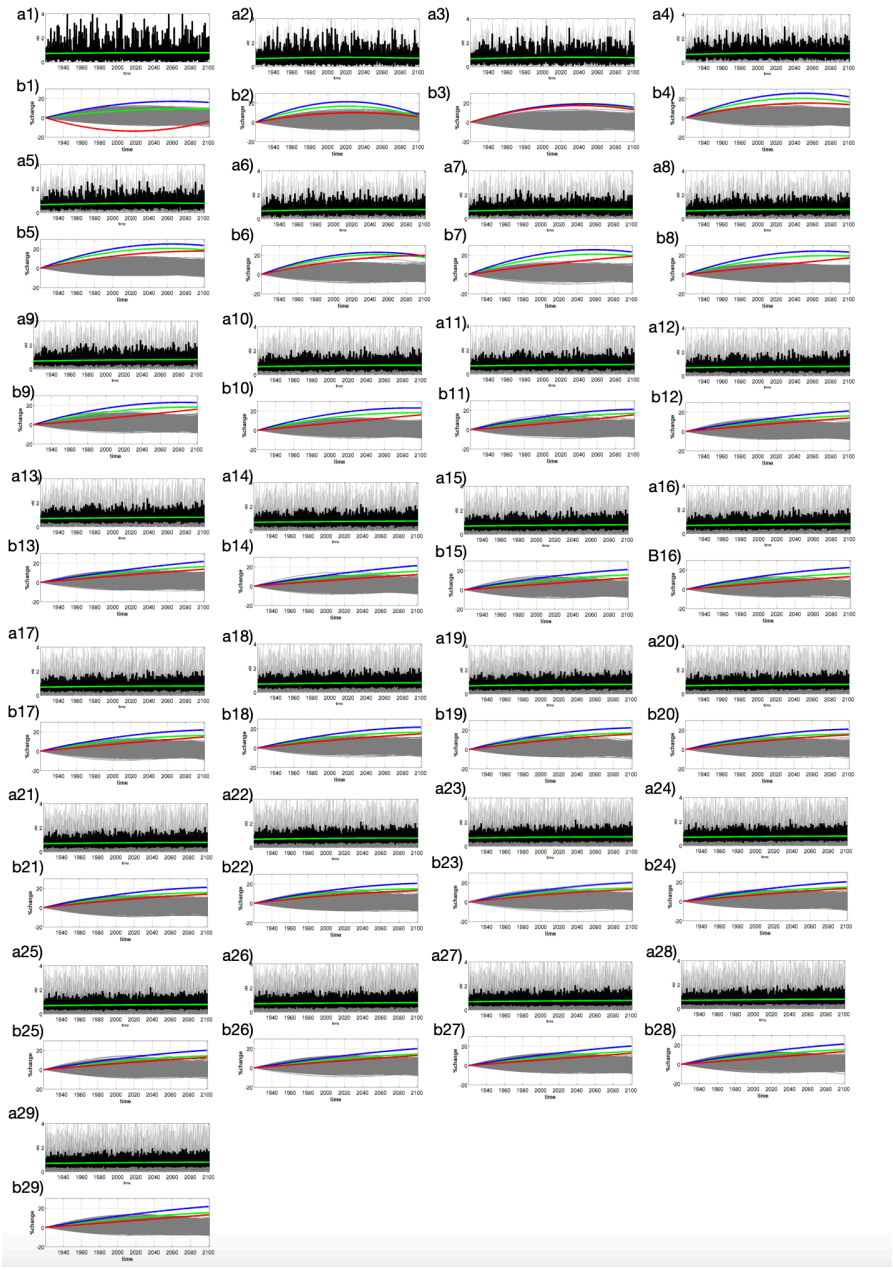

Figure A.2: Variance trend of the PSL. In Figures a1-a29 the principal component and the mean pc(in black) are displayed. The trend is associated to the patterns obtained from the projection of PSL anomalies on the first pc of SSH. While in figures b1-b29 the trend in SLP variability for each singular model is represented. The CESM has been used

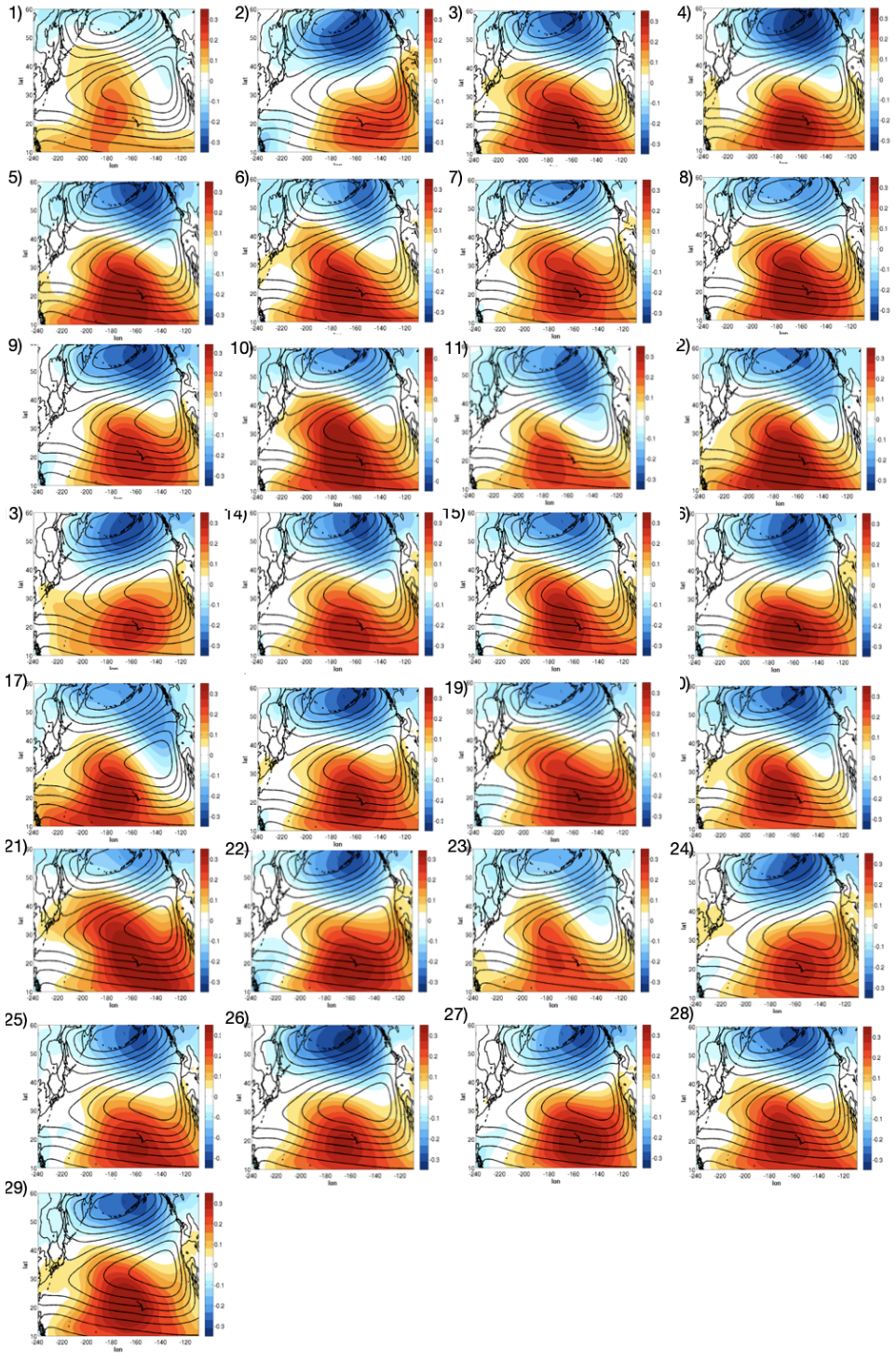

Figure A.3: In Fig.1-29 we represent correlation map obtained by the projection of the SLP anomalies on the second pc of SSH. In this case the CESM models have been used

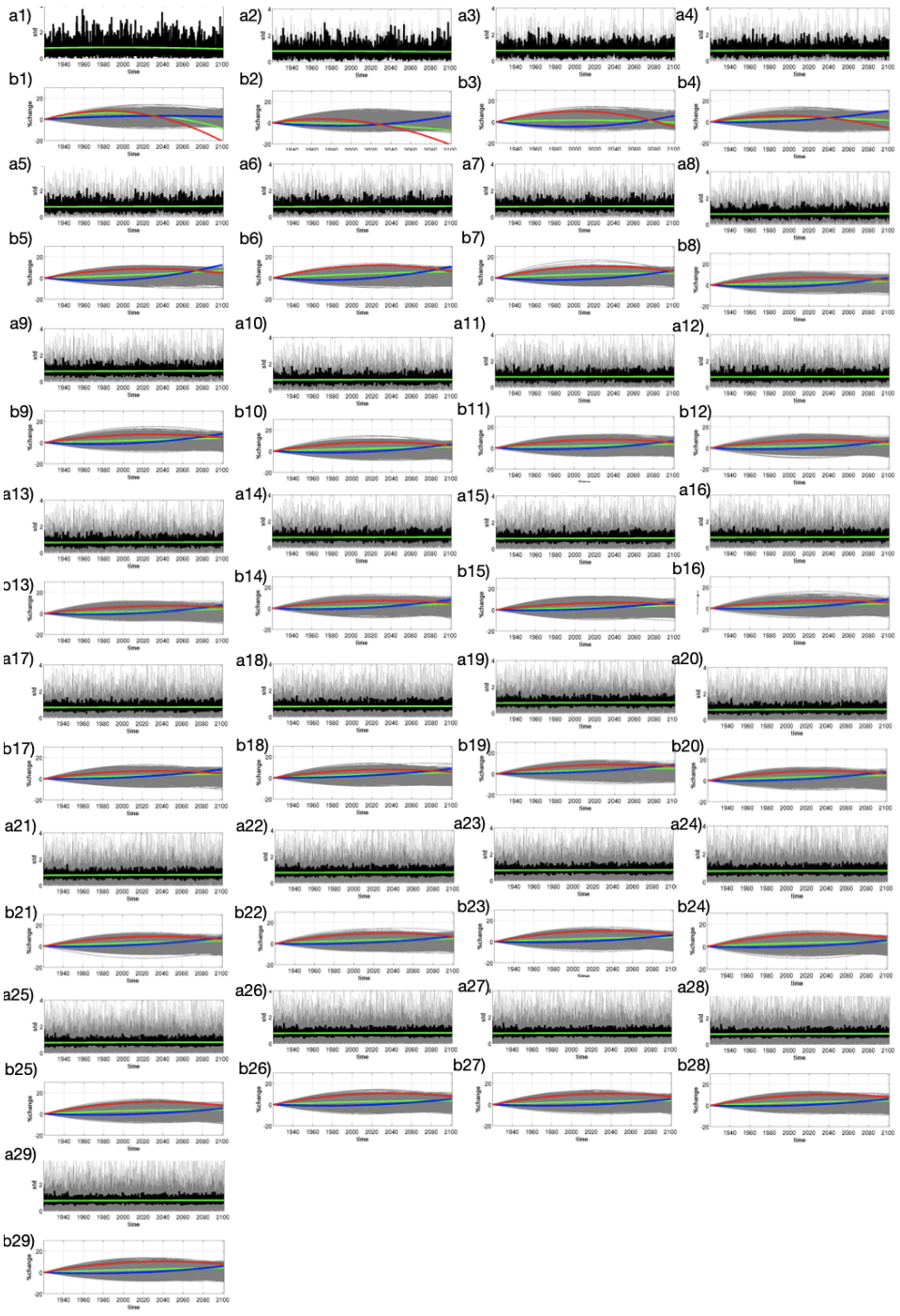

Figure A.4: variance trend of the SLP. In Figures a1-a29 the principal component and the mean pc(in black) are displayed. The trend is associated to the patterns obtained from the projection of SLP anomalies on the second pc of SSH. While in figures b1-b29 the trend in SLP variability for each singular model is represented. The CESM has been used

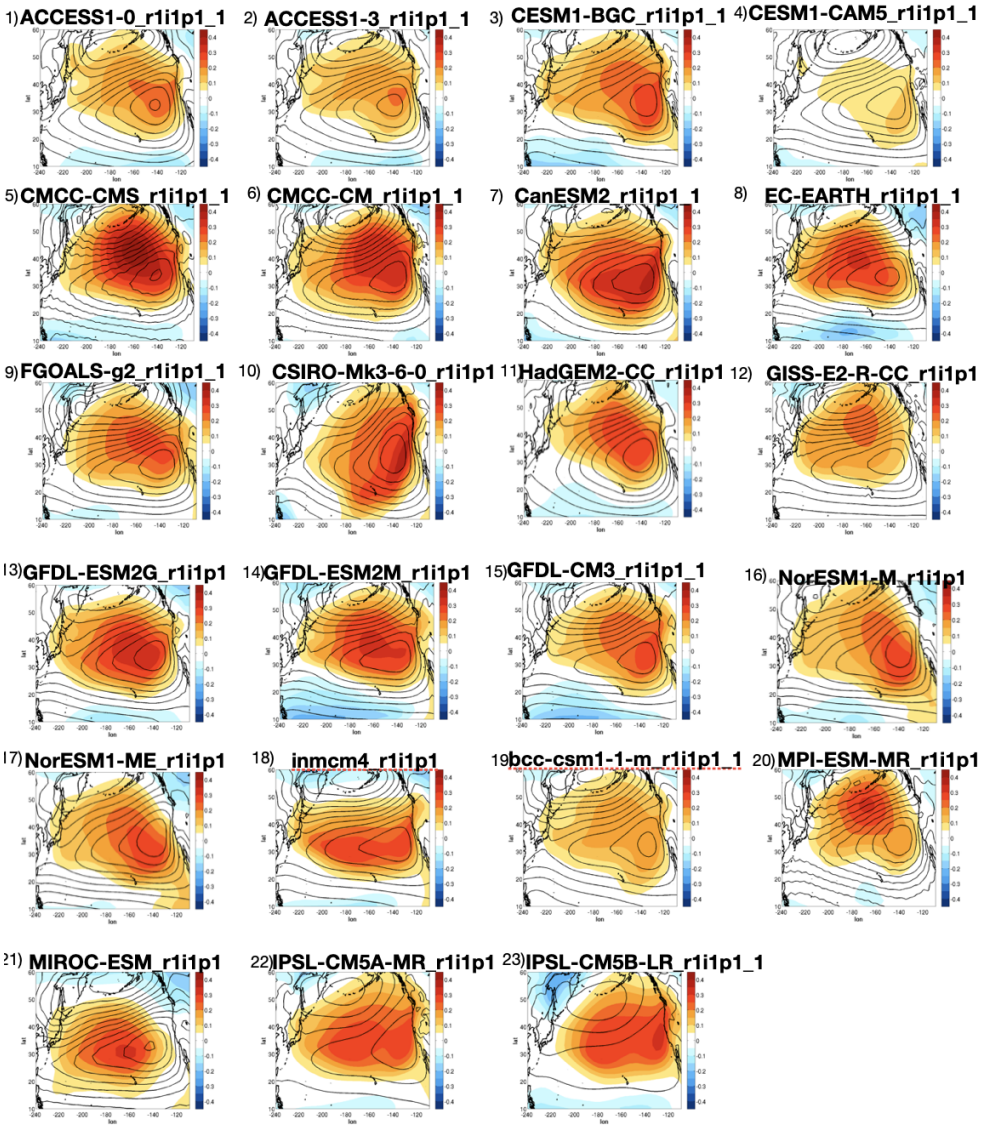

Figure A.5: In Fig.1-23 we represent correlation map obtained by the projection of the SLP anomalies on the first pc of SSH. In this case the CMIP5-E models have been used.

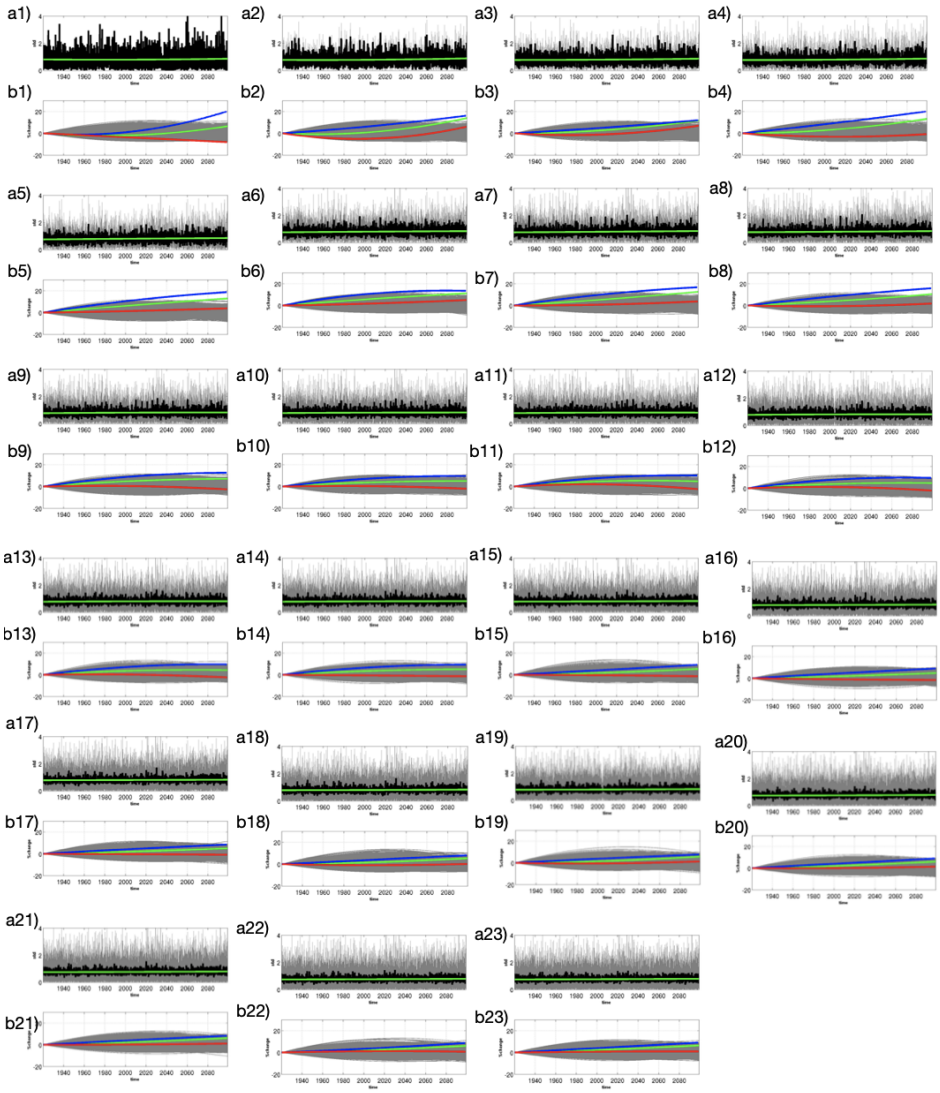

Figure A.6: variance trend of the PSL using the CMIP5-E models. In Figures a1-a29 the principal component and the mean pc(in black) are displayed. The trend is associated to the patterns obtained from the projection of PSL anomalies on the first pc of SSH. While in figures b1-b29 the trend in SLP variability for each singular model is considered.

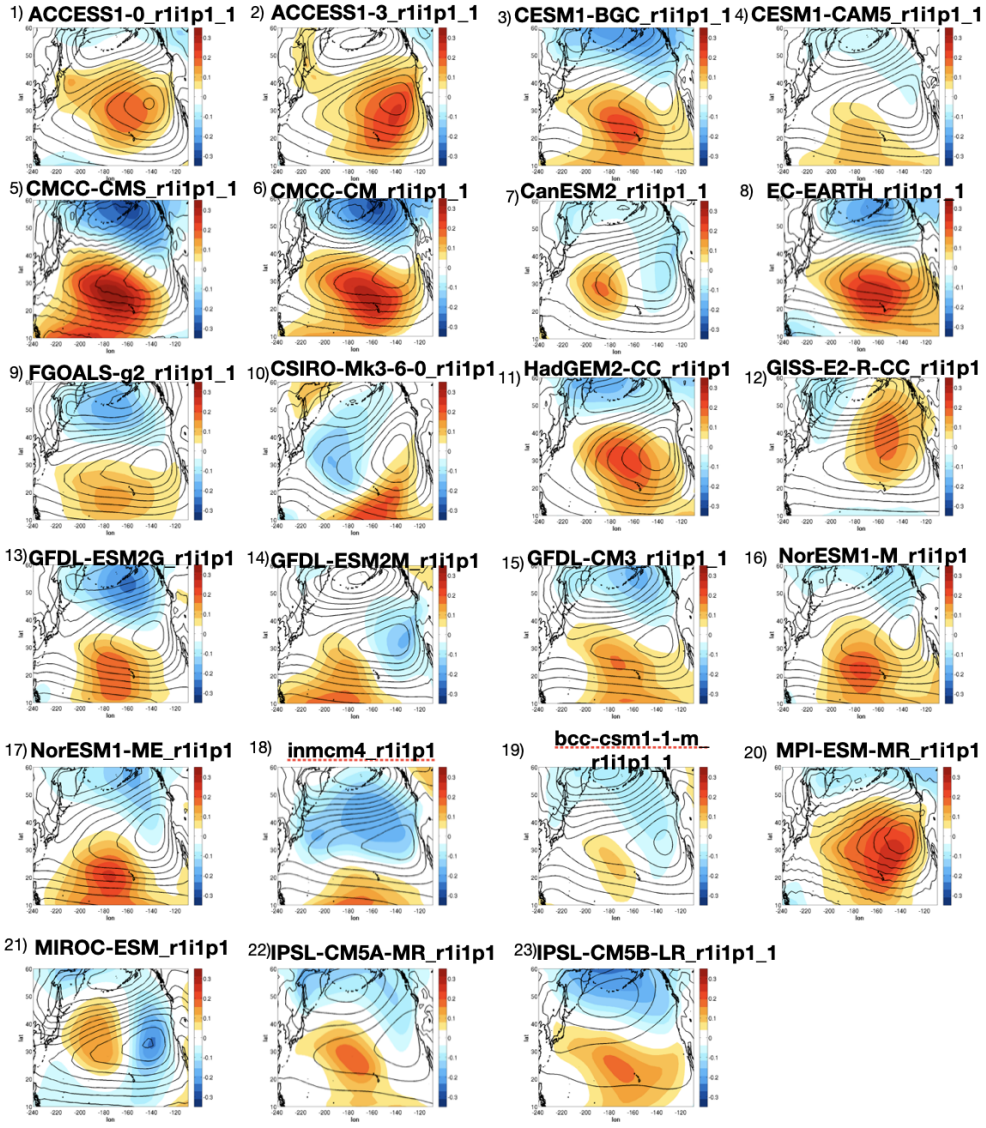

Figure A.7: In Fig.1-23 we represent correlation maps obtained by the projection of the SLP anomalies on the second pc of SSH. In this case the CMIP5-E have been used.

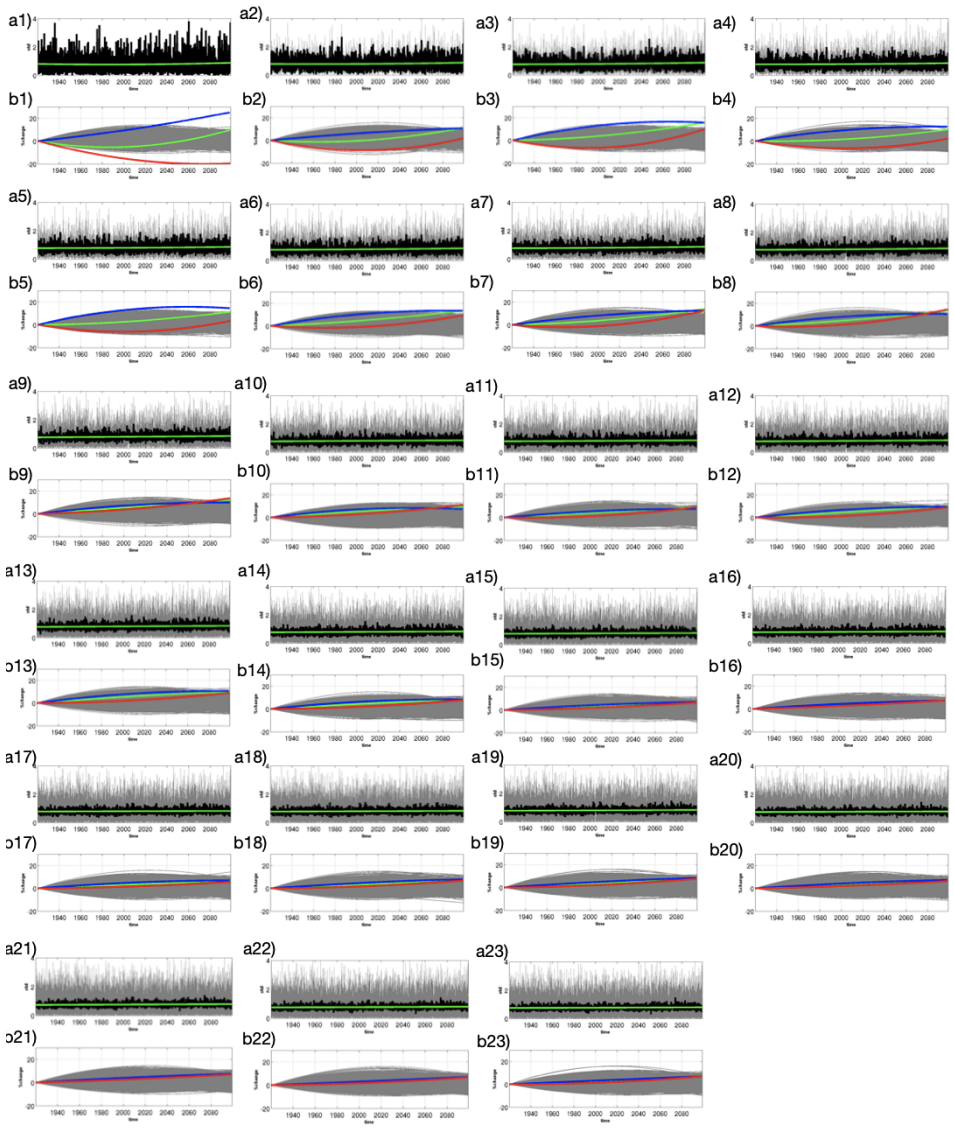

Figure A.8: variance trend of the PSL using the CMIP5-E models. In Figures a1-a29 the principal component and the mean pc(in black) are displayed. The trend is associated to the patterns obtained from the projection of PSL anomalies on the second pc of SSH. While in figures b1-b29 the trend in SLP variability for each singular model is considered.

APPENDIX B

APPENDIX CHAPTER 3

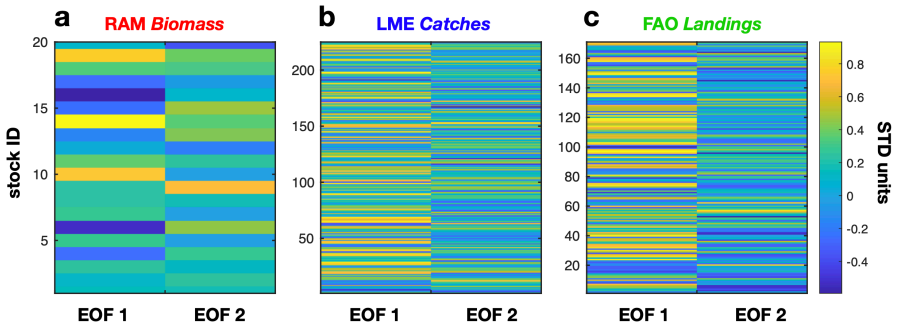

Figure S1. The first and second EOF weights for the RAM Biomass (a), the LME catches (b), and FAO landings (c).

Figure B.1: The first and second EOF weights for the RAM Biomass (a), the LME landings (b), and FAO catches (c).

Table B.1: RAM stocks

StockID	RAM fishery stock
1	Bigeye tuna Western Pacific Ocean
2	Striped marlin Southwestern Pacific Ocean
3	Blue marlin Pacific Ocean
4	Pacific bluefin tuna Pacific Ocean
5	Striped marlin Western and Central North Pacific
6	Albacore tuna North Pacific
7	Swordfish North Pacific
8	Striped marlin North Pacific
9	Alaskan Pollock Pacific Coast of Japan
10	Yellow sea bream Sea of Japan
11	Chub mackerel Pacific Coast of Japan)
12	Chub mackerel Tsushima Strait
13	Japanese anchovy Pacific Coast of Japan
14	Japanese anchovy Inland Sea of Japan
15	Japanese anchovy Tsushima Strait
16	Jack mackerel Pacific Coast of Japan
17	Japanese jack mackerel Tsushima Strait
18	Red seabream Inland Sea of Japan (East)
19	Red seabream Inland Sea of Japan (West)
20	Round herring Tsushima Strait'

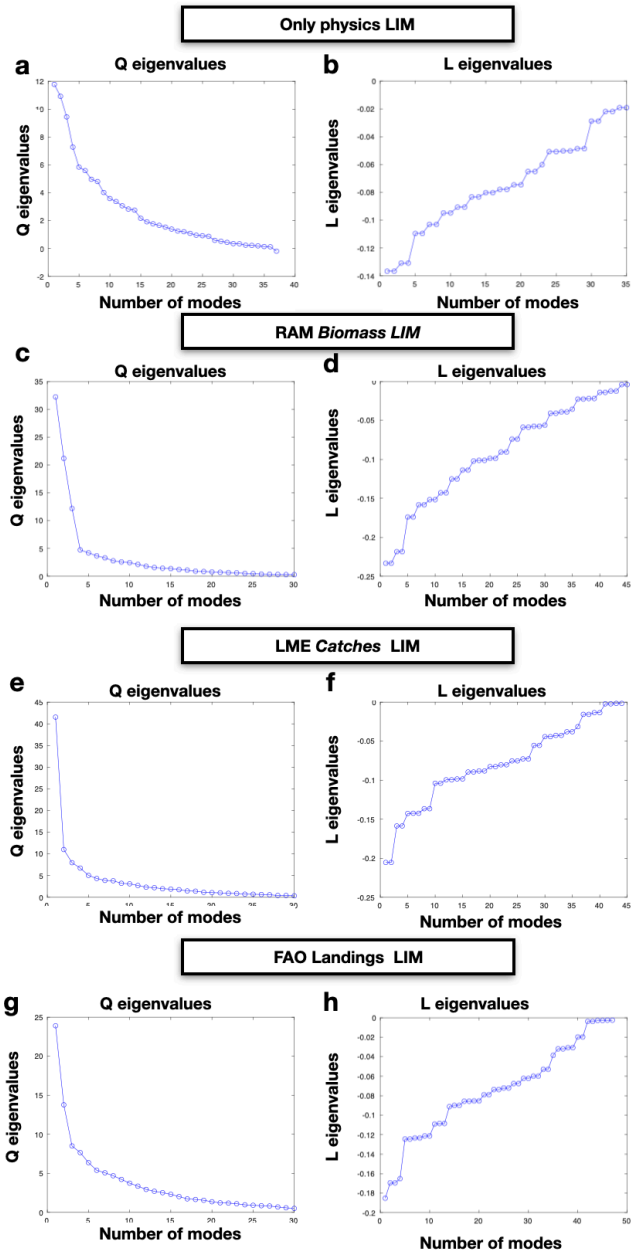

Figure B.2: Eigenvalue spectra of the LIM operator L (a) and the spectra of the matrix Q (b) for the LIM containing only SST and SSH. The same calculation has been done in (c) and(d) for the RAM LIM, in (e) and (f) for the LME LIM and in (g) and (h) the FAO LIM.

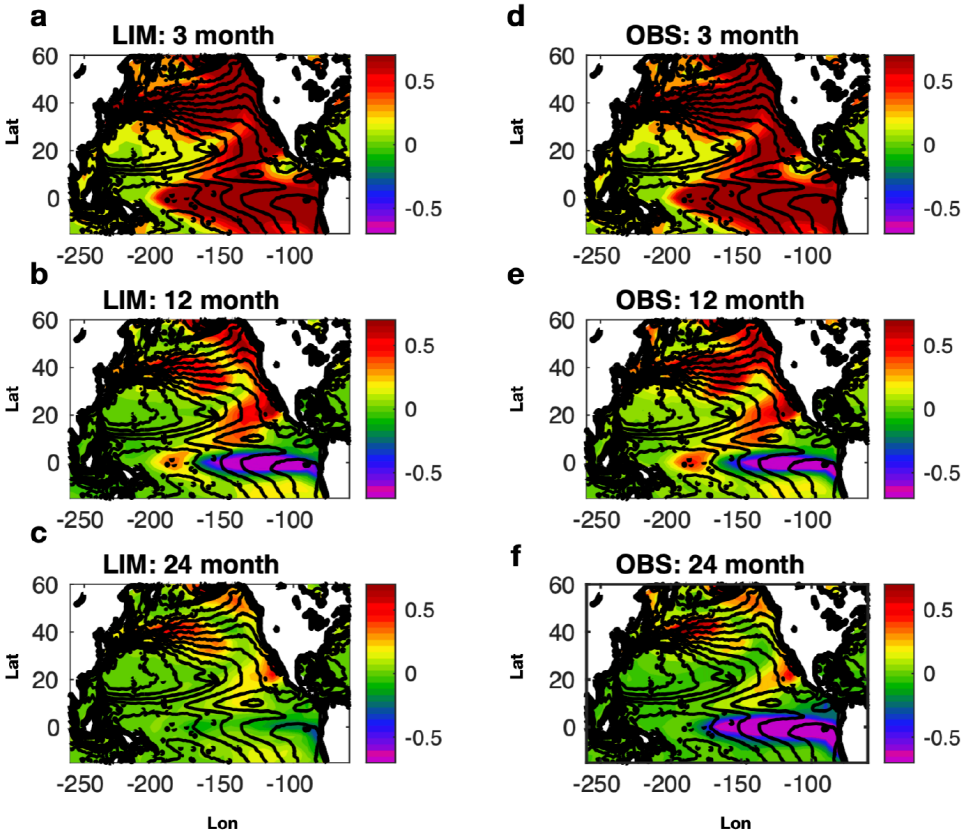

Figure B.3: LIM tau test applied to the SST forecast LIM. In column (a)-(c) we compute the lag Covariance matrix with the LIM up to 2 years of leading time. The results are compared with the lag covariance matrix from the observational data (d)-(f).

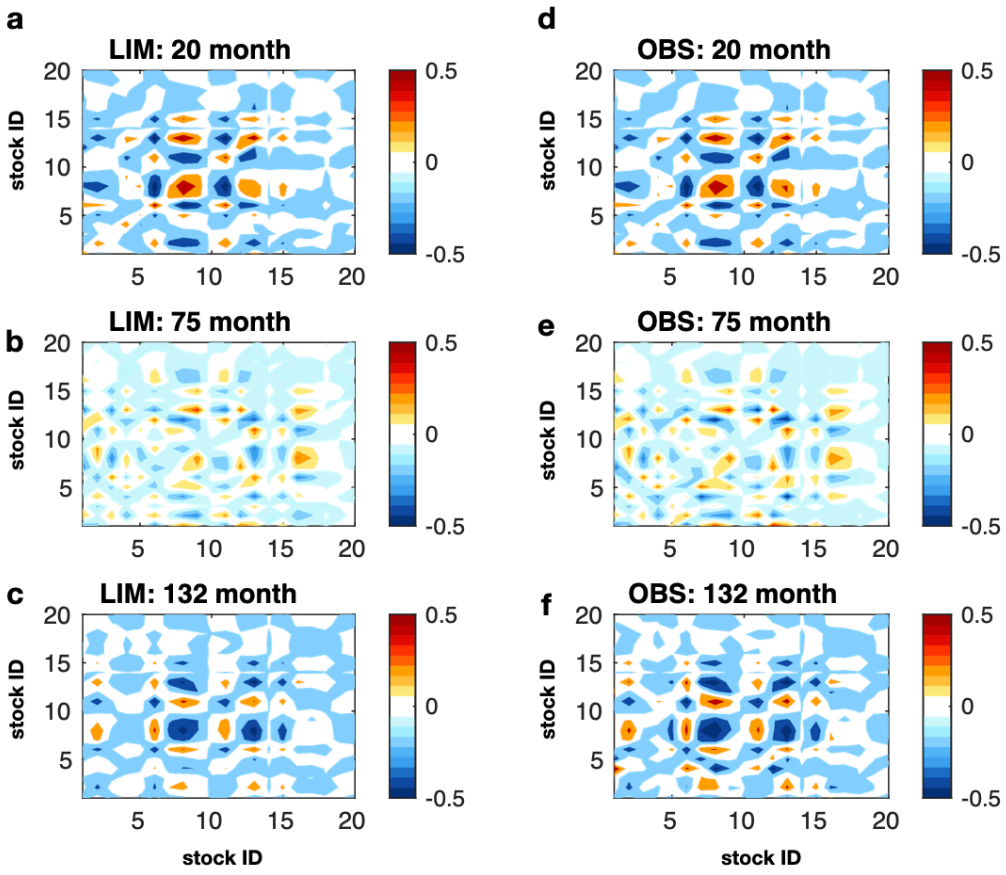

Figure B.4: LIM tau test for the RAM stocks. The test consists in calculating the covariance matrix with the state vector (d)(e)(f) and compare the results with the same matrix obtained from the LIM (a)(b)(c). The calculation is done at different lags up to 132 months.

Table B.2: LME stocks

StockID	Name	StockID	Name	StockID	Name
1	Haliotis gigantea	2	Larimichthys polyactis	3	Epinephelus
4	Trachurus japonicus	5	Thunnus alalunga	6	Clupeiformes
7	Oncorhynchus keta	8	Hypoptychus dybowskii	9	Chrysophrys auratus
10	Elasmobranchii	11	Scapharca subcrenata	12	Chionoecetes
13	Ariidae	14	Paralichthys olivaceus	15	Takifugu vermicularis
16	Thunnus albacares	17	Crustacea	18	Paralithodes
19	Portunus trituberculatus	20	Apostichopus japonicus	21	Pleuronectiformes
22	Ammodytes personatus	23	Sebastes alutus	24	Chelidonichthys kumu
25	Auxis	26	Nibea mitsukurii	27	Scomber japonicus
28	Penaeus	29	Cynoglossidae	30	Etrumeus teres
31	Strongylocentrotus	32	Katsuwonus pelamis	33	Pectinidae
34	Crassostrea	35	Penaeus monodon	36	Crassostrea gigas
37	Bivalvia	38	Oncorhynchus nerka	39	Scorpaenidae
40	Sciaenida	41	Oncorhynchus tshawytscha	42	Arctoscopus japonicus
43	Thunnus obesus	44	Pleurogrammus azonus	45	Scomberomorus niphonius
46	Theragra chalcogramma	47	Ruditapes philippinarum	48	Engraulis japonicus
49	Salmonidae	50	Sepiidaes	51	Cololabis saira
52	Haliotis	53	Mactra sachalinensis	54	Xiphias gladius
55	Teuthida	56	Thunnus orientalis	57	Coryphaena hippurus

Table B.3: LME stocks part2

58	Oncorhynchus kisutch	59	Glossanodon semifasciatus	60	Larimichthys croceus
61	Clupea pallasii	62	Todarodes pacificus	63	Panulirus longipes
64	Meretrix lusoria	65	Muraenesox cinereus	66	Stromateidae
67	Trichiurus lepturus	68	Caranx	69	Rajiformes
70	Sparidae	71	Spratelloides gracilis	72	Sardinops sagax
73	Pennahia argentata	74	Pecten yessoensis	75	Acetes japonicus
76	Marine fishes not identified	77	Makaira indica	78	Decapterus maruadsi
79	Brachyura	80	Loligo	81	Exocoetidae
82	Octopodidae	83	Mugil cephalus	84	Chirocentrus dorab
85	Metapenaeus	86	Oncorhynchus gorbuscha	87	Cheilopogon agoo
88	Seriola	89	Penaeus japonicus	90	Clupanodon thrissa
91	Shrimps prawns	92	Psenopsis anomala	93	Crassostrea gigas
94	Trachurus japonicus	95	Reinhardtius evermanni	96	Katsuwonus pelamis
97	Eleginus gracilis	98	Chrysophrys auratus	99	Scomber japonicus
100	Oncorhynchus nerka	101	Oncorhynchus keta	102	Marine fishes not identified
103	Oncorhynchus kisutch	104	Paralichthys olivaceus	105	Osmeridae
106	Mugil cephalus	107	Pseudopleuronectes herzensteini	108	Penaeus monodon
109	Pecten yessoensis	110	Mactra sachalinensis	111	Oncorhynchus tshawytscha
112	Takifugu vermicularis	113	Clupeiformes	114	Gadus macrocephalus
115	Auxis	116	Haliotis	117	Bivalvia
118	Scorpaenidae	119	Metapenaeus	120	Chionoecetes
121	Paralithodes camtschaticus	122	Paralithodes	123	Theragra chalcogramma
124	Sciaenidae	125	Acetes japonicus	126	Sebastes alutus
127	Octopodidae	128	Strongylocentrotus	129	Xiphias gladius
130	Gobiidae	131	Todarodes pacificus	132	Pleuronectiformes
133	Elasmobranchii	134	Clupea pallasii	135	Stromateidae
136	Shrimps prawns	137	Thunnus obesus	138	Teuthida
139	Pleurogrammus azonus	140	Sardinops sagax	141	Sepiidae
142	Thunnus alalunga	143	Engraulis japonicus	144	Cynoglossidae
145	Salmonidae	146	Cololabis saira	147	Hypoptychus dybowskii
148	Thunnus albacares	149	Apostichopus japonicus	150	Ammodytes personatus
151	Brachyura	152	Arctoscopus japonicus	153	Seriola
154	Sparidae	155	Oncorhynchus gorbuscha	156	Thunnus orientalis
157	Trichiurus lepturus	158	Rajiformes	159	Mugil cephalus
160	Ruditapes philippinarum	161	Teuthida	162	Oncorhynchus nerka
163	Shrimps prawns	164	Gobiidae	165	Chionoecetes
166	Octopodidae	167	Paralithodes camtschaticus	168	Apostichopus japonicus
169	Acetes japonicus	170	Katsuwonus pelamis	171	Stromateidae
172	Panulirus longipes	173	Oncorhynchus gorbuscha	174	Sparidae
175	Starfish and other echinoderms	176	Gadus macrocephalus	177	Pecten yessoensis
178	Sardinops sagax	179	Paralichthys olivaceus	180	Hypoptychus dybowskii
181	Cololabis saira	182	Etrumeus teres	183	Bivalvia
184	Thunnus orientalis	185	Sepiidae	186	Elasmobranchii

Table B.4: LME stocks part3

187	Clupeiformes	188	Salmonidae	189	Clupea pallasii
190	Scomberomorus niphonius	191	Trachurus japonicus	192	Reinhardtius evermanni
193	Chrysophrys auratus	194	Paralithodes	195	Coryphaena hippurus
196	Glossanodon semifasciatus	197	Penaeus monodon	198	Rajiformes
199	Thunnus obesus	200	Oncorhynchus keta	201	Xiphias gladius
202	Sciaenidae	203	Thunnus albacares	204	Eleginus gracilis
205	Strongylocentrotus	206	Cynoglossidae	207	Seriola
208	Arctoscopus japonicus	209	Penaeus japonicus	210	Trichiurus lepturus
211	Auxis	212	Pleuronectiformes	213	Marine fishes not identified
214	Takifugu vermicularis	215	Engraulis japonicus	216	Mactra sachalinensis
217	Brachyura	218	Todarodes pacificus	219	Scorpaenidae
220	Sebastes alutus	221	Theragra chalcogramma	222	Scomber japonicus
223	Metapenaeus	224	Haliotis	225	Osmeridae

Table B.5: FAO stocks part1

1	Scorpaenidae	2	Rajiformes	3	Anoplopoma fimbria
4	Natantia	5	Ophiodon elongatus	6	Saxidomus giganteus
7	Gadus macrocephalus	8	Cancer magister	9	Pleuronectiformes
10	Oncorhynchus tshawytscha	11	Hippoglossus stenolepis	12	Oncorhynchus nerka
13	Oncorhynchus gorbuscha	14	Oncorhynchus keta	15	Clupea pallasii
16	Larimichthys polyactis	17	Sepiidae, Sepiolidae	18	Scomber japonicus
19	Acetes japonicus	20	Larimichthys croceus	21	Mollusca
22	Mollusca	23	Crustacea	24	Trichiurus lepturus
25	Osteichthyes	26	Brachyura	27	Loliginidae, Ommastrephidae
28	Serranidae	29	Stromateidae	30	Cynoglossidae
31	Elasmobranchii	32	Scomberomorus spp	33	Branchiostegidae
34	Decapterus spp	35	Lutjanidae	36	Trichiuridae
37	Caranx spp	38	Sardinella spp	39	Sparidae
40	Stolephorus spp	41	Muraenesox spp	42	Synodontidae
43	Sciaenidae	44	Upeneus spp	45	Nemipterus spp.
46	Natantia	47	Clupea pallasii	48	Thunnus albacares
49	Bivalvia	50	Squalidae	51	Thaleichthys pacificus
52	Anoplopoma fimbria	53	Sebastes alutus	54	Scorpaenidae
55	Hippoglossus stenolepis	56	Oncorhynchus tshawytscha	57	Mammalia
58	Panulirus longipes	59	Penaeus japonicus	60	Scomberomorus niphonius
61	Chionoecetes spp	62	Haliotis gigantea	63	Paralithodes spp
64	Portunus trituberculatus	65	Atheresthes evermanni	66	Hippoglossoides elassodon
67	Sebastes alutus	68	Turbo cornutus	69	Lateolabrax japonicus
70	Psenopsis anomala	71	Pseudocardium sybillae	72	Chionoecetes spp
73	Coryphaena hippurus	74	Mugil cephalus	75	Apostichopus japonicus
76	Glossanodon semifasciatus	77	Paralithodes camtschaticus	78	Paralichthys olivaceus
79	Strongylocentrotus spp	80	Xiphias gladius	81	Arctoscopus japonicus
82	Cypselurus agoo	83	Oncorhynchus kisutch	84	Clupea pallasii
85	Scapharca subcrenata	86	Paralithodes spp	87	Patinopecten yessoensis
88	Meretrix lusoria	89	Dasyatis akajei	90	Chelidonichthys kumu
91	Auxis thazard, A. rochei	92	Pagrus auratus	93	Octopodidae
94	Saurida tumbil	95	Sebastes alutus	96	Muraenesox cinereus
97	Oncorhynchus nerka	98	Thunnus orientalis	99	Clupeoidei

Table B.6: FAO stocks part2

100	Decapterus maruadsi	101	Thunnus obesus	102	Plantae aquaticae
103	Rhodophyceae	104	Oncorhynchus keta	105	Seriola spp
106	Natantia	107	Thunnus alalunga	108	Oncorhynchus gorbuscha
109	Etrumeus teres.	110	Ammodytes personatus	111	Katsuwonus pelamis
112	Ruditapes philippinarum	113	Theragra chalcogramma	114	Bivalvia
115	Pleurogrammus azonus	116	Theragra chalcogramma	117	Laminaria japonica
118	Trachurus japonicus	119	Sardinops melanostictus	120	Todarodes pacificus
121	Engraulis japonicus	122	Cololabis saira	123	Thunnus alalunga
124	Metapenaeus spp	125	Tetrapturus audax	126	Istiophorus platypterus
127	Epinephelus spp	128	Makaira nigricans	129	Mene maculata
130	Ariidae	131	Coryphaena hippurus	132	Larimichthys polyactis
133	Todarodes pacificus	134	Muraenesox cinereus	135	Sepiidae, Sepiolidae
136	Natantia	137	Mugil cephalus	138	Exocoetidae
139	Atrobucca nibe	140	Clupeoidei	141	Makaira indica
142	Pennahia argentata	143	Thunnus albacares	144	Sparidae
145	Saurida tumbil	146	Spratelloides gracilis	147	Auxis thazard, A. rochei
148	Etrumeus teres	149	Sparidae	150	Lophiidae
151	Pleurogrammus azonus	152	Mytilus coruscus	153	Chelidonichthys kumu
154	Arctoscopus japonicus	155	Lateolabrax japonicus	156	Haliotis spp
157	Chlorophyceae	158	Clupanodon thrissa	159	Crassostrea gigas
160	Tetraodontidae	161	Rhodophyceae	162	Sardinops melanostictus
163	Natantia	164	Apostichopus japonicus	165	Paralithodes spp
166	Pagrus auratus	167	Octopodidae	168	Mugil cephalus
169	Muraenesox cinereus	170	Hypoptychus dybowskii	171	Nibea mitsukurii

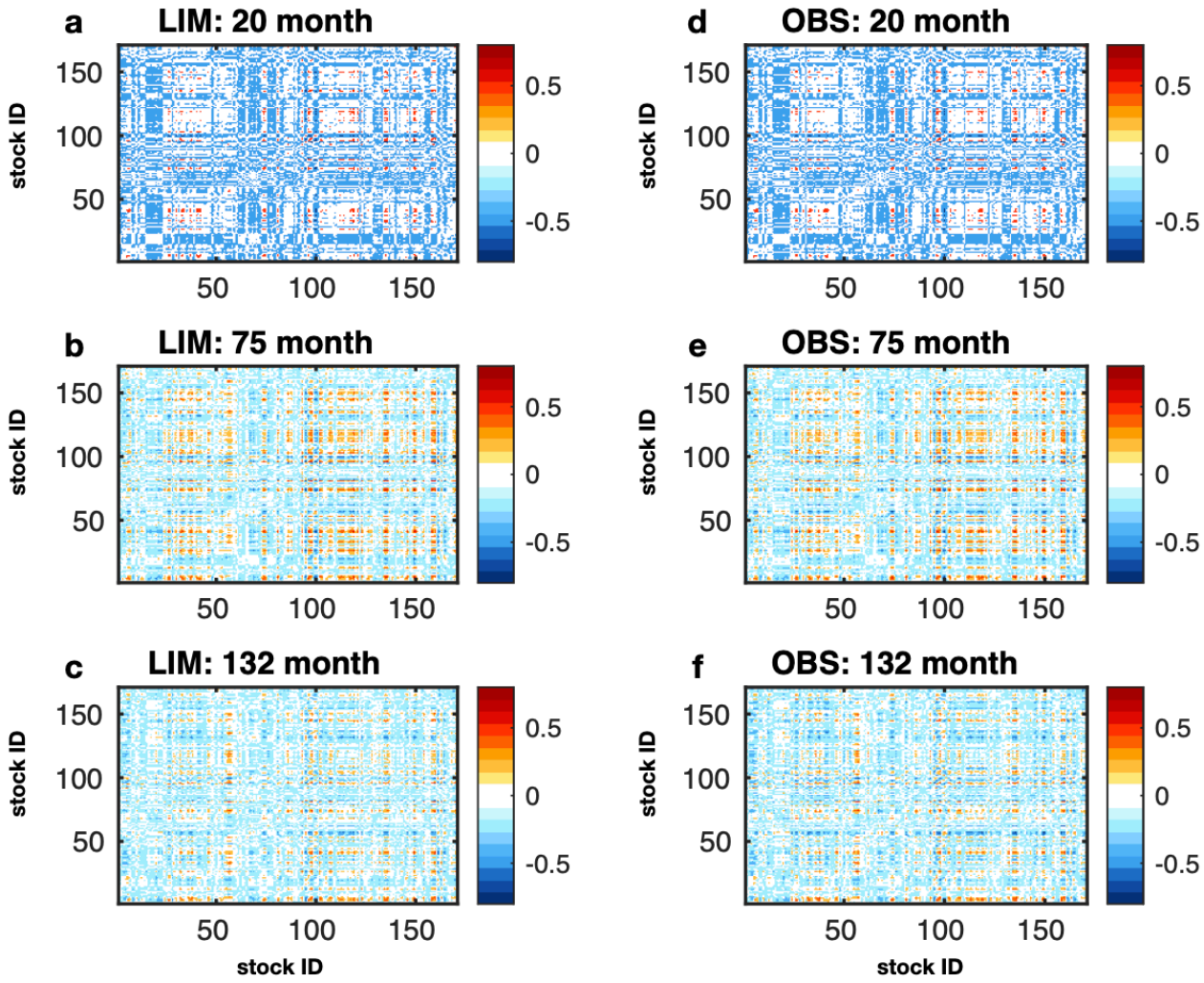

Figure B.5: LIM tau test for the FAO stocks. The test consists in calculating the covariance matrix with the state vector (d)(e)(f) and compare the results with the same matrix obtained from the LIM (a)(b)(c). The calculation is done at different lags up to 132 months.

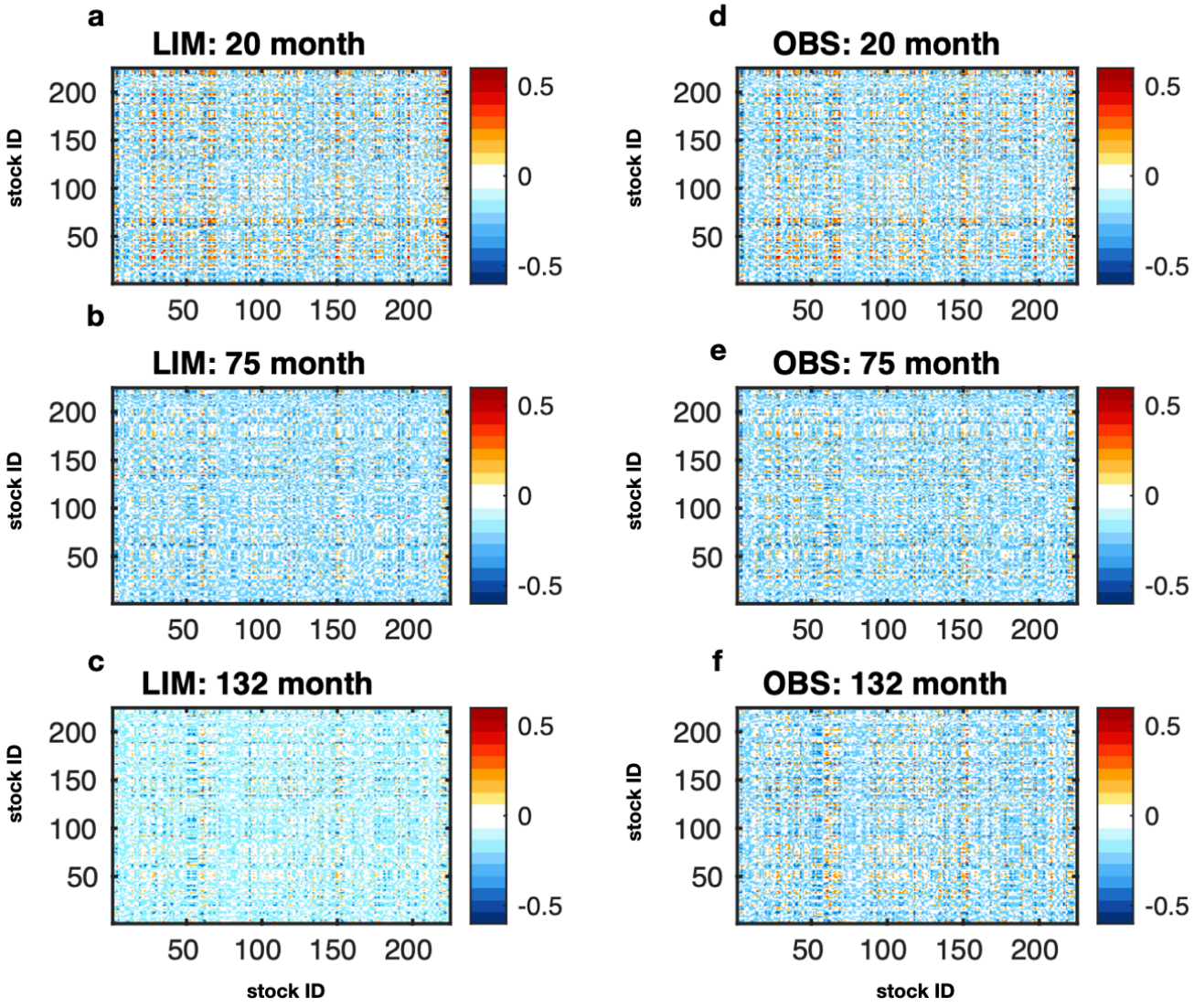

Figure B.6: LIM tau test for the LME stocks. The test consists in calculating the covariance matrix with the state vector (d)(e)(f) and compare the results with the same matrix obtained from the LIM (a)(b)(c). The calculation is done at different lags up to 132 months.

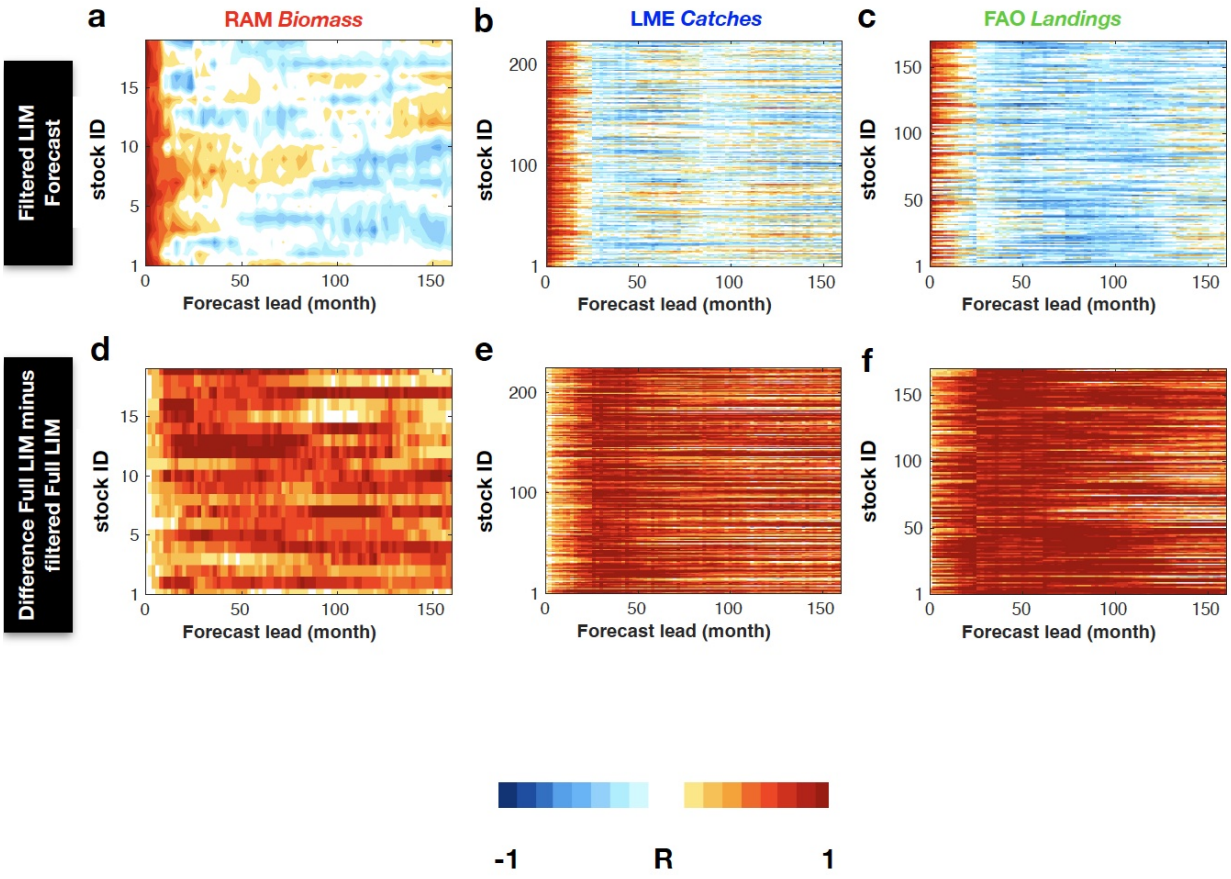

Figure B.7: The LIM forecasting correlation skill as a function of different lead-times is displayed from the RAM (a), LME (b), and FAO (c) stocks. Prior to the computation of the skill, a 6-year high-pass filter applied. The difference in skill between the full LIM and the high-pass version is displayed in (d), (e), and (f) for the three datasets respectively

BIBLIOGRAPHY

[1] Navarra, G.G., Di Lorenzo, E. Poleward shift and intensified variability of Kuroshio-Oyashio extension and North Pacific Transition Zone under climate change. Clim Dyn 56, 2469–2486 (2021). https://doi.org/10.1007/s00382-021-05677-0

[2] Navarra GG, Di Lorenzo E,Rykaczewski RR and Capotondi A (2022) Predictability and empirical dynamics of fisheries time series in the North Pacific. Front. Mar. Sci. 9:969319. doi: 10.3389/fmars.2022.969319